Search for TeV neutrinos from point-like sources in the southern sky using four years of IceCube data

Dissertation

zur Erlangung des akademischen Grades

doctor rerum naturalium

(Dr. rer. nat.)

im Fach Physik

eingereicht an der

Mathematisch-Naturwissenschafltichen Fakultät

der Humboldt-Universität zu Berlin

von

M.Sc. Simon David Altmann

Präsidentin der Humboldt-Universität zu Berlin:

Prof. Dr.-Ing. habil. Dr. Sabine Kunst

Dekan der Mathematisch-Naturwissenschaftlichen Fakultät:

Prof. Dr. Elmar Kulke

Gutachter: 1. Prof. Dr. Alexander Kappes
2. Prof. Dr. Allan Hallgren
3. Prof. Dr. Thomas Lohse

Tag der mündlichen Prüfung: 02.02.2017

Zusammenfassung

Galaktische und extra-galaktische Objekte sind in der Lage geladene Teilchen (die kosmische Strahlung) zu sehr hohen Energien zu beschleunigen. Allerdings sind noch viele Fragen bezüglich dieser Objekte und der Beschleunigungsmechanismen offen. Sowohl Gammastrahlung als auch Neutrinos werden von den Beschleunigungsorten kosmischer Strahlung erwartet. Ihr Nachweis ermöglicht die Studie dieser kosmischen Teilchenbeschleuniger. Gammastrahlung wurde von galaktischen und extra-galaktischen Objekten beobachtet. Für viele dieser Objekte ist es jedoch nicht eindeutig ob diese Gammastrahlung ein Resultat der Beschleunigung kosmischer Strahlen ist oder durch andere Prozesse erzeugt wurde. Für Neutrinos besteht diese Zweideutigkeit nicht, sie sind eindeutige Spuren der Beschleunigung kosmischer Strahlen. Dies macht sie zu idealen Boten. Der astrophysikalische Neutrinofluss wurde vom IceCube Neutrino Observatorium am Südpol gemessen. Einzelne Quellen dieses Flusses konnten noch nicht aufgelöst werden. Der Südhimmel beheimatet viele galaktische Objekte, unter Anderen das Zentrum der Galaxie, von denen Gammastrahlung im GeV und TeV Bereich beobachtet wird. Die Detektion von Neutrinos wäre ein Beweis für die Beschleunigung kosmischer Strahlung von diesen Objekten und würde Rückschlüsse auf ihre Umgebung und ihre Beschleunigungsmechanismen erlauben. Der Nachweis dieser Neutrinos mit IceCube wird durch den sehr großen Untergrund von atmosphärischen Myonen erschwert. Für dieser Arbeit wurde eine Datenselektion entwickelt die den Untergrund durch Verwendung des äußeren Detektorteils und der Eventtopologie reduziert. Die Analyse ist auf die Selektion von Myonspuren aus Wechselwirkungen von Myonneutrinos innerhalb des Detektorvolumens spezialisiert. Energieverluste und Richtung der resultierenden Myonspur werden rekonstruiert. Diese Informationen werden verwendet um nach potentiellen Quellen astrophysikalischer Neutrino im Rahmen einer ungebinnten Likelihoodanalyse zu suchen. Daten die zwischen 2011 und 2015 mit IceCube genommen wurden werden für diese Analyse verwendet. Im Gegensatz zu früheren Arbeiten liegt der Fokus auf Neutrinos mit Energien zwischen ein paar TeV und 100 TeV. In diesem Energiebereich wird die Sensitivität für die Detektion einer Neutrinopunktquelle um einen Faktor zwei (oder besser) verbessert. Die Resultate für eine Liste von 96 Quellkandidaten und für eine offene Suche am gesamten Südhimmel werden präsentiert. Es wurde keine signifikante Abweichung von der Untergrundhypothese gefunden. Daraus resultieren Limitationen für Neutrinoemissionen.

Abstract

There are accelerators in the universe that can accelerate charged particles (cosmic rays) to very high energies. Many questions regarding these accelerators are still open. Gamma rays and neutrinos are particles expected from sites of cosmic ray acceleration and can be used to study the environment and acceleration mechanisms of these sites. While sources for both galactic and extra-galactic gamma rays have been observed, it is often unclear whether these gamma rays are by-products of cosmic ray acceleration. This ambiguity does not exist for neutrinos making them ideal tracers for cosmic ray acceleration. An astrophysical neutrino flux has been measured by the IceCube detector, located at the South Pole. However, single sources have not been resolved yet. The part of the sky visible from the southern hemisphere hosts the Galactic Centre and many other galactic sources observed in GeV and TeV gamma-rays. Detection of neutrinos from these sources would identify them as acceleration sites and lead to a better understanding of the environment of the acceleration sites and the acceleration mechanisms. However, this is difficult due to the vast background of atmospheric muons also detected in the IceCube detector. For this thesis a data selection was developed that reduces this background by using the outer part of the detector as veto region and the topology of the event. This selection focusses on the selection of muon-tracks from muon-neutrino interactions inside the detector volume. The direction and the energy-profile of these tracks can be reconstructed. This information is used to search for potential sources of neutrinos using an unbinned likelihood method. This analysis uses data taken between 2011 and 2015. In contrast to earlier IceCube analyses this analysis is optimized for energies between a few TeV and $100\,TeV$ and improves the sensitivity of the detector for a point-like source by factor of two (or better) in this energy range compared to other IceCube analyses with similar livetime. Results for a list of 96 sources observed in TeV gamma-rays and a sky-scan are presented. No significant overfluctuation has been observed and limits on the neutrino emission of the sources are given.

Contents

List of Tables

List of Figures

1. Introduction

Measurements of the ionization of Earth's atmosphere taken by Viktor Franz Hess in 1912 lead to the awareness that Earth is bombarded by charged particles from space (cosmic rays). This motivated many follow-up experiments, which tried to answer the most fundamental questions one can imagine if a new thing is discovered. Where do these particles come from, which energy do they carry with them, where do they get the energy from, what is the abundance of chemical elements among the cosmic rays are just some of them? While some of these questions like the energy and chemical composition of the particles are now somewhat answered, other questions like the origin of cosmic rays and their acceleration mechanisms remain unanswered problems in the field of astroparticle physics.

Neutrinos can be used to answer these questions. Their ability to travel large distances without suffering absorption and deflection makes them ideal. However, the same properties make them challenging to detect. Large volumes of instrumented material are required to detect a sufficient number of high-energy astrophysical neutrinos. Neutrinos can be reconstructed by the detection of light emitted by the propagation of secondary particles through this material produced when they interact with matter. The largest of these detectors is the IceCube detector built at the South Pole. It uses the glacial ice between $1450\,\mathrm{m}$ to $2450\,\mathrm{m}$ as medium with an instrumented volume of $1\,\mathrm{km}^3$. IceCube has detected astrophysical neutrinos, but their sources are still unknown.

The aim of this thesis, written roughly $30\,\mathrm{km}$ away from the town of Bad Saarow where Hess landed after his measurements in 1912, is to find or constrain the potential sites of production for astrophysical neutrinos measured by IceCube using four years of data of IceCube taken between May 2011 and May 2015. The focus lies on the Southern sky, which hosts a large number of galactic source candidates for cosmic ray and neutrino production. Here the main challenge is the suppression of the background of atmospheric muons, amounting to almost 100 billion detected events each year – compared to only a handful of events expected from a galactic source. This analysis achieves this by focussing on "starting track" – muon neutrinos interacting within the detector volume, producing a muon track that can be used to estimate the neutrino direction with good resolution.

Following this introduction chapter 2 provides a summary over the detected cosmic rays, gamma rays and neutrinos, discusses how these observations can be connected and introduces predictions for neutrino emission from potential sources. Chapter 3 describes how neutrinos interact and how they can be detected. Several detectors, among them the IceCube detector, used for this analysis, are compared. The principal

search strategy of this search and the results of previous searches for neutrino emission are discussed in section 4. Chapter 5 focusses on the event selection and sums up the properties of the selected events used for this analysis. In chapter 6 the unbinned likelihood method used in this search and the results of this analysis are explained and discussed. The last chapter, chapter 7, summarizes this work and presents a brief overview over future developments.

2. The high energy universe

2.1. The discovery of cosmic rays

In 1912 VICTOR FRANZ HESS investigated the number of charged particles in the Earth's atmosphere via ionization measurements. Earlier measurements indicated that their rate would decrease, if the measurement was taken on a high building or in a balloon. This was understood to be due to the larger distance to the ground, where charged particles are expected due to the natural radioactivity of the Earth.

Going to altitudes of over 5000 m HESS found that the rate was not continuously decreasing – as one would expect by Earth-bound radioactivity alone, but increasing in altitudes above 1500 m [1]. He interpreted this as the existence of another source of charged particles arriving from outside the Earth's atmosphere which became known as **cosmic rays**.

His measurements were subsequently verified and he was awarded the Nobel Prize in Physics 1937 for his discovery. Over the coming decades the study of cosmic rays led to the discovery of several new particles, like positrons in 1930, muons in 1936, and both pions and kaons in 1947 [1]. By measuring their composition, energies and abundance the understanding of our universe was greatly improved. However, the sources of cosmic rays have not been identified yet.

2.2. Messengers

In addition to the charged particles mentioned above, neutral particles, photons and neutrinos, from outside the Earth's atmosphere have been observed. It is suspected that the same sites that accelerate charged particles are also responsible for the production of high energetic neutral particles. Accordingly, this section discusses first properties of the measured ion spectrum and how to detect cosmic rays. A discussion on how gamma rays can be produced and detected follows in section 2.2.3. Electrons, positrons, neutrons and neutrinos are briefly discussed.

2.2.1. Charged particles

Ions

Magnetic fields both in galaxies and in inter-galactic space deflect charged particles. Thus, the reconstructed direction of the particle does likely not point to the source of the particle and their arrival direction cannot be used to establish their origin. However, energy distribution and composition[1] can be estimated. In general the energy distribution follows a power-law [1], see eq. 2.1:

$$N(E)dE = KE^{-\gamma}dE. \tag{2.1}$$

The exponent γ is also known as the "spectral index". As can be seen in Fig. 2.1 the measured spectral index of the energy spectrum varies with energy. A spectral
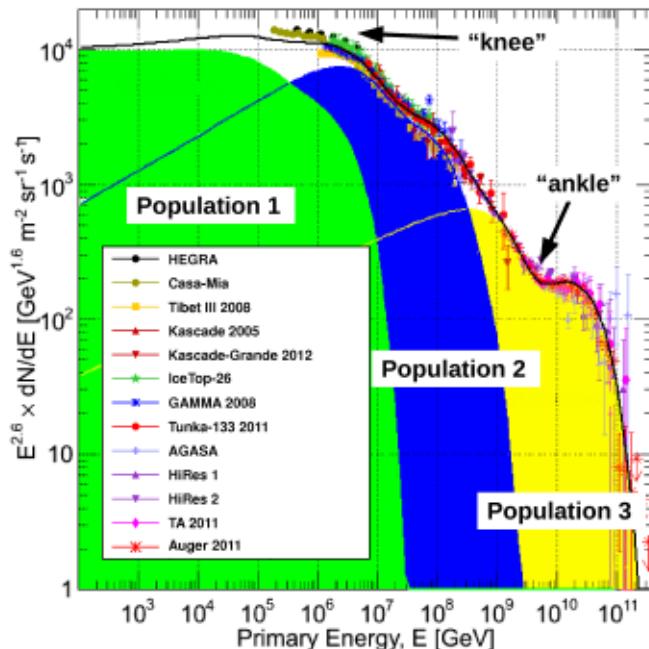
Figure 2.1: The energy spectrum of cosmic rays as measured by several experiments and three populations models of cosmic rays fitted to the data. Two changes in the spectral index at the "knee" and the "ankle" are indicated by arrows. This plot is a modified version from Fig. 4b in [2].

change at about $10^{15.5}$ eV, the so-called "knee", can be interpreted as the transition between two galactic components (population 1 and population 2 in Fig. 2.1) of the

---

[1]The abundance of ions of chemical elements (like H, HE or FE)

spectrum [2]. The region between "knee" and "ankle" (population 2) can be explained by the heavier elements accelerated in the galaxy [2, 3]. The region at the "ankle" and above (population 3) is thought to be of extra-galactic origin [4]. This is because at these energies the magnetic fields of the galaxy would be too small to contain the particles.

The features of the cosmic ray spectrum could also be explained with a purely galactic origin of cosmic rays [5].

It was pointed out by HILLAS that the energy of the observed cosmic ray can limit the possible acceleration sites [6]. The assumption is that the particle has to remain in the site during acceleration. Thus, the size of the site and the magnetic fields in it have to be sufficiently large to satisfy this assumption. A relativistic particle in a static magnetic field normal to the particals velocity will follow a cycle with radius $r = 1.08 \frac{E[1 \times 10^{15} \, eV]}{ZB[\mu G]}[pc]$ [6]. Here, E is the energy of the particle, B is the magnetic field and Z the atomic number of the element. The diameter of the circle defined by r is the minimal size $(d_{site} = 2r)$ for an acceleration site and gives a direct connection between maximal possible energy and the magnetic fields and size of an acceleration site $E_{max} \sim d_{site} ZB$ – heavier elements can reach higher energies in an acceleration site.

This argument by HILLAS can be used to plot source classes based on their magnetic fields and sizes (see Fig. 2.2). Following this argument some source classes, like supernova remnants are already excluded as production sites for ultra high-energetic cosmic rays (UHECRs; $E > 10 \times 10^{18} \, eV$).

Electrons and positrons

Due to their small mass electrons (and positrons) loose energy quickly compared to ions in the presence of magnetic fields, radiation or matter [8]. Measurements of the electron and positron spectrum have been performed by several experiments [9–11]. An observed rise in the positron-electron ratio at a few $100 \, GeV$ is often seen as an indicator for a local accelerator of electrons and positrons, like a near by[2] pulsar wind nebula [12], or a hint for dark matter [13, 14].

Atmospheric interactions

If charged particles arrive at Earth they can penetrate the Earth's atmosphere. Eventually, the primary particles interact with a particle of the atmosphere and produce several secondary particles, which is similar to particle interactions in man-made accelerators [1]. These secondary particles can interact again and a "shower" of particles is produced. Secondary produced electrons and photons propagate in a so-called "electro-magnetic cascade" in which electron-positron pairs are produced and the charged leptons lose energy via Bremsstrahlung until the created photons do not have enough energy to

---

[2]In the work of [12] the Vela pulsar with a distance of about $300 \, pc$ from Earth.
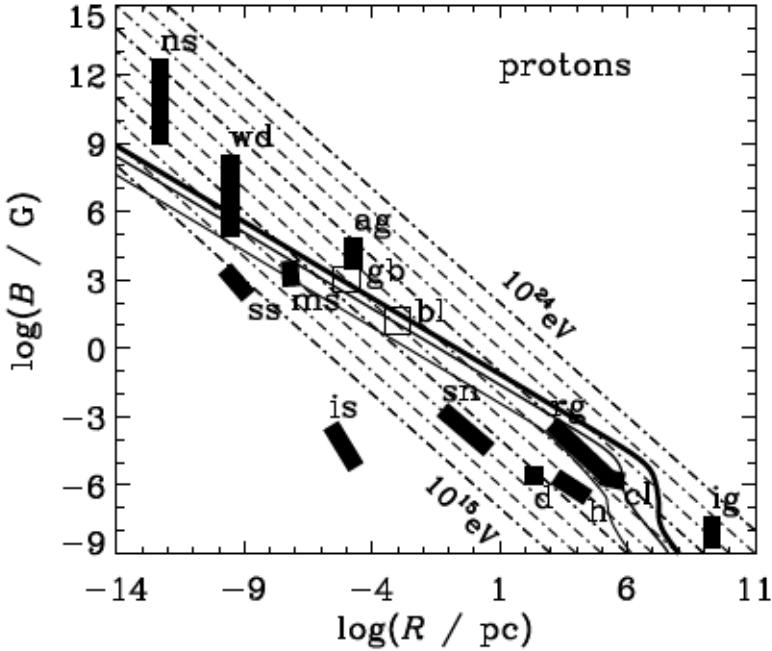
Figure 2.2: Possible acceleration sites placed according to their magnetic fields and size shown for neutron stars (ns), white dwarfs (wd), sunspots (ss), magnetic stars (ms), active galactic nuclei (ag), interstellar space (is), SNRs (sn), radio galaxy lobes (rg), galactic disk (d) and halo (h), clusters of galaxies(cl), blazars (bl) and gamma ray burst (gb) and intergalactic medium (ig). Diagonal dashed lines indicate the maximum energy to which protons can be accelerated by the given combination of magnetic fields and size. Solid lines show the maximum energy to which a proton can be accelerated by shock acceleration of different efficiency (see [7] and section 2.3 for more detail. Taken from [7].

create new electron-positron pairs. Such an electro-magnetic cascade is also produced if a cosmic gamma ray or electron/positron penetrates the atmosphere.

The produced hadrons interact again with particles in the atmosphere or decay. The most abundant hadronic decays are the decays of Pions and Kaons, in which neutrinos and charged leptons, such as muons, can be created. Muons have a livetime of about 2.2×10^{-6} s [15]. Since they often are highly relativistic they can reach the surface and even penetrate the Earth several km deep. The spectrum of atmospheric muons [16], and both atmospheric muon neutrinos [17] and electron neutrinos [18] has been measured, see Fig. 2.3.
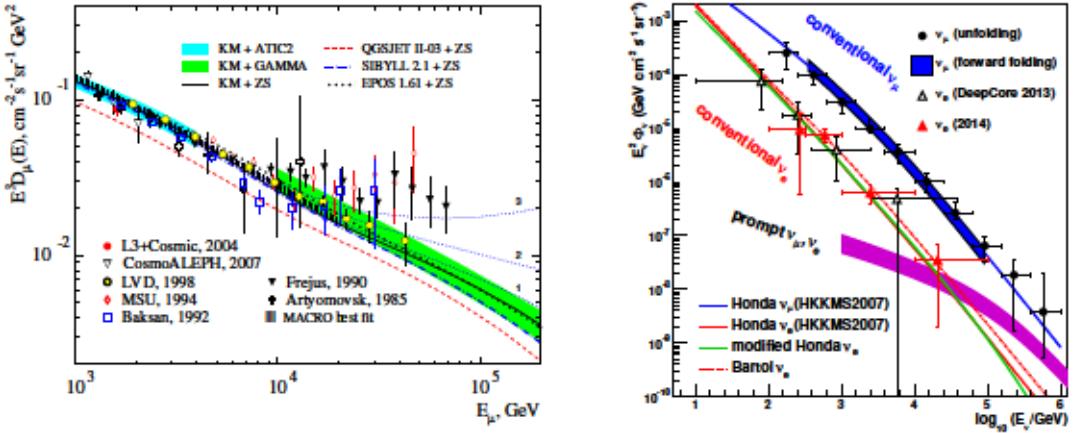
Figure 2.3: Measurements of the atospheric muon (left) and neutrino (right) spectrum. Taken from: left [19] right [18]

Due to energy-dependent energy losses in the atmosphere the observed spectrum for neutrinos and muons is steeper than the primary cosmic ray spectrum[3]. At higher primary particle energies not only Pions and Kaons but also heavier Mesons (like the D-Meson) can be produced in significant numbers [20]. These Mesons decay so rapidly ("prompt") that their energy loss during propagation through the atmosphere is small. Thus, their spectrum is expected to follow the spectrum of the primary cosmic rays.

However, this "prompt" flux has not been measured conclusively [16, 18]. An overall decrease in statistic due to the steep spectral index at higher energies and the even steeper spectral index for energies higher than the "knee" of the cosmic rays – and in the case of neutrinos the existence of the astrophysical neutrino flux – make this a challenging task.

Detection

There are two different approaches to detect cosmic rays. At low energies fluxes are still high enough to be detected directly with the limited detector area of about $1\,m^2$ of balloons high in the atmosphere or satellites. Modern detectors can determine both the element type of ions detected and their energy. Direct detection can be used up to ~ $100\,TeV$ [21].

At higher energies direct detection becomes more challenging. With the decrease in flux the number of expected events changes from about 10 events per second with a $100\,cm^2$ detector in the range of $1\,GeV$ [21] to one particle a year per km^2 at the

---

[3]A spectral index of 3.7 compared to 2.7 for primary cosmic rays with energies below the "knee".

energy of the "ankle" [22]. Cosmic rays at these energies and above are then usually detected by measuring properties of the particle shower they produce (see section 2.2.1). The electro-magnetic component, the number of produced muons or the observation of the fluorescence light produced in the atmosphere by the shower [21] are all be used to reconstruct the energy of the particle that produced the shower. However, the indirect detection makes it difficult to determine the chemical element of the cosmic ray. Currently this is only possible on a statistical basis [21].

2.2.2. Neutrons

Astrophysical neutrons could be produced by the interactions of both protons with protons and protons with photons [23]. Heavier nuclei can also create neutrons via spallation or photodisintegration. In first order the energy of the produced neutron depends on the energy per nucleon. Hence, an iron nucleus has to have 56 times the energy of a proton nucleus to create a neutron of same energy.

Since neutrons are charge-less they are not deflected by magnetic fields. Therefore, the directional reconstruction of a neutron would point to its source. However, its mean lifetime of $886\,\mathrm{s}$ puts constrains on the distance from which neutrons are expected to reach Earth before they decay. Taking relativistic effects into account its mean travel distance is about $9.2\,\mathrm{pc}$ at $1\,\mathrm{PeV}$. In air shower experiments a potential neutron signal would manifest itself in an access of proton like events in direction of its source. However, a dedicated searches by both the Pierre Auger Observatory [24] and the IceCube Observatory [25] have not yet discovered any neutron source.

2.2.3. Very high-energetic (VHE) Gamma rays

Gamma rays are not deflected by magnetic fields. Thus, their reconstructed direction is more likely to point to their source.

Production

Despite the fact that over 150 sources of Very High Energy (VHE) gamma rays ($E_\gamma >$ $100\,\mathrm{GeV}$) have been identified [26], it is often unclear how they produce these gamma rays. In the following paragraphs two suspected production mechanisms are discussed.

Leptonic production   The first mechanism how gamma rays can be produced is "leptonic production". Electrons are accelerated in a source region. The interactions between these electrons and photons or magnetic fields can produce gamma rays in various ways. When they scatter with photons in the ambient environment they can transfer part of their energy to the photon. This process is also called inverse Compton (IC) scattering (see [1]). A special case of IC scattering is self-synchrotron Compton radiation. Here the electron

interacts with a photon that was produced via synchrotron. Gamma rays can also be emitted by electrons suffering Bremsstrahlung losses or emitting synchrotron radiation.

Hadronic production The second option of VHE gamma ray production is the interaction of high-energy charged hadronic particles, like protons, with other matter (pp) or radiation (pγ). Neutral mesons like π^0, K^0, D^0, ... can be produced as secondary particles. When these mesons decay they can produce VHE gamma rays. If instead charged mesons are produced, their direct decay products can be neutrinos, due to charge and lepton-number conservation. At some point in the decay chain of a charged meson a neutrino has to be produced. The following examples, taken from [27], show the production of light mesons in pγ and pp interactions as well as the exemplary production of neutrinos in the decay of a charged mesons and photons in the decay of neutral mesons :

$$
\left.\begin{array}{c} p + p \\ p + \gamma \end{array}\right\} \rightarrow \pi^0 + \pi^{\pm},\, K^{\pm} + ... \tag{2.2}
$$

$$
\begin{aligned}
\pi^0 &\rightarrow & 2\gamma & \tag{2.3} \\
\pi^+ &\rightarrow \mu^+ + \nu_\mu \rightarrow e^+ + \nu_\mu + \bar{\nu}_\mu + \nu_e & \tag{2.4} \\
\pi^- &\rightarrow \mu^- + \bar{\nu}_\mu \rightarrow e^- + \bar{\nu}_\mu + \nu_\mu + \bar{\nu}_e & \tag{2.5}
\end{aligned}
$$

Detection

At the moment three distinct methods for the search of astrophysical gamma rays exist. Since the VHE gamma rays interact with the atmosphere of Earth direct detection is only possible in space. The Fermi-LAT satellite [28] was launched in 2008. It can measure gamma rays in the energy range between $20\,\mathrm{MeV}$ and $2\,\mathrm{TeV}$. The detection principle is pair conversion. The gamma ray produces an electron positron pair. This pair then propagates through the detector allowing for both angular and energy reconstruction. At higher energies the number of expected events is lower. Thus it is too small to detect gamma rays as energies above a few TeV.

At these energies air Cerenkov telescopes are used. They detect the Cerenkov light (details will be discussed in 3.1.2) emitted by the secondary particles which are produced when the photon interacts with the Earth's atmosphere (see section 2.2.1). Three major telescope arrays are operated at the moment. HESS [29] is located in the southern hemisphere and VERITAS [30] and MAGIC [31] are located in the northern hemisphere.

The number of produced Cerenkov photons is small. Therefore, observation is only possible at night and in regions without light pollution. In addition clouds can reduce the available observation time, since the source of the light is at high altitude in the atmosphere. This leads to an active period of data taking of about 10% per annum [32].

One possibility to detect the interactions of gamma rays with the atmosphere independent of daytime and other effects like clouds is the detection of the electro-magnetic shower on the ground. This can be done with larger instrumented volumes of transparent material (usually water). The Cerenkov light emitted in this material is then detected and used to reconstruct energy and direction of the gamma ray that produced the shower. This water Cerenkov technique has been used successful in the Milagro detector [33] and is now used in HAWC detector [34].

While angular reconstruction and higher background compared to air Cerenkov telescopes are disadvantageous, the detector uptime is not limited by weather or light conditions. Thus, it can operate with a non-stop duty cycle. Another advantage is the larger field of view. Air Cerenkov telescopes only observe a small part of the sky (about 5° for the 12 m diameter HESS telescopes [29]). Water Cerenkov telescopes on the other hand are always observing the entire overhead sky (2 sr) [35]. The different energy ranges of the three detection methods and required observation times to detect a specific flux are visualized in Fig. 2.4.
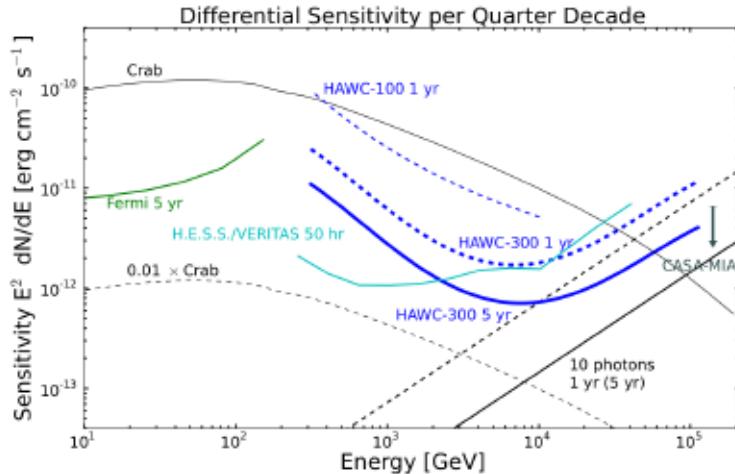
Figure 2.4: Differential gamma ray sensitivity for satellites (Fermi), air cerenkov detectors (Veritas/HESS) and air shower gamma ray detectors (HAWC). Taken from [34].

2.2.4. Neutrinos

As already discussed in section 2.2.3, if VHE gamma rays are produced hadronically neutrinos are expected as well. Hence, predictions can be made on the expected neutrino flux based on the measured VHE gamma ray flux. The detection or non-detection of neutrinos from a source can then be used to verify or disfavour hadronic production in comparison to leptonic production. Additionally, neutrinos can be a messenger from

environments which gamma rays cannot leave. Neutrinos are discussed in more detail in section 2.5 and chapter 3.

2.3. Cosmic accelerators

2.3.1. Acceleration mechanism

As discussed in section 2.2.1, charged particles from space are observed over many decades of energies. Their energy distribution follows a power-law. A potential acceleration mechanism needs to both predict a power-law like shape of the spectrum and accelerate up to the highest energies.

A mechanism, first proposed by ENRICO FERMI ("Fermi acceleration") in 1949 [36], seems to fulfil these requirements. The following explanations and formula notations are inspired by [8]. FERMI showed that particles could gain energy by the collision and reflection with moving molecular clouds within our galaxy. On average, the particle would gain energy proportional to the square of the velocity of the cloud V:

$$\left\langle \frac{\Delta E}{E} \right\rangle = \frac{8}{3} \left(\frac{V}{c} \right)^2 . \tag{2.6}$$

Here and in the following, it is assumed that the accelerated particles are highly relativistic ($v \sim c$). A crucial point is the gain on a stochastic basis. If a cloud moves away from the particle, the particle will lose energy instead of gaining energy in the case of a cloud moving towards the particle. Due to the higher relative velocity in the latter case the particle gains energy on **average** [36]. Additionally, the spectral energy distribution will follow a power-law.

However, it seems like the proposed mechanism is too slow, both due to the low velocity of the cloud and the following collisions. If the particle were to only experience head-on collisions, the energy gain would be proportional to the $\frac{V}{c}$ and not the square. Thus, it would be much more efficient.

One environment in which cosmic rays can be accelerated in this efficient manner are shocks. A shock is the border between two regions of different plasma configuration. In front of the shock wave (upstream region) gas is at rest or slowly moving. Behind the shock (downstream region) wave the gas is moving with a velocity higher then the speed of sound in this medium.

If a relativistic particle crosses the shock from downstream to upstream and vice versa, it will gain energy in the process. The average energy gain for a particle crossing

once from upstream to downstream and back is:

$$\left\langle \frac{\Delta E}{E} \right\rangle = \frac{4}{3}\frac{V}{c}. \tag{2.7}$$

Comparing equations 2.6 and 2.7, acceleration in shocks is more efficient due to the first-order term in $\frac{V}{c}$ compared to the second-order term.

The accelerated particle can always leave the region of acceleration with a certain probability. Repeated acceleration and escape probability lead to a resulting spectral energy distribution that follows a power-law [8]. The spectral index is two – harder than the observed spectral index of the cosmic rays. If one corrects for energy-dependent energy losses between the acceleration site and Earth [37], the expected spectral index will become softer and can explain the observed one[4].

The very efficient acceleration, the correct spectral index and the prediction of acceleration sites and environments make first-order shock acceleration a highly favoured model within the astrophysical community. However, the entire mechanism presented assumes relativistic particles in the first place. Thus, it cannot explain how these particles were accelerated up to this point. The spectral index of two is also not fixed [38] – by varying parameters of the acceleration site, like assuming relativistic shocks, the index can vary [39].

In general, particles can also be accelerated in electric fields. However, the abundance of unbound electrons and ions in space makes it very challenging to built up electric fields that are capable of accelerating particles up to the highest energies. One environment in which this could be possible are areas with strong magnetic fields. If zones of different magnetic polarity are close to each other, magnetic reconnection can occur. While the entire process would require an explanation of magneto hydrodynamics in more detail than feasible in the scope of this chapter, a comprehensive review of the topic can be found in [40]. Briefly summarized the phenomenon can be described as a conversion from magnetic field energy into the kinetic energy of a particle via electric fields in the reconnection layer. It can be shown [41] that this process is capable of accelerating particles to the highest energies.

2.3.2. Galactic source candidates for cosmic rays

The galactic center and the majority of observed galactic gamma ray sources is located in the southern sky. As already mentioned in section 2.2.1, cosmic rays up to at least $10^{15.5}$ eV are suspected to be accelerated in our galaxy.

---

[4]Observed spectral index below the knee: 2.7, spectral index by first-order fermi acceleration and energy-dependent energy losses during propagation: 2.6.

Supernova mechanisms Several galactic object classes which are suspected to be sites of cosmic rays acceleration are descendants of a star exploding in a supernova. After a star has depleted its fusion fuel resources, it cannot keep up the pressure against the gravitational forces in its inner part (core) and as a result its outer parts collapses [8]. Depending on the mass of the star ($\gtrsim 8\,M_\odot$), the gravitational forces in the core of the star can become strong enough for the electrons of the atoms to overcome the electron degeneracy pressure. They are then pushed in the nucleus and create, with the protons in the nucleus, neutrons and neutrinos with energies in the MeV range [42]. The neutrons form a neutron star. This neutron star is so dense that additional fermions would have to overcome the neutron degeneracy pressure. If the star is massive enough, a black hole will be created. Otherwise, the outer parts of the star which are falling inwards, bounce of the neutron star and propagate away from it and form a supernova remnant.

The remnant parts' kinetic energy of about 10^{51} ergs is small compared to the energy that is carried away by MeV neutrinos (about 10^{53} ergs) [27]. For a black hole to emerge the mass of the progenitor star has to be larger than $\sim 25\,M_\odot$ [42]. Since the core of the star collapsed either to a neutron star or to a black hole, this process is called a core collapse supernovae. In 1987, neutrinos from a supernova in the Large Magellanic Cloud[5] were detected [43]. Up to today these neutrinos are the only neutrinos that were associated with a specific source outside our solar system.

Also lighter stars' life can end with a supernova explosion. If a star is, at the end of his lifecycle, too light to overcome the electron degeneracy pressure, a white dwarf will be formed. In a system with more than one star this white dwarf then can accrete mass from a nearby companion. The accreted mass increases the pressure inside the white dwarf and reignites the fusion of remaining carbon [44]. This increases the temperature inside the white dwarf and starts additional fusion processes. The released energy in these reignited fusion processes is large enough to overcome the gravitational binding energy of the star (0.5×10^{51} ergs) and to accelerate mass ejecta up to about $1 \times 10^4\,\mathrm{km s^{-1}}$, which corresponds to about 1×10^{51} ergs [44].

Supernovae of this type (also known as Type Ia) are thought to emit very similar luminosity profiles. This can be used to calculate the distance of the supernova by comparing the luminosity observed on Earth to the emitted luminosity [45].

Supernova remnants (SNR) After a supernova explosion the ejecta is moving radially away from it at high velocities. It propagates through the vicinity around the exploded star, which contains interstellar matter (ISM) and can contain molecular clouds. This system now can fulfil the requirements for shock acceleration as discussed in section 2.3.1. Intriguingly, the kinetic energy released in a supernova (1×10^{51} ergs) can provide enough

---

[5]A nearby satellite galaxy of our own galaxy.

energy for cosmic rays up to the "knee" if 3% to 30% of the released energy are used to accelerate cosmic rays [46].

Pulsar Wind Nebulae (PWN)   When a supernova explosion results in the creation of a neutron star, most of the angular momentum of the progenitor star remains with the neutron star. Due to its much smaller size ($10\,\mathrm{km}$ to $15\,\mathrm{km}$ [47] radius compared to $7 \times 10^5\,\mathrm{km}$ [48] of our sun as an example.) it starts to rotate very fast. If a pulsed radio emission from this neutron star is detected it is called a "pulsar". At the same time, large rotating magnetic fields (up to $1 \times 10^{12}\,\mathrm{G}$) create strong potential differences in the electric field between the pole and the equator of the neutron star. This electric field is so strong that it strips away electrons and ions [49] from the surface of the neutron star.

Charged particles that are stripped away fill the vicinity around the pulsar and are called the pulsar wind [50]. They emit synchrotron radiation in the radio and X-ray band when they are deflected by the magnetic field of the pulsar [47]. The intereseted reader can find additional information in these reviews [51–53] and a detailed description of the magnetic fields and the conversion from electro-magnetic into kinetic energy in [54]. Due to their strong magnetic fields PWN are candidates for particle acceleration through magnetic reconnection.

Binary system / Microquasar   A binary system that consists of a compact object (like a neutron star or a blackhole) and a companion star or another compact object can accelerate particles to high energies. The compact object can accrete mass from the companion star. It is believed that it converts parts of the energy gained by this accretion into the acceleration of particles in jets along its rotational axes [55] or through interactions of winds [56].

The Galactic Centre   The centre of this galaxy hosts a super-massive black hole, Sagittarius A*. This black hole is proposed as source of the galactic cosmic rays in [57]. Today, the observed luminosity is too small to be a candidate for sufficient particle acceleration. However, large structures, so-called bubbles, observed above and below the galactic centre [58] are an indication for a more active phase of the black hole in the past. The black hole could have accelerated particles in jets by using energy released by mass accretion on it.

The size and position of the bubbles can be used to estimate the time window of this high activity phase of the black hole. This yields an activity phase of about $1 \times 10^7\,\mathrm{yrs}$ which started about $2.4 \times 10^7\,\mathrm{yrs}$ ago. This is similar to the average escape time of a cosmic ray from out galaxy, $1.5 \times 10^7\,\mathrm{yrs}$ [59]. As pointed out in [60], the average escape time can also be larger by factor two to four if different assumptions about the cosmic ray propagation are made.

Similar to shock acceleration a spectral index of two at the source is predicted. Hence, a phase of high activity in the phase of Sagittarius A* is one possible origin of galactic cosmic rays.

2.3.3. Extra-galactic source candidates for cosmic rays

Active galactic nuclei Active galactic nuclei (AGNs) are inner parts of galaxies with a very high luminosity [61]. It is assumed that their emission is fuelled by the accretion of mass on a supermassive black hole. AGNs are prime candidates for the acceleration of UHE cosmic rays as can also be seen in Fig. 2.2. Due to mass accreted by the black hole an accretion disk is formed. Sometimes one also observes two highly relativistic jets orthogonal to the disk. Some models expect the UHE cosmic rays to be accelerated in the jets [3]. Depending on the viewing angle an AGN is identified in different source classes. An example are AGNs with one of their jets pointing directly to us, which are called blazars.

Gamma ray bursts Gamma ray bursts (GRBs) are short (seconds or less) bursts of photons peaking at $10\,keV$ to $1 \times 10^4\,keV$ [62]. In this short period their luminosity is comparable to the entire universe integrated over all wavelengths. GRBs are usually separated in two classes based on the distribution of GRB durations.

Short GRBs peak at a duration of about $0.3\,s$ while long GRBs peak at about $30\,s$. GRBs with a duration smaller than $2\,s$ are classified as short GRBs, otherwise, they are classified as long GRBs. The most common interpretation of this feature are two different source classes. The collapse of massive stars (mass $> 15\,M_\odot$) has been identified as the progenitor for some of the long GRBs. Likewise, for short GRBs the merging of two compact objects in a binary system has been discussed [63]. However, there are still many open questions when it comes to the progenitors of GRBs. The observation of VHE gamma rays from these objects might be an indicator for hadronic processes. Thus, GRBs are a possible site of cosmic ray acceleration.

2.4. Observed gamma sources

As discussed in section 2.2.3 VHE gamma rays can be produced by the interaction of cosmic rays with ambient matter or photon fields. Unlike the charged cosmic rays the neutral gamma rays are not deflected. Hence, the observation of VHE gamma ray emission from an astrophysical object or region can be seen as an indicator that it is also a site of cosmic ray acceleration. However, a VHE gamma ray can also be produced by leptonic processes (also discussed in section 2.2.3). In the following both observations of VHE gamma rays from the galactic and extra-galactic origin are discussed.

Galactic VHE gamma rays   Both HESS [64] and the Fermi-LAT satellite have surveyed the galactic plane[6] and found numerous galactic sources (see Fig. 2.5). Depending on their position on the sky, many of these also have been observed by MAGIC and VERITAS. The diffuse emission from the galactic plane is also measured by FERMI [66] and HESS [67]. While some sources seem to produce the observed gamma rays leptonically, for others there is evidence of hadronic production. For supernova remnants,

Figure 2.5: Results from the galactic plane scan with HESS and the Fermi-LAT satelite. Taken from [68].

one possible explanation is a correlation between the age of the remnant and the density in which interactions take place [69]. It is believed that leptonic production of gamma rays occurs in low density environments and hadronic production in environments with a higher density.

In many cases a source is not only observed in GeV and TeV gamma rays, but also in radio and X-ray bands. The emission in these bands is generally interpreted as synchrotron radiation of electrons. Thus, a model describing the GeV and TeV emission by electrons losing their energy via inverse-compton scattering or Bremsstrahlung has to be consistent with the radio and X-ray observations [70]. In Fig. 2.6 the supernova remnant W51C is used as an example for the differentiation between models. While the observed GeV and TeV emission fits both hadronic (model a) and leptonic (model b + c) models well, the predicted radio emission for the leptonic models is in disagreement with the data. The gamma ray emission is therefore likely hadronic in origin.

For some supernova remnants the environmental conditions and observed spectra strongly suggest a hadronic origin of the observed GeV and TeV gamma rays (examples:

---

[6]This has also be done by MILAGRO, mainly in the northern sky [65].

Figure 2.6: Spectral energy distribution for W51C. Measured data (radio on the left, VHE gamma rays on the right) and three different models are shown. Figure a) shows a model with a dominant hadronic production of VHE gamma rays and Figure b) and c) show models that predict leptonic processes to dominate the production of VHE gamma rays. Taken from [70]

IC443 and W44 [46]). The crab nebula, a pulsar wind nebula associated with the observation of a supernova in 1054, on the other hand, is well known for being a very bright source in the sky for both radio and X-rays as well as gamma rays up to a few TeV [71]. Due to its brightness in these bands the spectral energy distribution (SED) is well measured and can be very well fitted with a pure leptonic scenario [72–74] as can be seen in Fig. 2.7.

For most of the sources the SEDs are not as well measured as in the previous examples. If an observation in an energy range is missing this can be both due to lack of experimental sensitivity or lack of emission. Additionally, the arguments used in favour and against the hadronic/leptonic case are not always absolute. A good example is the supernova remnant RX J1713.7-3946. The emission in the GeV range shows a very hard spectral index of about $\gamma = 1.5$ [75]. This and the lack of X-ray line emission expected of higher proton number densities in hadronic production [76] were long thought to be arguments for a leptonic production of the observed gamma rays [76, 77].

While simple hadronic models seem to be disfavoured [78], it is possible to explain the observed GeV and TeV emission by hadronic interactions with an additional remnant shell upstream [78] or with a clumpy medium like a dense molecular cloud [79, 80]. The observation or non-observation of neutrinos could help to either support hadronic scenarios or limit their contribution to the observed gamma rays.

The HESS telescopes also detected TeV gamma-rays from the Galactic Centre [81].
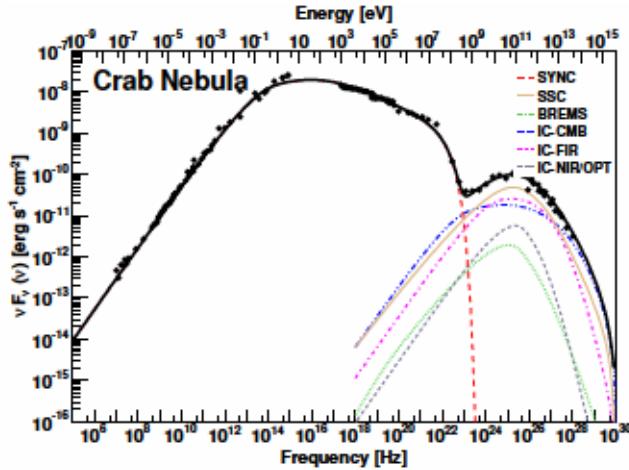
Figure 2.7: Spectral energy distribution for the crab nebula. Data points and predicted emission from various leptonic production mechanisms. Taken from [74].

In its molecular cloud high-energetic electrons will suffer large radiative losses. This disfavours a leptonic origin because it is challenging to explain the large emission region with a leptonic model as it is larger than their expected range. The gamma-ray emission in this region is also a magnitude larger than expectations from the interactions of the "'sea' of cosmic rays" [81] that fills the galaxy. This indicates intrinsic cosmic-ray acceleration in the Galactic Centre and supports the theory of a high activity phase of Sagittarius A* in the past.

Extra-galactic VHE gamma rays VHE gamma rays have also been detected from extra-galactic objects. Observation of TeV gamma rays from AGNs can be seen as an indicator for their ability to accelerate charged ions up to energies above 1×10^{17} eV [82] – if they are of hadronic origin. However, as shown examplary for some blazars in [82], their VHE gamma ray emission can also be explained by both hadronic and leptonic processes (see Fig. 2.8).

Blazars can vary in their emission dependent of time, see Fig. 2.8 and [83]. 3C279, the exemplary blazar shown above, was in a bright state over a few hours observed by the Fermi satellite in December 2013. In this state the detected flux was about ten times higher flux than in its ground state. This emission can be explained by emission of proton synchrotron radiation or by a pure leptonic scenario [83].

As mentioned before, photons can interact with other photons and create electron-positron pairs. PeV photons can interact with the photons of the cosmic microwace background. Due to the abundance of this background light their mean free path is as
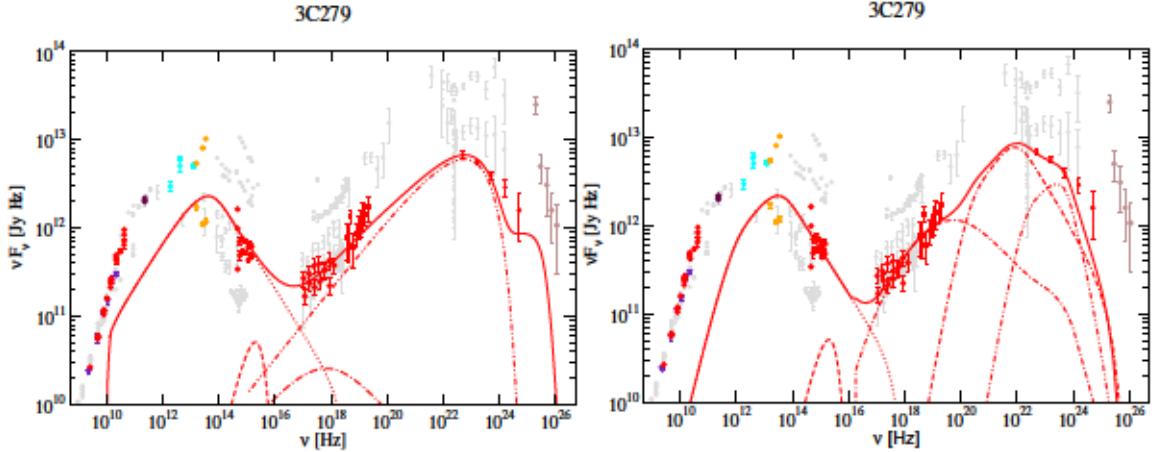
Figure 2.8: Left: Model with hadronic emission (dot-dot-dashed) and various leptonic emissions (other non-solid lines). Right: Leptonic model with various leptonic emissions. In both figures the dotted curve represents the synchrotron emission from electrons. Red points correspond to data taken into account for the fit. The other data points show the variability of the blazar at different points in time. Taken from [82]

small as $1 \times 10^{-2}\,\mathrm{Mpc}^7$ [84].

At TeV energies the VHE gamma rays do not interact with the CMB photons, but with the infrared extra-galactic background light (EBL) [85]. They have a mean free path of $100\,\mathrm{Mpc}$ to $1000\,\mathrm{Mpc}$ (see Fig. 2.9). Hence, their observed spectrum needs to be corrected for this attenuation. This requires both knowledge of the EBL and the source spectrum. Neutrinos can again help to distinguish hadronic and leptonic scenarios and in the case of a hadronic scenario to determine whether a change in the observed spectrum is due to a change in the initial spectrum or absorption. Additionally, in the PeV regime they open the window to a universe (almost) opaque for gamma rays.

2.5. Prospects of neutrino astronomy and its impact

Neutrinos are an unambiguous trace of hadronic processes in a source. Thus, the detection of astrophysical neutrinos is a strong indicator that at least part of the detected gamma ray flux is of hadronic origin. One advantage of neutrinos compared to gamma rays is their limitation to weak interactions (and gravitational forces) while gamma rays can also undergo electro-magnetic interactions. Hence, VHE gamma rays can interact with photons in the production site [86] or the extra-galactic background light [85] on their way to Earth. Therefore, it is not expected to detect these gamma rays from sources

---

[7]About the distance of Earth to the galactic center of $8.4 \pm 0.6\,\mathrm{kpc}$ [15]. 3C279 the examplatory blazar of Fig. 2.8 has a distance from Earth of about $1.8^{+0.5}_{-0.3}\,\mathrm{Mpc}$
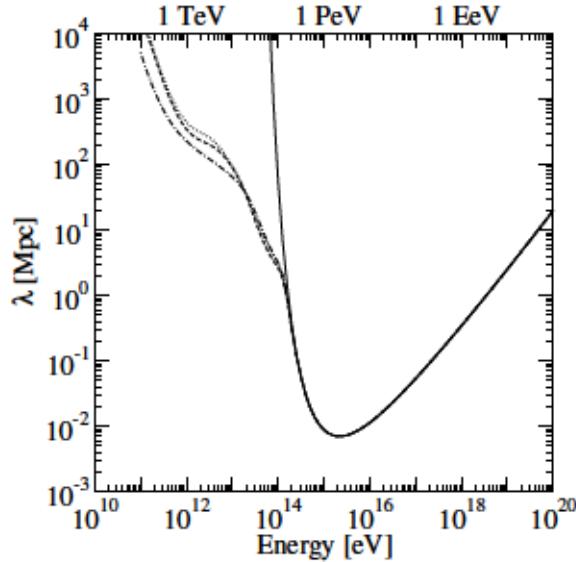
Figure 2.9: The mean free path for VHE gamma rays. Interaction with CMB photons are represented by the solid line. The dashed lines correspond to interactions with different models of the EBL. Taken from [84]

that are far away or produced in a photon-dense environment. About five percent of the energy of a cosmic ray interacting is on average transferred to a single neutrino [87, 88]. Therefore, if a cosmic ray below the "knee" at $1 \times 10^{15.5}$ eV interacts, neutrinos up to a few 100 TeV can be excepted.

IceCube, a neutrino detector that will be discussed in detail in chapter 3, has detected a diffuse astrophysical neutrino flux [89–91] at neutrino energies above 25 TeV [92]. It was pointed out in [86] that this flux already puts constrains on the production sites for the diffuse emission of gamma rays and neutrinos. If the observed diffuse emission of astrophysical neutrinos originated from pp interactions the expected gamma-ray flux in the GeV range would be much higher than observed, as shown in Fig. 2.10.

The same argument is somewhat weaker for pγ interactions [86]. For this scenario it is argued that a source that produces neutrinos efficiently requires target photon fields of such intensity that the source would become opaque for gamma rays in the 1 GeV to 100 GeV due to γγ interactions. Thus, assuming correlation between gamma rays at these energies and the astrophysical neutrinos observed by IceCube might not be fruitful. They conclude that these arguments do not hold for observations of TeV gamma-rays – making them a prime messenger to use combined with neutrino observations. However, in both cases (pp and pγ) assumptions about the neutrino spectrum below 10 TeV are made. In this energy range the shape of the astrophysical neutrino spectrum is still unknown.
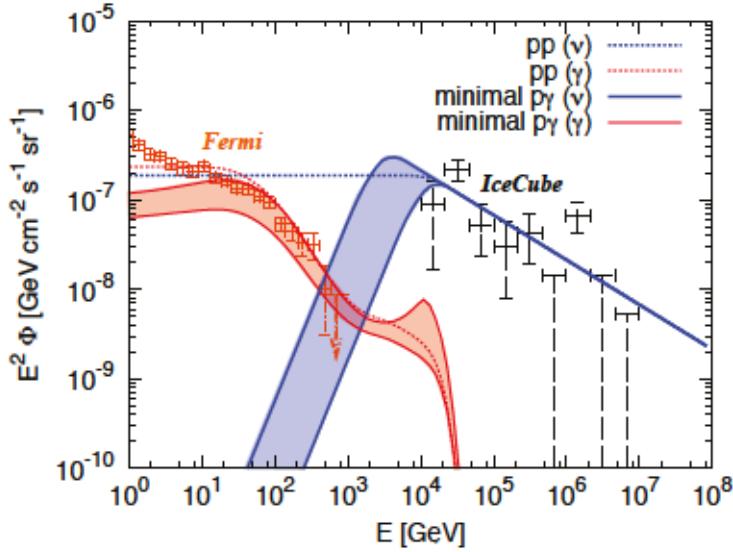
Figure 2.10: The measured diffuse gamma and neutrino emission by Fermi and IceCube. Also shown are generic models for pp and pγ production of the gamma rays and neutrinos, assuming that they are produced in the same sites. Taken from [86]

2.5.1. Expected neutrinos from the galaxy

For all source classes discussed in section 2.3.2 models can be found [55, 93–96] predicting a contribution of neutrinos. In the context of this thesis these sources are point-like sources – sources with a spatial extension below the angular resolution of the experiment. In many cases these models are either constrained by the observed gamma ray spectrum of the source or by the measured flux or upper limits from both the IceCube and the ANTARES[8] collaborations. As discussed in section 2.2.1 and shown in Fig. 2.1 cosmic rays at least up to the "knee" at $1 \times 10^{15.5}$ eV are thought to be of galactic origin. Neutrinos produced in an 1 PeV pp interaction have an average energy below 100 TeV, see Fig. 2.11.

Connecting gamma rays and neutrinos If the hadronic production (pp) of the observed gamma ray flux is believed in, the corresponding expected neutrino flux on Earth can be calculated [97] using the parametrization of pp interactions described in [88]. One obtains:

$$\frac{dN_{\gamma/\nu}}{dE_{\gamma/\nu}} \approx k_{\gamma/\nu} \left(\frac{E_{\gamma/\nu}}{1\,\text{TeV}}\right)^{-\Gamma_{\gamma/\nu}} \exp\left(-\sqrt{\frac{E_{\gamma/\nu}}{\epsilon_{\gamma/\nu}}}\right) \qquad (2.8)$$

In this model the spectra of gamma rays and neutrinos have the same spectral index Γ. The neutrino flux parameter k_ν is related to the gamma ray flux parameter k_γ: $k_\nu \approx (0.71 - 0.16\alpha)k_\gamma$, with α as the cosmic ray spectral index and $\Gamma_{\gamma/\nu} \approx \alpha - 0.1$. If a

---

[8]A neutrino detector discussed in section 3.2.1.
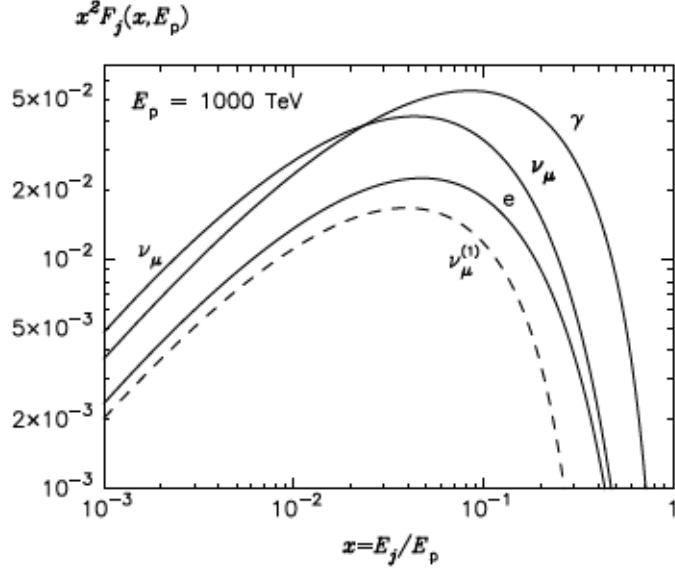
Figure 2.11: SED of secondary particles produced by a pp interaction of a 1 PeV proton and the decay of the resulting mesons. $\nu_\mu^{(1)}$ corresponds to the contribution of muon neutrinos produced by the initial decay of charged pions. The spectrum for electron neutrinos is not shown, but is very similar to the electron spectrum depicted. Taken from [88].

cutoff can be fitted to the gamma ray spectrum, it is parametrized by the $\exp\left(-\sqrt{\frac{E_{\gamma/\nu}}{\epsilon_{\gamma/\nu}}}\right)$ term and $\epsilon_\nu \approx 0.59\epsilon_\gamma$. In the case of no published cutoff a pure power low is fitted ($\epsilon_{\gamma/\nu} = \infty$). For five of the sources discussed in [97] a cutoff is provided with ϵ_γ between 0.21 TeV and 4.24 TeV.

In this model some assumptions have to be made concerning the source and its environment. Examples are the exclusive production of gamma rays via hadronic production (which might not be true for many of the discussed sources) or that both pions and muons do not lose significant parts of their energy before their decay creates neutrinos. The predicted neutrino flux for two strong galactic gamma ray sources SNR RXJ1713.7-3946 and PWN Vela X is shown in Fig. 2.12. However, even with these optimistic assumptions the number of expected neutrinos produced by these processes is small compared to the background of neutrinos produced in interactions of cosmic rays with our atmosphere[9].

Galactic plane The galactic plane has been observed in gamma rays with energies up to a few TeV [67, 98]. At least a part of this observed flux is thought to be of hadronic origin [66], coming from interactions of cosmic rays with interstellar matter. In this case

---

[9]Example: A hypothetical KM3NeT detector would expect to measure about 11 signal neutrinos and 41 background neutrinos above 1 TeV for the SNR RXJ1713.7-3946 over a five year period of data taking.
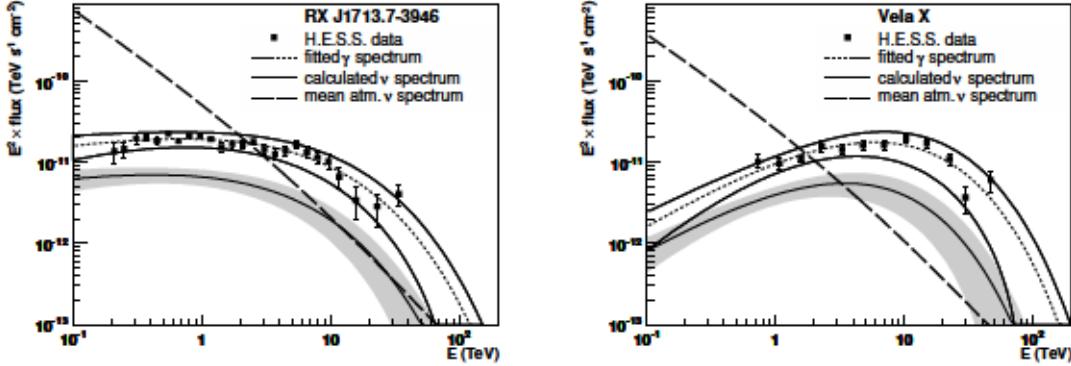
Figure 2.12: Measured and fitted gamma ray spectrum and predicted neutrino spectrum for a given source. The left plot shows this for the SNR RXJ1713.7-3946 and the right plot for the PWN VelaX. Additionally, the predicted atmospheric neutrino flux for a detector in the Mediterranean sea is shown. Taken from [97].

not only gamma rays from the decay of π^0 are expected, but also neutrinos from the decay of charged pions. While some authors claim that the number of expected neutrino events is both small and their energies rather low (90 % of the integral flux from neutrinos with $E_\nu < 10\,\mathrm{TeV}$) [98], others claim that diffuse emission from the galaxy could make up between 10% to 40% of the astrophysical neutrino flux detected by IceCube [99].

Unidentified gamma ray sources It has been discussed in [94] that sources observed only in TeV gamma rays might be old galactic hypernovae. Hypernovae are very bright, "hyper-energetic" supernovae [100]. These sources can produce VHE gamma rays and, if one assumes hadronic processes, also neutrinos. While they could produce neutrinos with energies up to about one PeV the expected number of events would be small.

Dark matter Both from measurement of the cosmic microwave background and the rotation curves of galaxies there is evidence for the existence of an additional mass component in our universe [101] – dark matter. Usually, it is thought to interact only via the weak force and gravity. Its illusive character makes it difficult to be detected. Two possibilities to detect it are the decay of such a dark matter particle inside a detector or the detection of particles produced when two dark matter particles annihilate. In some models both gamma rays and neutrinos from annihilation of dark matter in the galaxy, in particular the Galactic Center, are predicted [102].

2.5.2. Expected neutrinos from extra-galactic source candidates

Like the galactic source candidates above extra-galactic sources are assumed to be point-like in the scope of this thesis.

GRBs   The IceCube neutrino telescope was already able to put strong limits (about one order of magnitude below the detected neutrino flux) on the neutrino flux from GRBs [103], excluding a large contribution to the overall astrophysical neutrino flux [90].

AGNs   For AGNs the vicinity of the black hole [104] and the jet can be production sites of astrophysical neutrinos [105, 106]. Accelerated protons could interact with matter in the host galaxy and produce neutrinos [106]. Recent IceCube results [107, 108] restrict the contribution of AGNs with jets pointing to Earth (so-called blazars) to the measured astrophysical flux to be about 20% or less[10] [108].

Starburst galaxies   Supernova remnants are prime candidates for cosmic ray acceleration sites within our galaxy. Some galaxies, more luminous than ours, have regions with an increased rate of star formation and thus, an increased rate of supernovas. The observation of synchrotron emission by GeV electrons is an indicator for strong (~ 100 times stronger than in our galaxy) magnetic fields. Due to the large magnetic fields and the dense environment neutrinos by pp interactions are expected [87, 109, 110]. Since the cosmic rays are accelerated in the remnant shocks, cosmic ray energies are not expected to be much higher than in our galaxy. Therefore, it seems unlikely that they are the sources of UHE cosmic rays. The expected neutrino energies go up to about $100\,\mathrm{TeV}$ − if one does not assume more extreme scenarios such as galaxy mergers, supermassive black hole activities or hypernovae [110].

Cosmogenic neutrinos   Shortly after the discovery of the Cosmic Microwave Background (CMB), interactions of CMB photons with UHECRs were predicted both by GREISEN [111] and ZATSEPIN and KUZMIN [112]. This later called GZK-effect could produce neutrinos at energies between $10^{16}\,eV$ and $10^{21}\,eV$. However, there are experimental and theoretical uncertainties on the maximum energy and composition of such UHECRs and even in optimistic scenarios the expected number of events is very small for neutrino telescopes like IceCube: About 1.3 events for a pure proton spectrum and > 0.1 events for a pure iron spectrum in one year of data for $E_\nu > 1\,\mathrm{PeV}$ [113].

---

[10]For a sample of 862 Fermi-LAT observed blazars.

3. The principle of high-energy neutrino detection and neutrino telescopes

Most experiments searching for high-energetic ($E_\nu > 10\,\mathrm{GeV}$) neutrinos have done this by looking for the light patterns produced by secondary particles that are created in neutrino interactions with nuclei inside or in the vicinity of the detector. This chapter discusses first the interactions of neutrinos and matter, second the production of light by secondary particles of the neutrino and third the propagation of the light in a transparent medium. Then the detectors are discussed.

3.1. Physics of neutrino detection

3.1.1. The neutrino as an elementary particle

Neutrinos are chargeless leptons. Due to this fact they can only experience the weak-force (and gravitation). There are two possible kinds of interactions between neutrinos and nucleons. They can exchange a $W^\pm$ (charged-current) or exchange a Z^0 (neutral-current) [114]. For neutrinos with energies larger than $15\,\mathrm{GeV}$ deep inelastic scattering (DIS) is the dominant process [114]. DIS is the interaction of the neutrino with a quark in the nucleon. A neutral-current process gives a neutrino in the final state while a charged-current process (shown in Fig. 3.1) gives a charged lepton.
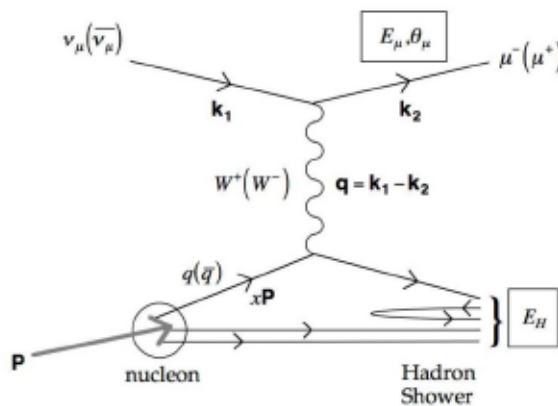
Figure 3.1: Feynman diagram for a charged-current DIS process. Taken from [114]

At lower energies the cross-sections for anti-neutrinos are smaller than those of neutrinos. This difference almost vanishes for very high energies (about the same at $E_\nu > 1\,PeV$ (see Fig. 3.2)). At high energies Earth becomes opaque for neutrinos [115, 116].
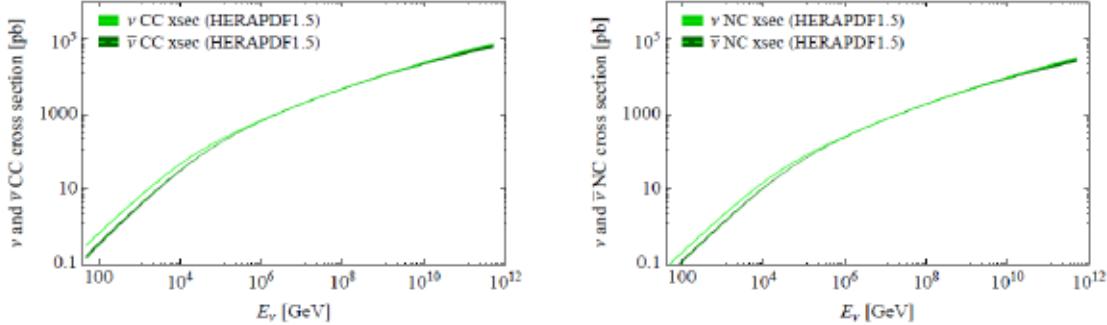
Figure 3.2: Cross-sections for charged-current (CC) and neutral-current (NC) interactions of neutrinos with an isoscalar target. Taken from [116].

Neutrinos have a flavor and a mass eigenstate. A flavor eigenstate does not have a corresponding mass eigenstate, but is a mixture of all mass eigenstates. Neutrinos oscillate between their flavor states due to their non-zero mass. These oscillations occur between all three flavor states. However, in a good approximation the probability for this can be expressed as a two flavor oscillation and is proportional to [87]:

$$P_{\nu_\alpha \to \nu_\beta} \sim \sin^2\left(\frac{\delta m_{ij}^2 L}{4E}\right). \tag{3.1}$$

Here α and β are two flavor eigenstates and δm_{ij} is the difference of the squared masses, L is the distance for which the oscillation probability is calculated and E the energy of the neutrino.

Even if the neutrino energy can be determined with good precision, the distance between the point of neutrino emission in an astrophysical source and detection will be impossible to be determined. The usual astrophysical source is of such large size compared to the oscillation length that $\sin^2$ term in equation 3.1 averages to $\frac{1}{2}$. Hence, a direct calculation of which neutrino mixing is expected on Earth, depending on the initial neutrino flavor composition at the source and the mixture and the degree to which the mass and flavor eigenstates are mixed but independent from E and L, is possible.

As discussed in section 2.2.3 neutrinos are expected from the decays of pions and muons. Without any other assumptions this gives a ratio of ($\nu_e = 1 : \nu_\mu = 2 : \nu_\tau = 0$) at the source. At Earth the ratio becomes $(1 : 1 : 1)$ after accounting for mixing [117].

Most models predict the production of ν_τ at the source to be very small or even neglect it. Due to the mixing however, a contribution of ν_τ at Earth is expected for all models discussed here.

If the muons produced in the pion decay lose significant energy in magnetic fields at the source (damped muons) the ν_μ and ν_e produced in their decay are of lower energy. Thus, the ratio for HE neutrinos becomes (0 : 1 : 0) at the source. Another possible scenario are sources where the dominant process of neutrino production is the decay of neutrons – leading to a (1 : 0 : 0) ratio. Table 3.1 shows the relation between the neutrino flux at the source and the Earth.

Table 3.1.: Initial composition of ($\nu_e : \nu_\mu : \nu_\tau$) and composition after mixing. Values taken from [117]

	Initial	After mixing
normal pion decay	1:2:0	1:1:1
damped muons	0:1:0	4:7:7
neutron decay	1:0:0	5:2:2

Depending on the energy and the necessary environmental conditions (density, magnetic fields) some source classes can be favoured or excluded for certain flavor compositions [118].

3.1.2. The Cerenkov effect

If a particle moves through a medium with a velocity v higher than the speed of light in this medium it begins to emit photons [119]. This effect is named after its discoverer PAVEL CHERENKOV. The speed of light in the medium is defined by the speed of light in vacuum c over the refractive index n. These photons are emitted in a specific angle, the so called Cerenkov angle $\cos(\theta) = \frac{c}{vn}$. The number and wavelength of the emitted photons are dependent on the charge of the particle. As one can see in 3.2 the number of photons is dependent on $dE = hdv = hc\frac{d\lambda}{\lambda^2}$ [120]:

$$\frac{d^2N_\gamma}{dxdE} = \frac{\alpha z^2}{\hbar c}\left(1 - \frac{1}{\beta^2 n^2}\right)$$ (3.2)

Thus, photons with smaller wavelengths are produced in higher numbers than photons with larger ones. For water (n =1.33) and ice (n = 1.31) the properties are rather similar. Roughly 200 emitted photons per cm in the range of the visible light ($\lambda = 400\,\text{nm}$ to $700\,\text{nm}$) are expected. The energy loss due to the Cerenkov effect is small compared to the overall energy loss of the charged particle [120]. The refractive index is not constant, but changes for light with different wavelength. For X-rays the refractive index approaches one [121] and no Cerenkov light is emitted.

3.1.3. Energy losses of charged particles

The energy losses of relativistic charged particles heavier than the electron in matter can be separated into two parts [122]. On the one hand, the charged particle loses energy by ionization of the target material. On the other hand, it loses energy over the so-called radiative processes Bremsstrahlung, pair production, and photo-nuclear interactions. For muons, which are of particular interest in the scope of this thesis, the average energy loss for $E_\mu > 1\,\mathrm{GeV}$ can be parametrized as follows:

$$-\left\langle \frac{dE}{dx} \right\rangle = a(E) + b(E)E, \qquad (3.3)$$

where the parameter $a(E)$ represents the ionization part and $b(E)$ the radiative one. The "critical energy" is defined as the energy for which the contribution of both parts to the total energy loss is equal (about $1\,\mathrm{TeV}$ for muons in water). At higher energies the radiative losses dominate the total energy loss, see Fig. 3.3. This has a large influence on the "topology" or profile of the overall energy losses along a particle track. While losses of ionization are rather constant, the particle can loose a large part of its energy in a single radiative interaction. Therefore, the radiative losses per unit distance are of a more stochastic nature.
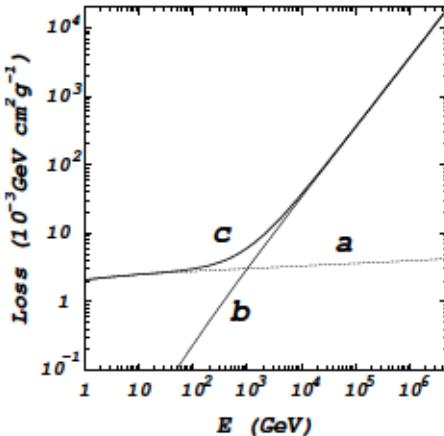
Figure 3.3: Energy loss of muons in water depending on the muons momentum. Taken from [123].

3.1.4. Signatures

Depending on the type of interaction and neutrino different light patterns of Cerenkov light are produced from the energy losses of secondary particles discussed in the two sections above.

In any interaction hadronic particles are produced which interact fast again with

nucleons and cascade down to lower energies [124]. Such a cascade extends for a few meters at 100 TeV neutrino energy and about 200 m at 10 EeV [125]. As long as secondary charged particles in these interactions are fast enough, they emit Cerenkov light. Similar to the air showers discussed in section 2.2.1 an electo-magnetic component is produced as well, increasing the light yield [124]. Scattering of photons leads to an almost isotropic light distribution after 25 m in the ice of the IceCube detector [125]. Hence, for larger distances from the interaction vertex the emission appears almost spheric. A neutral-current cascade is depicted in Fig. 3.4 A.

In a neutral-current interaction the neutrino can carry a large part of its energy away. While in charged-current interactions the median of the sum of the energies of the produced lepton and the hadronic cascade at the interaction vertex is larger than 90% of the neutrino energy, for neutral-current interactions its about 30% [126].
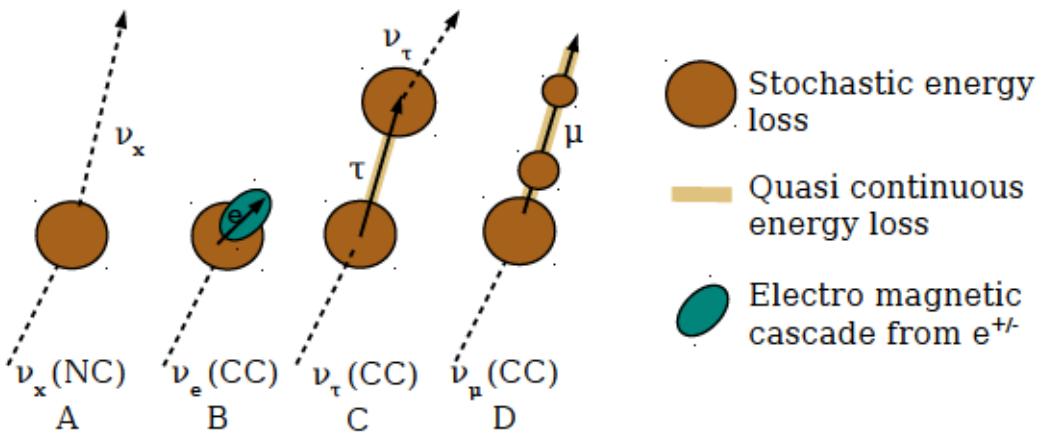
Figure 3.4: Schematic representation of the four neutrino interaction signatures of neutrinos detectable with an IceCube-like detector.

For charged-current interactions of electron- and tau-neutrinos the produced patterns of photons are very similar to the case of neutral interactions. However, in case of the electron there is an additional electromagnetic cascade (see Fig. 3.4 B). In case of the tau-neutrino the pattern depends on the energy of the neutrino. For sub PeV energies the tau decays fast[1]. If a muon is produced in this decay, the pattern will look similar to that of the interaction of the muon neutrino discussed below. In the other cases the additional hadronic and electromagnetic cascade of particles just adds more Cerenkov photons.

At very high energies the produced tau can travel for distances that are outside

---

[1]$c\tau = 87.03\,\mu m$, $m_\tau = 1.776\,GeV$ [15]. Hence, a tau with energy [1 TeV, 10 TeV, 100 TeV, 1 PeV, 10 TeV] can travel is (about) [0.05 m, 0.5 m, 5 m, 50 m, 500 m]. This calculation ignores the influence of energy losses.

the range of the electromagnetic or hadronic cascade. This would lead to a so-called "double bang" event (see [127] and Fig. 3.4 C) with two bright cascade-like signatures connected by a track.

In case of a muon neutrino interacting with a nucleon over a charged-current interaction a muon is produced as secondary particle. Usually, a large part of the neutrino energy is transferred to this muon. These high-energetic muons can travel for several kilometres through a medium like ice or water before they lose their energy as described in section 3.1.3. Along this track they emit Cerenkov photons. Additionally, they can interact with the matter along this track and lose energy through processes like pair-building or ionization [128].

Along the track of the muon secondary particles are created in these processes. It is known from simulations [129] that most of the secondary particles travel in the direction of the muon. Hence, also the majority of their Cerenkov light is emitted in the same angle as for the initial muon track, increasing the overall light yield. Some of these processes can lead to the momentum transfer of a large part of the muons momentum to the nucleon it is interacting with on a stochastic basis. At these positions cascade like patterns emerge (see Fig. 3.4 D). This leads to a track-like signature with high stochastic losses along it [130].

In general, the long track-like signatures created in charged-current muon-neutrino interactions can be used to reconstruct the direction of the interaction better than the spheric signatures of neutral-current interactions or charged-current interactions of electron- and tau-neutrinos. An exception is the case of tau-neutrinos producing a tau / muon with a long track-like signature.

Additionally, muons with TeV energies can travel several kilometers before they decay (see Fig. 3.5). This has two consequences: Muons produced in the atmosphere (see section 2.2.1) can penetrate the Earth several kilometres deep and muons produced in neutrino charged-current interactions can propagate through a medium and reach the detector from the outside, increasing the number of signatures of this type in the detector volume compared to spheric interactions. Both the larger number of track-like signatures and their superior angular reconstruction makes them the preferred choice in searches for point-like sources.

While the neutrino direction cannot be reconstructed as well from the spheric emission (types A and B in Fig. 3.4), the energy reconstruction is easier since the entire energy deposited in the initial neutrino interaction and the secondary processes is inside or in the vicinity of the detector. For the long track-like signatures this is not the case. In this case, the deposited energy in the detector is not equivalent to the total energy deposited
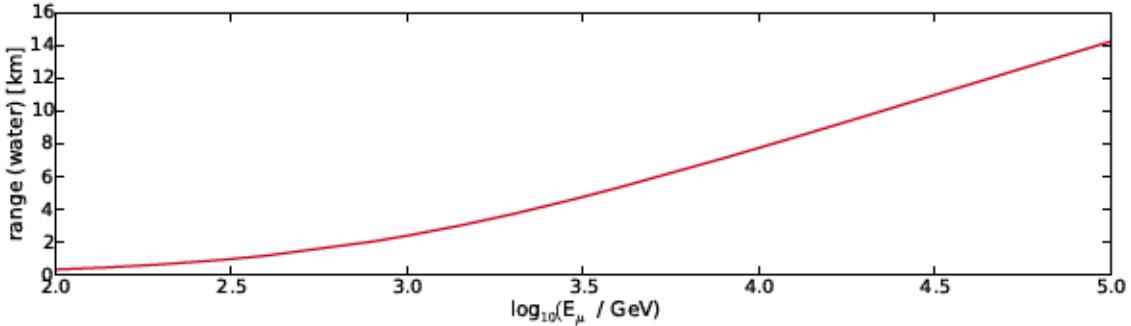
Figure 3.5: Range of muons in water, dependent on energy. Values taken from [122].

making an estimate on the initial neutrino energy more challenging. A discussion on how to reconstruct both energy and direction of a muon track can be found in section 5.2.

3.1.5. Propagation of photons

As seen in the section above, the neutrino properties such as energy and direction can be estimated only if one is able to detect enough of the photons that are produced. The number of expected VHE neutrinos is small. Thus, large detector volumes are required. Both financially and technically, the number of detection units one can deploy in this large volume is restricted. Therefore, photons have to propagate for several tens of meters in the current detector generation, if they are far away from a detection module. For such long distances both scattering and absorption are important properties of any potential detector material.

Volume-wise Mtons or even Gtons of material are required. This limits detector designs to regions of the Earth were such quantities of a potential material are already in place. Both the needed size and the necessary optical properties make water or ice strong choices as detector material. Additional requirements are power-supply, data transfer, and enough depth to reduce the background of muons produced in the atmosphere which can create signatures similar to those of muon neutrinos at a much higher rate. The combination of all these requirements leads to two kinds of environments for potential experimental sites: Deep water like the sea (not too far away from the shore) or deep lakes (like lake Baikal) and the glaciers of Greenland and the Antarctic continent [131].

3.2. Neutrino telescope projects

All telescopes discussed here operate via the detection of Cerenkov light via photo-multiplier tubes (PMT) that are part of optical modules (OMs). These OMs are connected via cables for fixation, data transfer and power supply. A unit of these cables and OMs is called a string. In the following, a few milestone experiments looking for astrophysical neutrinos are discussed.

All experiments have to overcome the background of atmospheric neutrinos and muons discussed in section 2.2.1 to detect astrophysical neutrinos. Additionally, there are other processes like bioluminescence (not in ice) as well as radioactive decay in the OMs and their vicinity that can also produce light and hinder detector operations as "noise". In the case of ANTARES, a detector discussed in the section below, the additional light emitted by biological luminescence can increase the amount of data taken by a factor of ten in phases of high biological activity and ultimatively leads to phases with lower sensitivity to astrophysical neutrinos [132]. For a more comprehensive overview the historical review by SPIERING [133] is recommended.

3.2.1. DUMAND, ANTARES and KM3NeT

With both large depth and volume, the oceans are a somewhat natural choice for neutrino telescopes. First planned was the DUMAND detector near Hawaii [134]. Designed to be a km^3- volume detector several thousand meter below the surface the project run in both technical and financial problems and was abandoned in 1995 – after the first deployed string ceased to work shortly after deployment.

Experiments in the Mediterranean sea were more successful. Starting with the deployment in 2001 near the shore of Toulon, France, ANTARES is completed since 2008 [132]. A group of three OMs is installed on a optical module frame (OMF). The distance along a string between two OMFs is about 14.5 m (see Fig. 3.6). ANTARES is formed by 13 strings. Eleven of them have 24 OMFs, starting 100 m above the ocean's floor (2475 m below sea level). One has only 20 OMFs and additional sensors for acoustic neutrino detection. The last string is used for the measuring of environment variables.

Due to sea currents the position of the OMFs is not fixed. However, the position is monitored by an acoustic sensor system continuously. While measurements of atmospheric muons and neutrinos are possible, the small size of the detector (about $0.01\,km^3$) severely limits the potential to measure an astrophysical neutrino flux [135]. Decommissioning of the detector is planned in 2016.

ANTARES will be followed up by the KM3NeT detector [136, 137]. It will consist out of several building blocks. The building blocks are optimized for different science goals. One block is planned for low energy measurements (GeV) of particle physics properties of the neutrino (ORCA). It will be built in vicinity of the ANTARES detector. Another building block is planned near the shore of Sicily. This one is optimized for the detection of high-energy neutrinos (ARCA). Construction of both sites has begun. Depending on funding up to six building blocks are envisioned.
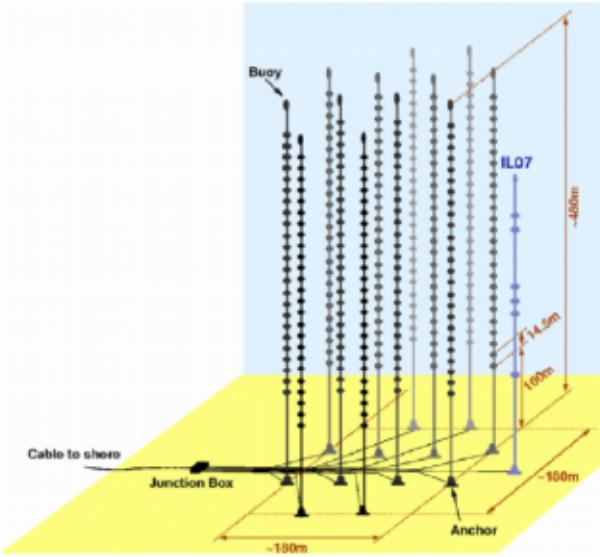
Figure 3.6: Layout of the ANTARES detector. Taken from [132].

3.2.2. Baikal experiment, NT200 and GVD

The detection of neutrinos in water is not limited to the oceans. However, the requirements limitthe possible sites in lakes. So far, only in lake Baikal a neutrino telescope has been successfully operated. In 1981, first experiments started in shallow water [138]. They were followed by the construction of the NT200 detector. Deployed at the bottom of the lake in a part with depths of about 1370 m, 192 optical modules are attached to eight strings. The distance between these strings is 21.5 m and the height of the string 72 m. Thus, the instrumented volume is about $0.0001 \, \text{km}^3$ – about a factor 100 smaller than the ANTARES detector.

The deployment of a much larger detector, the Baikal Gigaton Volume Detector (GVD) has begun. GVD is planned to have 216 strings, each string holding 48 OMs. The completed detector would then have an instrumented volume of about $1.4 \, \text{km}^3$ [139].

3.2.3. AMANDA

The last environment for neutrino telescopes discussed here is the Antarctic ice. Deployment of the Antarctic Muon and Neutrino Detector Array (AMANDA) started in the 1990s. First AMANDA A was deployed, consisting of four strings each carrying 20 OMs. The OMs were deployed in depths between 800 m and 1000 m. However, air bubbles led to large scattering of photons in the ice at these depths and made a reconstruction of muon tracks infeasible.

Thus, the next ten strings, AMANDA B, were deployed in depths between 1545 m

and 1978 m. Deployment ended with the additional eight strings of AMANDA II positioned around AMANDA B. Three of these strings had OMs deployed as deep as 2350 m. Thereby ice properties at these depths could be investigated – a foreshadow of the already planned IceCube detector. AMANDA was successful in showing that the detection of neutrinos in ice is possible. However, similar to ANTARES, its size (about $0.02 \, \text{km}^3$) limited it to the detection of atmospheric neutrinos [140, 141].

3.3. The IceCube Neutrino Observatory

After the successful operation of the predecessor AMANDA, plans for a much larger detector were made. Finishing the deployment of optical modules in 2010 the IceCube detector is nowadays the largest detector of this type in the world. The detector is equipped with 5400 modules. Each module consists of a 25 cm PMT[2] [142] and a main board for data acquisition. The measured analogue signal by the PMT is digitalized before it is sent to the surface. The module as a whole is called DOM (Digital Optical Module) and will be discussed after an description of the detector layout.

3.3.1. Deployment and layout of the IceCube detector

The DOMs are fixed to a 2500 m long cable, the string. The string provides power-supply and communication for the attached DOMs. Each string holds 60 DOMs [143]. Most of the strings (78) are oriented in a triagonal grid with 125 m spacing and the 60 DOMs are deployed in depths between 1450 m and 2450 m (see Fig. 3.7).

In the center of IceCube eight strings are deployed more densely (between 40 m and 70 m apart). In contrast to the other strings their DOMs are equipped with PMTs with a higher quantum efficiency. Additionally, these DOMs are not deployed between 1450 m and 2450 m. Ten of the DOMs are deployed between 1760 m and 1850 m; the other fifty are deployed between 2100 m and 2450 m deep in the ice. This part of the detector is optimized for a lower threshold energy (about 10 GeV instead of about 100 GeV) and is called DeepCore. The IceCube Neutrino Observatory is completed by a surface array called IceTop. It consists of 81 stations in a triangular grid with the same 125 m spacing as IceCube. Each station is made of two tanks with clear ice in them. Every tank hosts two DOMs. The array can detect the showers of cosmic rays.

3.3.2. The Digital Optical Module - DOM

The environment in which the DOMs are deployed dictates several of the DOMs properties. It should not require more than five Watts of electrical energy due to high fuel costs at the South Pole. Additionally, it has to be built robust enough to withstand the pressure and temperature conditions present deep in the ice. For practical reasons

---

[2]Hamamatsu R7081-02
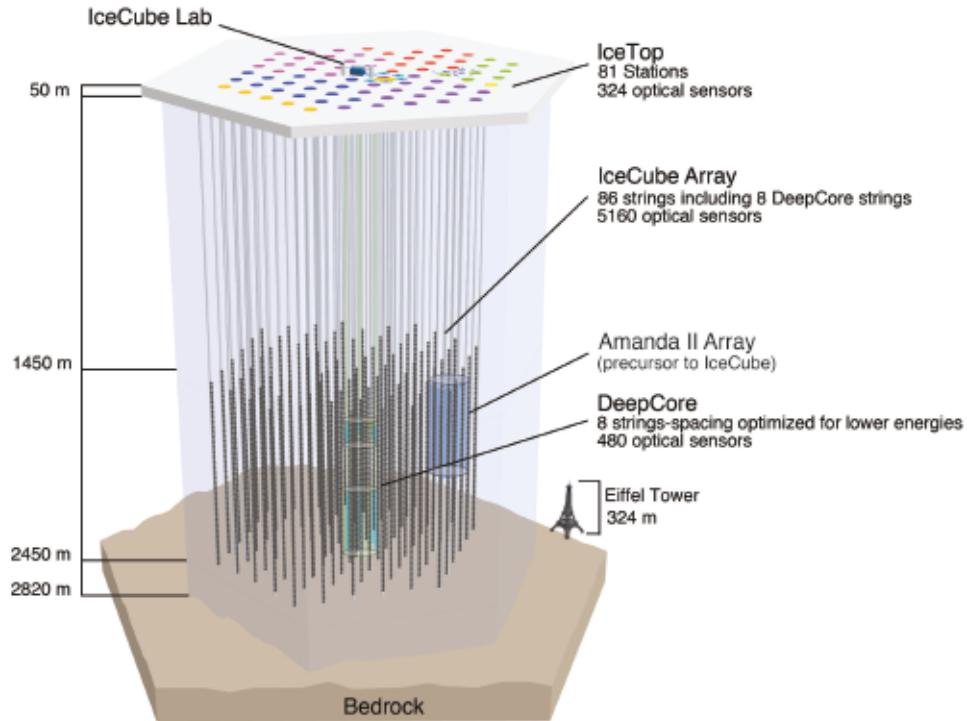
Figure 3.7: The IceCube Neutrino observatory, consisting of the IceCube detector, the low-energy extension DeepCore and the air shower detector IceTop, is deployed a the geographic South Pole. Also shown is the predecessor AMANDA. Taken from [144].

the DOM has to work at room temperature ($20\,°\mathrm{C}$) during testing as well as at $-55\,°\mathrm{C}$ when it is transported to and deployed at the South Pole [143]. To minimize the dark noise by natural radioactivity the material (mainly the glass sphere) the DOM is made of had to be chosen accordingly. Another important property is the reliability. Since the ice refreezes after deployment, the DOMs can not be physically accessed afterwards. Therefore, every DOM with a fatal hardware or software error remains lost.

These requirements are met by the chosen design. To resist the high pressure in the deep ice the DOMs housing is made out of two glass half-spheres with a thickness of $13\,\mathrm{mm}$ and a diameter of $35.6\,\mathrm{cm}$. The PMT, pointing downwards, and the mainboard are fixed in the sphere, see Fig. 3.8. To improve the optical coupling between PMT and sphere a special silicone-based gel is used.

Light emitted at a position higher than the DOM has to be scattered before detection. If a photon reaches the DOM, it can be detected by the PMT as charge. The charge over time, measured by the PMT, is then digitized. There are two ways a signal

can be digitized [145, 146].
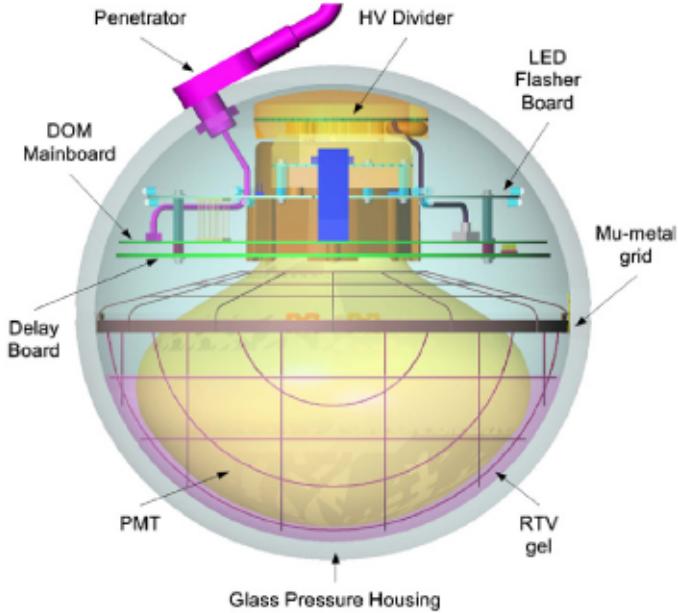
Figure 3.8: Schematic drawing of the Digital Optical Module. Taken from [142].

One is digitization by a fast Analogue to Digital Converter (fADC). This fADC samples the signal taken by the PMT with a rate of 40 Mega samples per second (MSPS). If the fADC gets triggered, 256 samples are recorded, covering a time interval of 6.4 µs.

For a higher time-resolution two Analog Transient Waveform Digitizer (ATWDs) are used. They sample the PMT signal with 300 MSPS and can record 128 samples, covering a time interval of about 400 ns. Three ATWD channels are operated in parallel with different amplifier gains, to improve the dynamic range that can be recorded . The second ATWD can digitize, if the first one is in dead time.

The detector was planned assuming a DOM survival rate of 90 percent after 15 years. Up to date the number of lost DOMs is about 120 (about two percent) – eleven years after the deployment of the first string and almost six years after the deployment of the last.

3.3.3. Ice properties at the South pole

The ice between 1450 m and 2450 m is very clear leading to an effective absorption length larger than 70 m and an effective scattering length larger than 20 m in most parts of the detector (see [147, 148]) and Fig. 3.9). However, the ice-properties are not homogeneous. In the past there were several periods of high concentration of dust particles in the Earth's atmosphere. Nowadays this can be observed as "dust layers" in the ice. In these layers

the scattering and absorption length are much smaller due to the unclean ice (see the range between 1800 m and 2000 m in Fig. 3.9). Therefore, less light is detected from interactions of muons/neutrinos in this region.
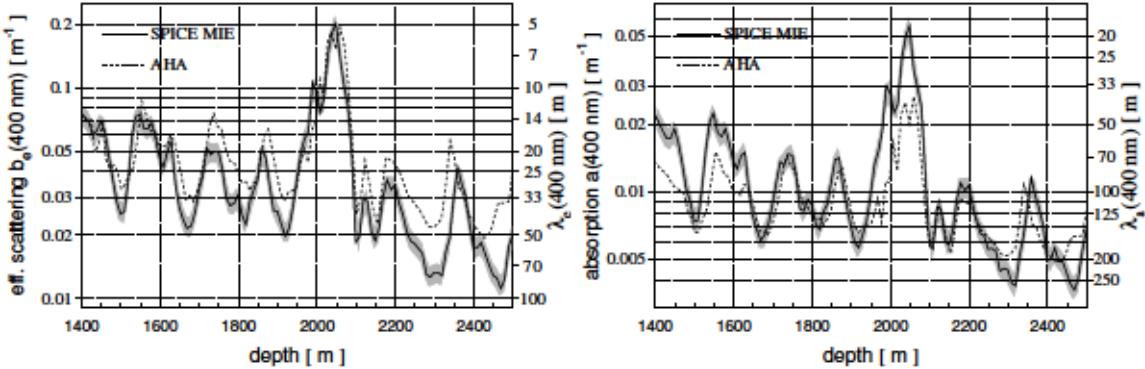
Figure 3.9: Effective scattering coefficient(left) and absorption (right), dependent on depth, for two models describing the optical properties of the ice in IceCube. Taken from [148].

3.3.4. Data acquisition at the South Pole

Each DOM is connected to the two DOMs below and above it. If one DOM detects charge over a threshold of 0.25 Photoelectrons (PE) with a discriminator trigger, it will start data sampling with the fADC and one of the ATWDs. It will also check if its neighbours (the two DOMs above and below him) registered charge above this threshold in a time window of 1 µs as well. If this is true, these readouts will be then marked as "local-coincident" or LC.

Between three and eight DOMs must have observed LC readouts within 5 µs for an event to be triggered. If the trigger condition is fulfilled the read outs from the entire detector will be recorded, which defines an event. Readouts that fulfil the LC condition are stored completely (both ATWD and fADC data). For all other readouts only the three highest samples of the first 16 fADC samples are kept.

The data of the readout is then sent to a facility at the surface. The total trigger rate is about 2.5 kHz [149]. This rate can vary by ~ ±10% due to yearly atmospheric variations [150]. The interpretation of raw ATWD and fADC is challenging for most used reconstruction algorithms. Hence, for triggered events this information is used to deconvolve specific single PE shapes [151]. Afterwards the events are reconstructed with relatively simple, but fast algorithms applied on this extracted time and charge information (pulses) and afterwards pre-selected (filtered). The filtered events are sent via satellite for further processing with more time consuming reconstructions.

3.4. Detector simulation and background estimation used for this analysis

Simulated neutrinos are required to estimate the quality of the used reconstruction methods, to design the event selection and to calculate sensitivities and upper limits. The background of atmospheric events is estimated using data. This has the advantage that systematic uncertainties (for example the normalization of the atmospheric muon flux in IceCube) do not have to be taken into account for the background estimation. The aim of this analysis is to measure emission from point-like sources, not a diffuse emission. Since it is not expected to cluster in space, a precise estimation of the atmospheric background is not necessary . The influence of systematic uncertainties on the signal simulation is discussed in section 6.3.

However, to verify the variables used in the event selection simulated air showers are used for comparison. In this analysis several simulation data sets are used. While some of there parameters differ, for example the type of particle simulated (neutrinos/muons) or the generated energy spectrum, the overall simulation chain remains the same.

First, either simulated muons or neutrinos are "created" using a generator. For neutrinos a generator based on the software package discussed in [152] is used. The probability of a neutrino to interact in the simulated volume is very small. To avoid simulating many events that leave no trace in the detector the generator forces the neutrino to interact inside the detector or in the vicinity of it. Atmospheric muons are taken from the air shower simulation software CORSIKA [153].

In a second step, the propagation of the muons created in either of the generators is simulated using the software described in [128, 154] [3]. The energy losses inside and in the vicinity of the detector are then used to estimate the light yield of an event. Using parametrizations of the number of expected photons from an energy deposition these photons are then propagated. This propagation depends on both scattering and absorption length of the ice. For the simulations used in IC86-I the SpiceMIE model from [148] is used. For IC86-II+ an improved version of this model which includes the observed anisotropy[4] [155] of the ice where IceCube sits is used. For most simulation data sets all photons were propagated using the propagation code described in [156].

In IC86-I signal simulation with high statistics for neutrino events above $1\,\mathrm{PeV}$ is used. The propagation of all single photons is computational very expensive. Hence, parametrized look-up tables [157] are used here that are faster, but less precise.

---

[3][128] is used for simulation of the first year of this analysis and [154] for the following years two to four. The main difference is the programming language of the propagation.

[4]An azimuth dependence of the light yield.

The response of the OMs to arriving photons and noise is simulated next and in a last step the same triggers that are applied on data are also applied on the simulation.

4. STeVE – a search for point-like TeV neutrino sources in the southern sky

This chapter starts with a description of the observed VHE gamma ray sources. As will be shown in section 4.1, the majority of galactic VHE gamma sources has been discovered in the southern sky. The implications of this for IceCube will be discussed in section 4.2. The search strategy described in this thesis, a search for neutrino emission from point-like sources with Starting TeV Events (STeVE), is presented in section 4.3 and an overview of previous searches for point-like sources in the southern sky is given in section 4.4.

4.1. Gamma ray sources in the southern sky

About fifty percent of known TeV sources, listed in the TeVCat[1] [26] catalogue are found in the southern sky. From 90 sources that are located in the galaxy, 57 are in the southern sky[2]. This includes the center of our galaxy and the two examples RXJ1713 and VelaX discussed in section 2.5.1. As demonstrated in Fig. 4.1 the observed objects are not equally distributed over the sky. While the HESS colloboration surveyed
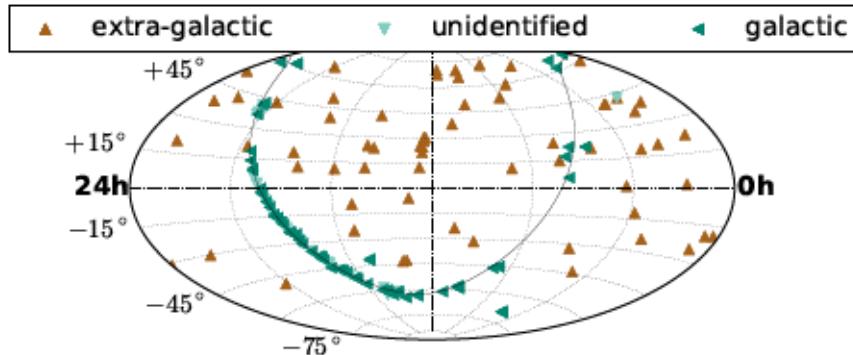
Figure 4.1: Skymap of sources in TeVCat. The galactic plane is indicated by the solid black band.

most of the galactic plane [64] VERITAS and MAGIC did not. Thus, they had more observation time available for other sources. This is represented by the fact that more extra-galactic sources have been found in the northern sky so far, while an isotropic distribution of these sources would be expected. The second important feature is the

---

[1]http://tevcat.uchicago.edu/
[2]The numbers quoted here are based on the status of the TeVCat in August 2015.
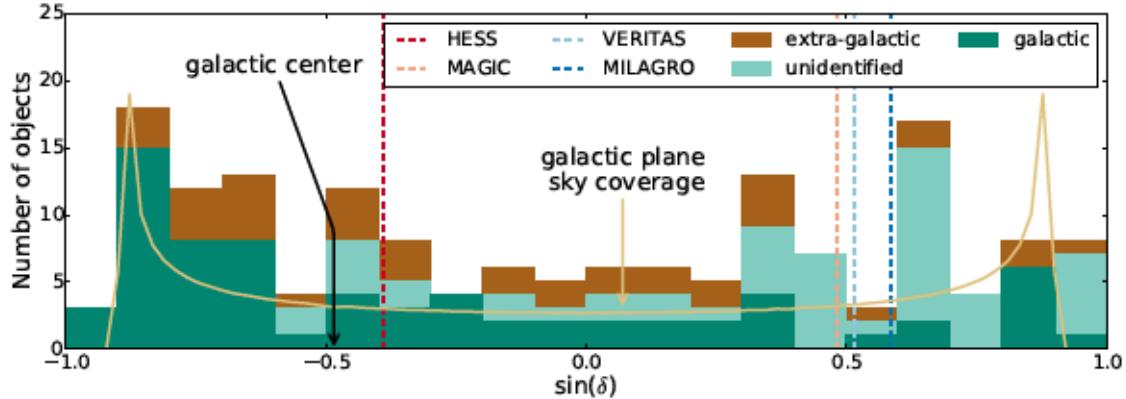
Figure 4.2: Declination of sources in TeVCat and gamma ray telescopes.

large number of objects detected around $-60°$, see Fig. 4.2. A likely explanation is the increased coverage of the galactic plane in at that declination (equatorial coordinates). Most of the unidentified objects are very close to the galactic plane; suggesting a galactic origin.

The abundance of galactic TeV gamma ray emitters and the fact that they can be seen as an indicator for TeV neutrino emission in the case of an hadronic origin (see section 2.5) are strong arguments to focus a search for the sources of the astrophysical neutrino flux on the southern sky.

4.2. Challenges for IceCube

Muons cannot cross Earth. Thus, a muon track that goes up through the detector, as if it would come from the northern sky, must come from a neutrino interaction. Most of these neutrinos are produced in interactions of cosmic rays in Earth's atmosphere, as discussed in section 2.2.1. In the southern sky IceCube looses the Earth as a shield against atmospheric muons. Here, the main background for searches of astrophysical neutrinos is not atmospheric neutrinos, as in the northern sky, but atmospheric muons.

These muons are about a facto 10^6 times more abundant than atmospheric neutrinos (see Fig. 4.3), but the atmospheric muons have a very steep spectrum. This and the fact that opaqueness of Earth for high energy neutrinos does not play a role in the southern sky searches for neutrinos with energies of PeV or higher with through-going[3] muon tracks leads to comparable sensitivity with searches in the northern sky in this energy range [158].

For neutrino energies below 100 TeV however, these searches are about a factor 1000 worse than in the northern sky [159]. Due to the fact that many of the galactic sources in the southern sky are expected to have either a cutoff in energy somewhere

---

[3]A track-like signature that enters and leaves the detector volume.

below $E_\nu = 100\,\mathrm{TeV}$ or a steep spectrum [97] an IceCube search with through-going muon tracks is not very promising for these sources.
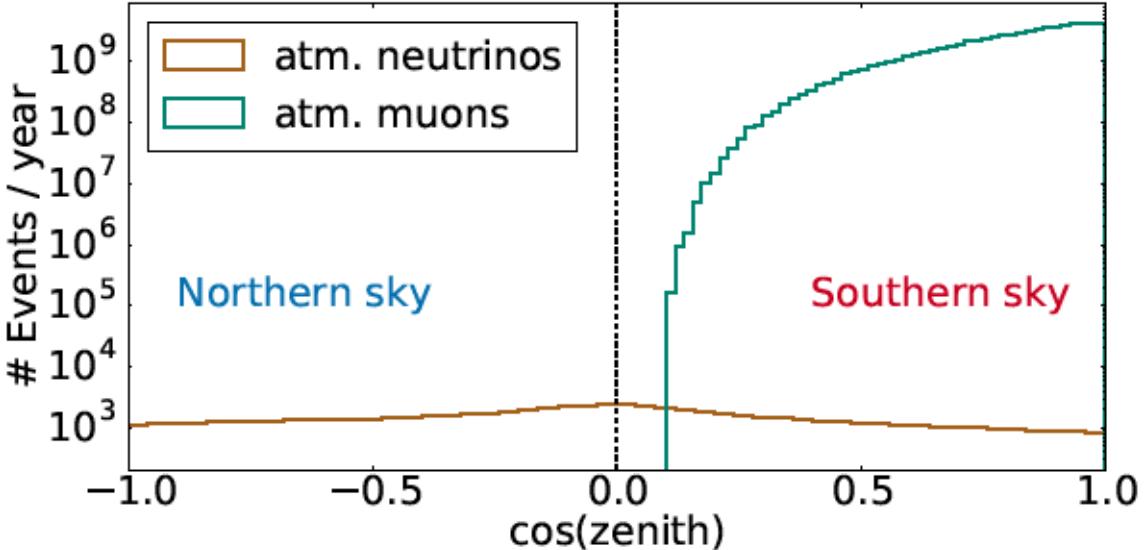
Figure 4.3: Number of atmospheric muons and neutrinos expected in one year of live-time of the IceCube detector. The numbers are taken from Monte Carlo simulation.

4.3. Strategy of this work

4.3.1. Starting tracks

If one or more muons, produced in a cosmic ray air shower, are of sufficient energy to produce a hit pattern that appears to enter and leave the detector volume, this will be called a through-going event. Similar muons created in interaction of neutrinos outside the detector volume can produce such a hit pattern. As a result for a single muon track in this case it will not be possible to say whether it origins from a cosmic ray or a neutrino interaction [4].

Atmospheric muons can only be produced in the atmosphere and have to enter the detector volume. The neutrino on the contrary has no track-like signature, thus, a track that starts within the detector volume – a **starting track** – can be observed. If the scope is set to only these events where the neutrino interacts within the detector volume, ideally, an unambiguous signature for a neutrino interaction will be at hand.

This unique signature comes with a drawback. Through-going tracks can be de-

---

[4]Given that the initial neutrino interaction is sufficiently far away from the detector volume.

tected even if the initial interaction is several kilometers away, depending on the energy and thus, range of the muon. For starting tracks this is not longer true. This decreases the volume that is available for the neutrino analysis.

4.3.2. Atmospheric self veto

One advantage of starting tracks is the potential suppression of atmospheric neutrinos. This has been discussed in detail in [160, 161] and is summarized here. The hit patterns in the detector for neutrinos from the northern sky are the same for astrophysical and atmospheric neutrinos. A separation is only possible on a statistical basis due to the different expected energy spectra (and position, in the case of source searches).

In the southern sky however, also tracks produced by the muons from the cosmic ray shower that produced the neutrino are expected to be visible. These muons would overlay with the starting track of the atmospheric neutrino and it would be easy to reject the combined track as through-going. Therefore, a perfect rejection of through-going tracks would provide a sample of pure astrophysical events. As can be seen in Fig. 4.4, the efficiency of such a veto is both dependent on energy and zenith angle of the event. The more horizontal an event is, the less efficient becomes the veto. Likewise, a higher energetic atmospheric neutrino has a larger probability to be accompanied by a more energetic muon. This muon has a higher chance to both reach the detector and to be energetic enough to make a veto possible.

4.3.3. Searching for TeV eutrinos from point-like sources

In the southern sky the background by atmospheric muons exceeds the second largest background of atmospheric neutrinos by roughly a factor 10^6 (see Fig. 4.3). These muons are still abundant in large number at the TeV energies where galactic neutrinos are expected. Thus, a separation based on the energy alone does not seem to be promising. In almost all searches for point-like sources in the southern sky with IceCube the majority of events are atmospheric muons – see for example [149]. The challenge is to suppress the number of muons enough for a clustering of neutrino events from a point-like source to be statistically significant, but it is not required to obtain a sample of pure astrophysical neutrinos induced starting muon tracks at these energies in a search for point-like sources.

Starting-tracks are a promising event topology here. Therefore, this analysis focusses on their selection to make used of both their good angular resolution and posssible suppression of atmospheric background.
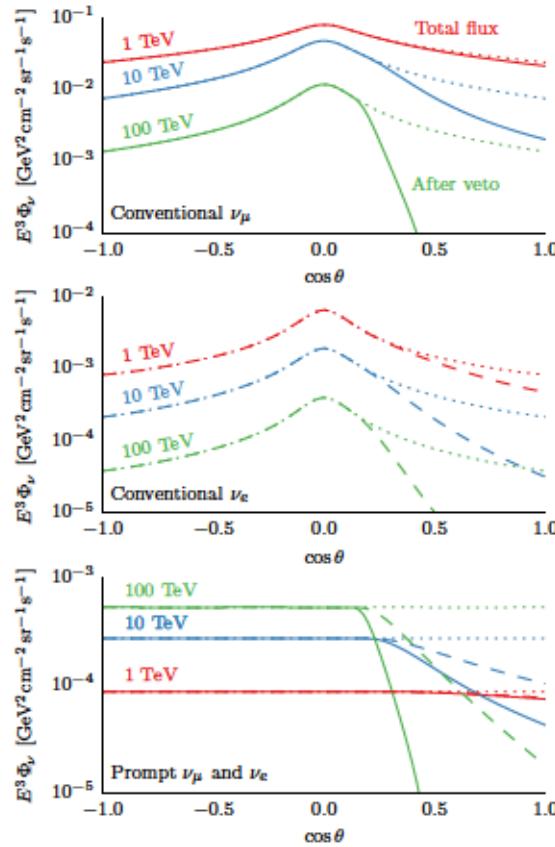
Figure 4.4: Atmospheric neutrino for three reference energies, depending on declination. Solid lines show the total flux. Dashed lines show the part of flux from neutrinos without a muon produced in the same air shower reaching IceCube. Top: Muon neutrinos from pion and kaon decays. Mid: Electron neutrinos from pion and kaon decays. Bottom: Muon and electron neutrinos produced in "prompt" decays. Taken from [161].

4.4. Previous measurements

STeVE is not the first search for point-like sources of neutrino emission in the southern sky. In the following section both results from the ANTARES detector and previous searches with the IceCube detector are discussed.

4.4.1. ANTARES results

As described in section 3.2, the ANTARES telescope operates in the Mediterranean sea. Therefore, it can use the Earth as a shield against atmospheric muons from the southern sky. The ANTARES collaboration can give the most competitive limits on the neutrino flux from many astrophysical objects observed in TeV gamma rays in the southern sky, if the connection between gamma rays and neutrinos as discussed in section 2.5.1 is assumed

[159, 162]. Even if an E^{-2} neutrino spectrum without a cutoff in energy is the hypothesis the results remain comparable to those of IceCube. The ability to compete with a detector a 100 times larger impressively shows the power of the Earth as a muon shield (see Fig. 4.5).

4.4.2. IceCube searches with through-going events

In the southern sky IceCube has searched for point-like sources with through-going tracks [149]. The number of background events is reduced to about 70,000 events (almost entirely muons) per year, by selecting events with a large charge. For an unbroken E^{-2} spectrum the result of this search is comparable with the ANTARES search mentioned above. However, if a more realistic scenario of a cutoff in energy at a 100 TeV is assumed, the IceCube analysis will lose more than a factor 100 in magnitude in sensitivity, while ANTARES will lose a factor of about two. Given the observed spectral energy distribution of the observed TeV gamma sources this is not very promising for the IceCube analysis (see Fig. 4.5).
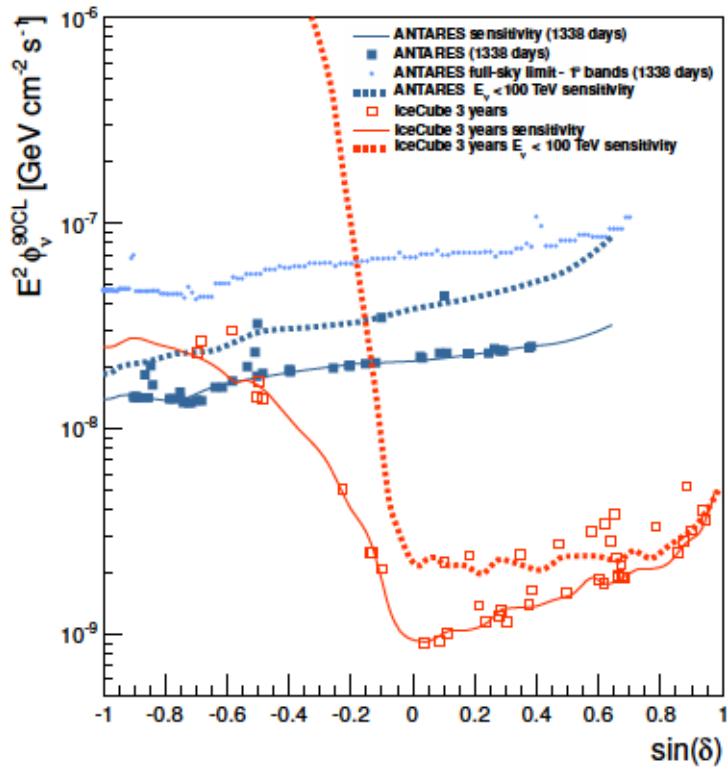

Figure 4.5: Sensitivity for point-like sources in dependence of declination for ANTARES and the IceCube search using through-going events. Taken from [159]

4.4.3. IceCube searches with starting events

High-energy starting events (HESE) Motivated by both the promising suppression of atmospheric background and the lack of evidence in the search for astrophysical neutrinos with through-going tracks an analysis was designed to specifically select events with a starting hit-pattern. The IceCube Collaboration used starting hit-patterns before, but these searches were focused on the cascade-like channel [163] or the detection of neutrino oscillations at the lower-energy threshold of the DeepCore part of the detector [164].

Thus, a new selection had to be designed to also allow for high-energy (E_ν > 30 TeV) starting events, both track-like and cascade-like. A both very simple and efficient way to suppress atmospheric background is a cut on the charge detected by the DOMs. In this analysis each event was required to deposit energy equivalent to 6000 PE or more within the detector. To select only starting-events it is required that within the time of the detection of the first 250 PE less than 3 PE are detected inside the veto region. The veto region is composed by the outer layer of strings and the highest five DOMs on each IceCube (not DeepCore) string as well as the lowest DOM on each string, see Fig 4.6.
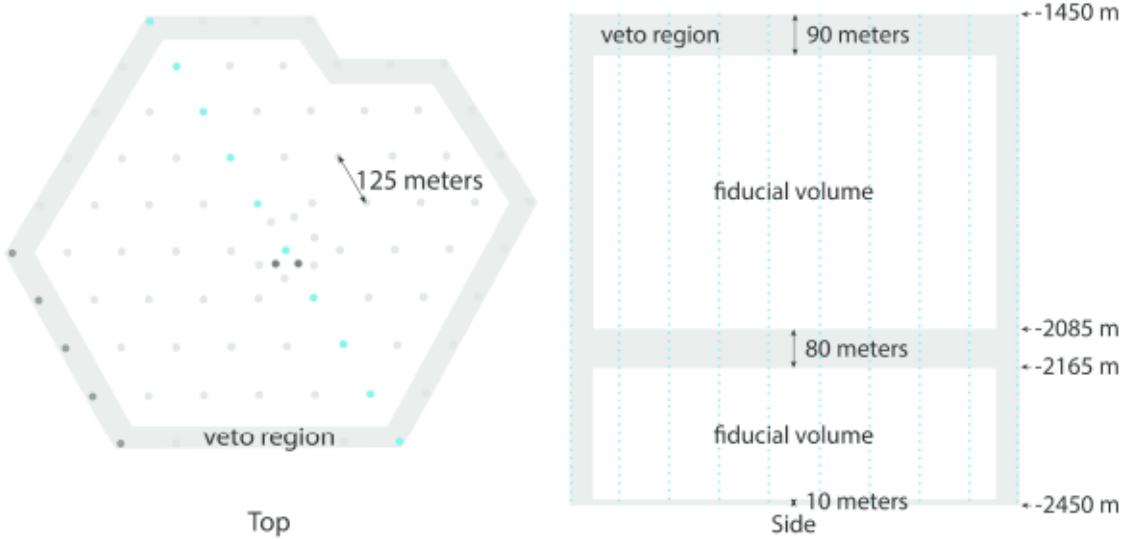
Figure 4.6: Vetoregion, taken from [89]. The dark grey strings were added in the second year used in this analysis. They completed the IceCube detector with 86 strings. The grey shaded region shows the veto region used for the completed IceCube detector. The blue dots indicate the layer of cross section chosen in the right plot.

This analysis was first performed on two years of IceCube data. One year with the almost completed detector and the first year of the completed IceCube detector

(additional seven strings). Simulations show that one expects $10.6^{+5.6}_{-3.6}$ background events from atmospheric muons and neutrinos in these two years. 28 events were detected. If the energy and zenith distribution of these events is considered this amounts to an excess of 4.8 σ over the background-only hypothesis [89]. This result was strengthened by the addition of more years of IceCube data [90].

The sample consists mainly of cascade-like events (21 out of 28). These events have a rather poor angular resolution (estimated between ~6° to ~50°). Thus, even if a point-like source had been detected, which was not the case, an identification would have been very challenging due to the large uncertainty concerning its position.

Medium-energy starting events (MESE) Motivated by the success and the limits of HESE a search for starting track-like events was designed to improve the sensitivity for point-like sources in the southern sky at energies $E_\nu < 1\,\text{PeV}$. This analysis allows for a larger contamination of atmospheric background by lowering the charge threshold of the event selection to 1500 PE. Thus, MESE focuses on medium-energy starting events (MESE). A detailed description of the analysis can be found in [165]. Additional cuts select only track-like hit patterns. These cuts exclude 77% of all cascade-like events while 95% of all charged-current ν_μ with an opening angle between reconstruction and Monte Carlo truth (Ψ) of less than five degree are kept. As a last step, a two-dimensional cut on reconstructed energy and distance of the reconstructed starting vertex to the detector boundaries is applied.

This search yields 549 events with three years of IceCube data (IC79 and two years of IC86). The analysis mainly improves the sensitivity for scenarios with a cutoff energy. For an E^{-2} power-law with an energy cutoff at 1 PeV the sensitivity of the combined through-going and starting track selection improves by a factor $\sim 2-3$ and for an energy cutoff at 100 TeV by a factor $\sim 5-20$ compared to the through-going analysis. In Fig. 4.7 the sensitivities of this combined selection are shown and compared to the results from ANTARES.

While the requirement on the deposited charge is very efficient in suppressing atmospheric backgrounds, it also reduces the efficiency for astrophysical neutrinos with energies $E_\nu < 100\,\text{TeV}$.

Low-energy starting events (LESE) The shortcoming of the three IceCube analyses presented above is their lack in sensitivity for point-like TeV neutrino emission - which is predicted in hadronic models of galactic TeV gamma sources, as discussed in section 2.5. The event selection of LESE is based on a veto condition similar to the HESE/MESE condition discussed above. The main difference is the lack of a charge threshold - making this selection also viable for events of lower energy depositing less energy in the detector volume [166, 167]. STeVE uses this initial selection developed for LESE, which will be
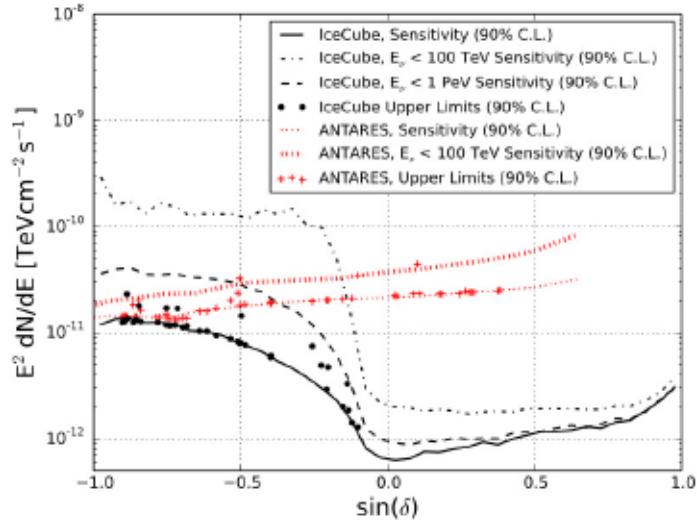
Figure 4.7: Sensitivity for point-like sources in dependence of declination for ANTARES and the IceCube search using through-going events in combination with MESE events. Taken from [165]

explained in more detail in section 5.3.1. Using additional selection levels to suppress the background further the LESE analysis is optimized to be sensitive below a few TeV.

5. Event selection and reconstruction

5.1. Motivation

It was presented in section 4.3 that selecting starting muon tracks is a promising selection to look for galactic neutrino point sources in the southern sky. This chapter discusses how to get to a data set suitable for a point source analysis. First, the methods to reconstruct event topology, energy and direction are described. Second, the individual selection steps are presented. The objective is to obtain a sample of well reconstructed signal events while suppressing background events. The last part of this chapter focusses on the properties of the event selection used in the point source analysis. **STeVE** uses four years of data taken by the completed IceCube detector. One of the energy estimators used varies between the first year (May 2011 - May 2012) and the following (May 2012 - May 2015). This leads to two event selections. Data taken in the first year will be called IC86-I and the additional years IC86-II+. If not explicitly mentioned, the provided descriptions apply to all data.

5.2. Event reconstruction and variables

5.2.1. Which properties of an event need to be reconstructed?

The **STeVE** analysis introduced in the previous chapter requires estimators of the energy, direction and topology of the event. Topology here is used as a summary of track properties. The focus of this analysis is, as discussed in section 4.3, on starting TeV muon tracks (see Fig. 5.1 a). The location of the initial interaction can be reconstructed based on the hit pattern with the methods described in section 5.2.3 and section 5.2.5. The distance between the edges of the detector volume and the reconstructed initial interaction point (*length to start*, light red line in Fig. 5.1) is expected to be positive if the vertex is inside the detector volume and negative if it is outside. A TeV muon produced by a neutrino interaction inside the detector volume is expected to leave the detector volume (*length to leave*, blue line in Fig. 5.1).

The energy deposited along the track can also be used to characterize a starting event. The energy spectrum of both atmospheric muons and neutrinos is steep (see section 2.2.1). Thus, an event with higher energy is more likely to be of astrophysical origin. The hadronic cascade of the initial neutrino interaction is also expected to be bright. Using simulated neutrino interactions and muon propagation shows that in about 80 % of all charged current muon neutrino interactions the initial cascade is the most energetic one (see Fig. 5.2). At lower energies, below $10\,TeV$, this changes to almost 90 %.
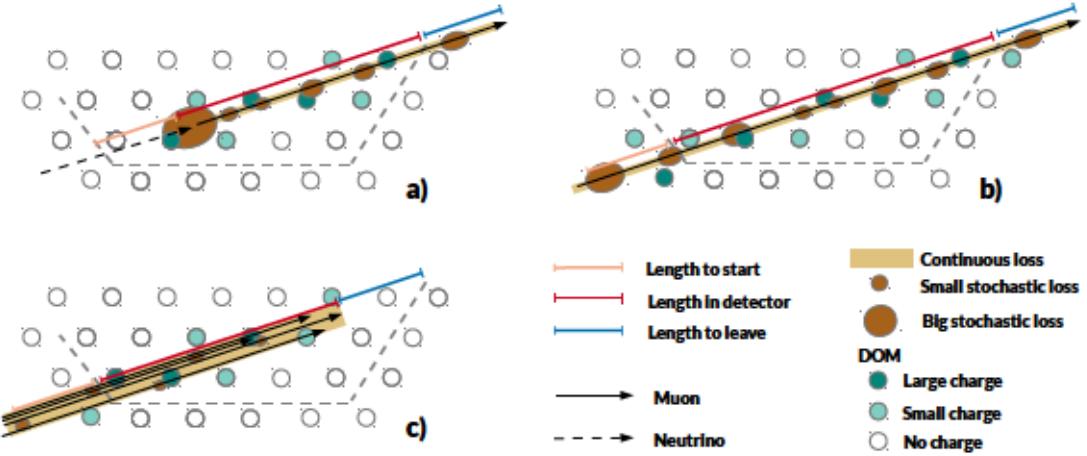
Figure 5.1: Topology of events in IceCube. a): Starting muon track b): Through-going muon track c): Low energy muon bundle. Shown are the quasi-continuous and stochastic energy losses and three track length variables.

Muons produced in an air shower often arrive in a group, a muon bundle [21]. These bundles have a more equally distributed light yield. They are on average of lower energy and a larger part of their energy is emitted continuously (see section 3.1.3 and Fig. 5.1 c).

If an atmospheric bundle consists of few, or only one, muon that carries most of the bundle's energy, the energy losses of this muon will be very similar to the neutrino induced track (see Fig. 5.1 b). If by chance this event lacks a large stochastic energy loss in the veto region of the detector, it will be very challenging to separate it from a "starting" neutrino event.

Muons from bundles produced in the atmosphere can have enough energy to penetrate the ice and enter the instrumented volume of IceCube. Some of these muons then decay inside the detector. A TeV muon produced by a neutrino interaction inside the detector volume, however, leaves the detector volume (see Fig. 3.5). Thus, a hit pattern which stops inside the detector, see Fig. 5.1 c, is an indicator for an atmospheric muon (bundle).

5.2.2. Angular reconstruction

This section about angular reconstruction is in large parts a summary of the paper describing the reconstruction methods used for the AMANDA detector [168]. Where used, additional references are given.

The direction of a muon is reconstructed with the help of likelihood reconstruc-
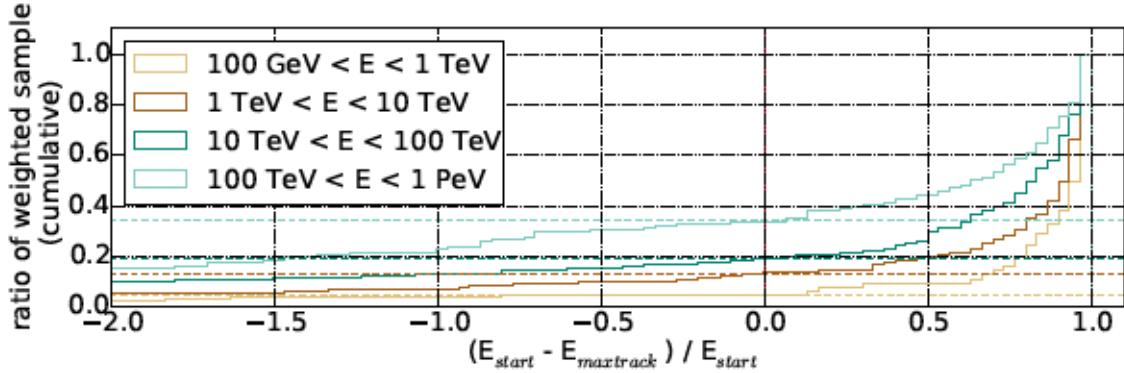
Figure 5.2: Difference between the initial energy loss at the point of neutrino interaction and the most energetic energy loss along the muon track, normalized with the energy of the initial energy loss. Simulated events in which the initial energy loss is more energetic than any single energy loss along the muon track give a value larger than zero. The cumulative distribution in four different energy bands is shown, indicated by the different colors. The dashed line of each color indicates the ratio of events in this band with an energy loss larger than the loss at the initial interaction point of the neutrino. The events in each energy band are weighted to follow an E^{-2} spectrum.

tions. These reconstructions require a first guess estimator to avoid landing in local minima of the negative log likelihood (LLH) function $-\log(\mathcal{L})$. The first guess is provided by an algorithm that minimizes the distance in space and time between a hypothetical track with a vertex and velocity vector and the positions and time of the optical modules observing charge. The angular resolution of the first guess estimator can be improved by about 60 % by rejecting detected charge that is unlikely to be in causal connection to the track [169]. This improved version of the analytical reconstruction is used for IC86-II+.

In a next step the estimated track information can be used as a seed for the LLH track reconstruction. The optical modules that detected charge can be seen as independent measurements of the track hypothesis. A likelihood $\mathcal{L}$ can be defined by multiplying the probability density functions p (PDFs) for each individual measurement x_i:

$$\mathcal{L}(\vec{x}|\vec{\Theta}) = \prod_i p(x_i|\vec{\Theta}). \tag{5.1}$$

Here, $\vec{x}$ is the vector of all measurements and $\vec{\Theta}$ contains the free parameters of the track hypothesis, the vertex position (x, y, z) and the direction of the track (zenith: θ and azimuth: Ψ). The PDF uses a muon track without stochastic losses as hypothesis. The impact of these losses, PMT response and scattering on the arrival time distribution are visualized in Fig. 5.3. Only the time information of the charge associated with the first photon that hit the OM is considered. If only the information for a single photon hit is
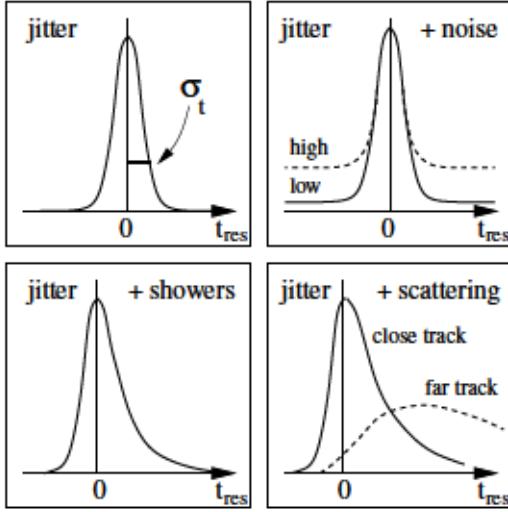
Figure 5.3: Distribution of detection arrival times in an OM from Cerenkov light emitted by a muon. Top left: Arrival time taking into account the PMT jitter. Top right: With added random noise. Bottom left: Effect of considering light yield by stochastic energy losses along the muon track. Bottom right: Impact of scattering on the arrival time distribution for a near and a far track. Taken from [168]

used, this PDF will be called a Single Photoelectron PDF, short SPE[1]. This approach ignores available information from later hits in an OM. However, it provides a fast and good reconstruction that can be used to seed more sophisticated track hypotheses. It can be improved by considering the information that N hit(s) followed in the Likelihood for the first hit. This is taken into account by the Multiple Photoelectron PDF, MPE in short.

To account for random hits (noise) detected in optical modules a small noise term is added to the likelihood. The ice properties, discussed in section 3.3.3, have to be taken into account as well. Two approaches can be used for this. If computational speed is required an analytical description of the expected light yield will be used [170]. This can be improved by simulating the light propagation in the ice and saving the information in tables. However, these tables occupy about 20 GB [107] which makes their usage very demanding in terms of computational resources.

A solution for this problem is the fit of polynomial functions to the ice properties. The functions used are described in [171]. More detail on the fitting procedure can be found in [107]. The usage of this polynomial functions, called splines, reduces the required memory storage to about 200 MB [107]. It has been shown in [107] that for the data selection discussed in that work the usage of splines improves the median angular resolution for a 10 TeV muon track from about 1° with the analytical light yield

---

[1]In IceCube "slang" SPE_{first}.

Table 5.1.: Angular reconstructions used for **STeVE**

Reconstruction	seed	method
analytical reco.	none	analytical minimization
SPE LLH reco.	analytical reco.	LLH with SPE PDF
MPE LLH reco.	SPE LLH reco.	LLH with MPE PDF
MPE LLH reco. (spline)	MPE LLH reco.	LLH with MPE PDF (spline)

description to about 0.7° (both times the MPE PDF is used).

Starting with a first guess particle track the minimizer searches for the optimal directional reconstruction. In this analysis first an analytic reconstruction is applied and used as first guess estimator for the likelihood-based reconstruction using the analytical description of the light yield and a SPE PDF. For this method the reconstruction is applied twice, with different starting parameters, to reduce the risk of falling in a local minimum. The result of this reconstruction is then used for a likelihood minimization using an MPE PDF and the analytical light yield description. The latter in turn is used as a seed for a MPE PDF using splines. This chain of reconstructions is summarized in Table 5.1.

The median angular resolution of these reconstructions for the final selection level (that also is used in the point-like source search for STeVE and selects only well reconstructed events) for IC86-I is shown in Fig. 5.4. Larger values of the likelihood, or equivalent
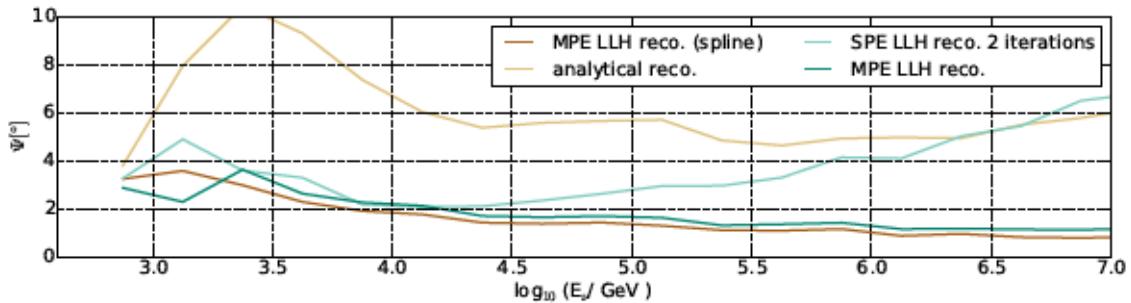
Figure 5.4: Median angular error Ψ for the different reconstructions used in this analysis. The distribution is shown for the final level selection, see section 5.3.3. The behaviour below ~ 3 TeV is likely caused by a lack of Monte Carlo statistics due to few events passing the event selection and possibly a change in the event topology.

the smaller -log($\mathcal{L}$) usually correspond to a closer fit to the true direction. However, the absolute value of this quantity depends on the number of data points taken into account. To compare the fit quality between different hypotheses the "reduced" logarithm of the

likelihood, short $\mathrm{rlogl} = \frac{-\log_{10}(\mathcal{L})}{N_{\mathrm{d.o.f.}}}$ can be used, with $N_{\mathrm{d.o.f.}}$ (the number of degrees of freedom), the number of pulses measured on optical modules, reduced by the number of parameters for the fit. Hence, rlogl can be used as a track quality parameter[2].

Angular error uncertainty

In a search for point-like sources it is not only the directional information of an event that is important but also the uncertainty on it. Here, a method is used minimizing the log likelihood at directions surrounding the best fit direction. A parabola is fitted to these LLH values. The parameters of this parabola can be used to estimate the angular uncertainty [172].

In several analysis [107, 173] it has been observed that the estimator underestimates the directional error. This effect is energy-dependent. One explanation for this behaviour is discussed in [174]. It can be shown that the stochastic energy losses, which are not part of the Likelihood description used to reconstruct muon tracks, lead to the underestimation of the directional error. This can also explain why the effect is energy-dependent with an increasing underestimation for higher energies, where stochastic energy losses dominate the total energy loss.

Both angular reconstruction and estimation of the angular error uncertainty can be verified with the non-observation of atmospheric muons from the direction of the moon [175]. The moon shields Earth against cosmic rays. In consequence no muons are produced and their absence can be fitted. With the size of the moon been well known only the angular resolution is a free parameter. The fitted angular error is in agreement with the error observed from reconstructed Monte Carlo events (after correcting for the energy-dependent overestimation). Any systematic uncertainty present in the Monte Carlo must have an impact of $0.2°$ or less [175]. Therefore, Monte Carlo events can be used to test the directional error estimator.

5.2.3. Length reconstruction

The angular reconstruction and the first guess energy estimator both assume an infinite muon track. To reconstruct the starting vertex and the stopping vertex this assumption has to be changed. The algorithm used here is discussed in more detail in [176]. In a first step, all optical modules in a radius of 200 m around the track are selected. Of these modules, for all that detected charge it is assumed that the photons arrive from the track in the Cerenkov angle without scattering in the ice. The earliest and latest point on the infinite track from which these theoretical photons could have arrived are then used as first guess for the start vertex and the stop vertex, as shown in Fig. 5.5. In a second step, the optical modules upstream of the cone shaped by the first optical module to detect charge

---

[2]It is not mathematically motivated, but a variable that has shown to be correlated with reconstruction quality in previous analyses.
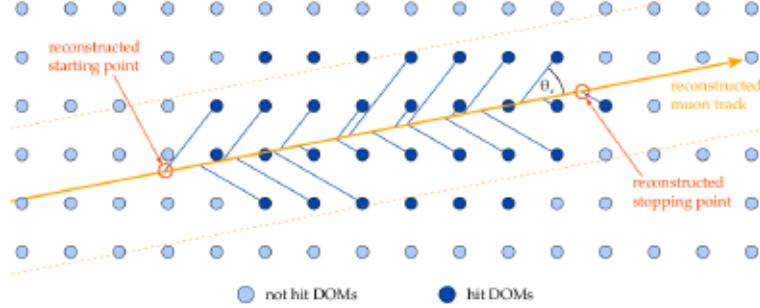
Figure 5.5: First step of length reconstruction;: The starting and stop point of a track are estimated. Taken from [176]

the Cerenkov angle and the muon track as rotational axis are selected, see Fig. 5.6. Two hypotheses are compared. The first hypothesis is a muon track without a detected charge (no-hit) while the second hypothesis is no track and no detected charge. Maximizing the ratio of the no-hit Likelihoods of these hypotheses returns an improved estimator for the starting vertex. The same procedure repeated downstream gives the stopping vertex.
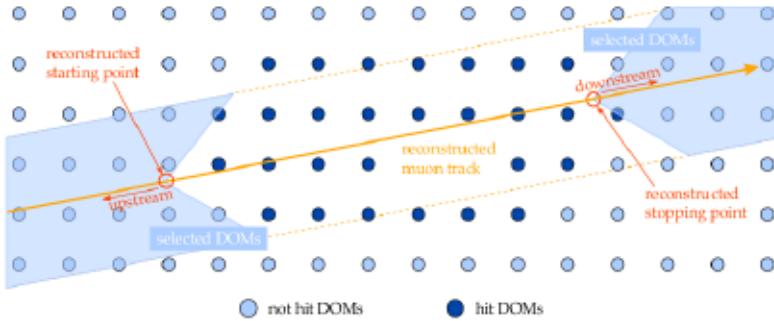
Figure 5.6: Second step of length reconstruction: Two hypotheses are compared (no track and no light detected versus a track and no light detected using a Likelihood ratio test. Taken from [176]

5.2.4. First guess energy reconstruction

This section is a summary from an IceCube paper [126]. The energy of an event is reconstructed by comparing the light yield of a hypothetical energy deposition E with the measured number of photons k, which are expected to follow a Poisson distribution. A template, Λ, is used to model the detector and ice properties. The mean number of expected photons $\lambda = E\Lambda$ for an optical module can then be compared with k using a

LLH approach,

$$\mathcal{L} = \frac{(E\Lambda)^k}{k!} \cdot e^{-E\Lambda},$$ (5.2)

$$\ln(\mathcal{L}) = k\ln(E\Lambda) - E\Lambda - \ln(k!).$$ (5.3)

Equation 5.3 can be generalized to allow for an additional noise term ρ:

$$\ln(\mathcal{L}) = k\ln(E\Lambda + \rho) - (E\Lambda + \rho) - \ln(k!).$$ (5.4)

As for the angular LLH reconstruction the detector is evaluated by building the product of all the single OM LLH expressions. Maximizing this Likelihood and adding the contributions from all optical modules provides the best fit energy estimator. The quality of this estimator is directly connected to the quality of Λ. Due to the non-trivial ice properties, in term of wavelength depending scattering and absorptions as well as inhomogeneities, a precise analytical description of Λ is not feasible. As a first guess approximation an infinite muon track with even emission of photons at the Cerenkov angle is assumed for Λ. The ice properties are modelled by an analytical formula.

This reconstruction method is used in IC86-I. For IC86-II+ an improved version is used, adding a probability density function that is convolved on the mean light yield λ, allowing for larger fluctuations, like a large Bremsstrahlung's loss along the track. It is shown in [107] that this improves the overall energy estimation. However, the underlying assumption of an even emission along an infinite muon track does not represent the reality of a TeV track starting inside the detector very well.

5.2.5. Topology and energy reconstruction

In section 5.2.4 the template Λ is an infinite muon track. This can be improved by changing the template to a series of cascade-like energy losses along a track. The sum of them is fitted to match the observed photons. Technically, this is realized by placing 1 GeV simulated cascades along the track, in this analysis with a spacing of 15 m. The light yield of a cascade scales linear with energy [129] and the shape of the emission remains the same – this assumptions holds up to PeV cascade energies [177] where the Landau-Pomeranchuk-Migdal effect [178–180] suppresses energy losses of secondary particles in the cascade over Bremsstrahlung and pair-production. This is well above the expected energy losses along a muon track from a TeV neutrino. The light yield for each 1 GeV in each optical module is then stored in a matrix Λ. All simulated cascades $\vec{E}$ can be scaled up and down. The sum of all light emissions has to match the observed light yield in each optical module $\vec{N}$:

$$\Lambda\vec{E} = \vec{N}.$$ (5.5)

Equation 5.5 can be solved with a non-negative least square algorithm. Using this method cascades can be fitted with zero energy, but non-physical negative energies are

not allowed. The sum of all the calculated energy losses along the track can be used to estimate the energy deposited by the track. The location of the first and last cascade not fitted to zero can be used as an estimator for the start and stop vertex of the track, also providing a length estimator. Additionally, estimators for the energy at the start, the maximal energy loss along the track and its position can be used by picking the according cascade along the track.

The algorithm can be extended to be used for angular reconstruction. However, for each hypothesis tested the positions of the simulated cascades along the track vary and have to be repeated. This makes this reconstruction computational expensive. In addition, an angular error estimator further increases the number of iterations required. Therefore, it is not used as angular reconstruction for this event selection.

5.2.6. Excluding coincident events

Due to the length of the trigger window (readout continues as long as the trigger condition was fulfilled in the last 5 µs), multiple event can be recorded in a single readout. These events are labeled "coincident". The most common case are two atmospheric muons, but the same probability also applies for neutrino events. Simulations show that about every tenth event triggered in IceCube is a coincident event. These coincident events can be problematic in general and for a search using starting events in particular. All the reconstructions described above use one muon track as hypothesis. If there is more than one track, this hypothesis will be wrong and may result in bad reconstruction performance. Two atmospheric muons arriving in the "right" order can lead to a reconstruction as an up-going track, a signature that would only be expected from a neutrino induced track, if the track reconstruction were true.

For starting event searches another problem can arise. If the first event is low energetic enough to pass veto conditions, as discussed in section 4.4.3, another more energetic muon can enter the detector without being vetoed. This muon, however, would be of higher energy - another discriminator variable used to split astrophysical neutrinos and atmospheric muons.

An algorithm using time and space information of the first pulse detected in the OMs is used to detect coincident events [181]. If the algorithm indicates coincidence, the event will be discarded. For the final level event selection (see below) of a simulation dataset both the ratio of coincident events and the performance of the algorithm are shown in Fig. 5.7. A part of the coincident events is badly reconstructed and does not pass the selection criteria. Out of the events passing about half of the coincident events are identified correctly. The overall "contamination" of coincident events on final level in signal simulation is 3.5 %.
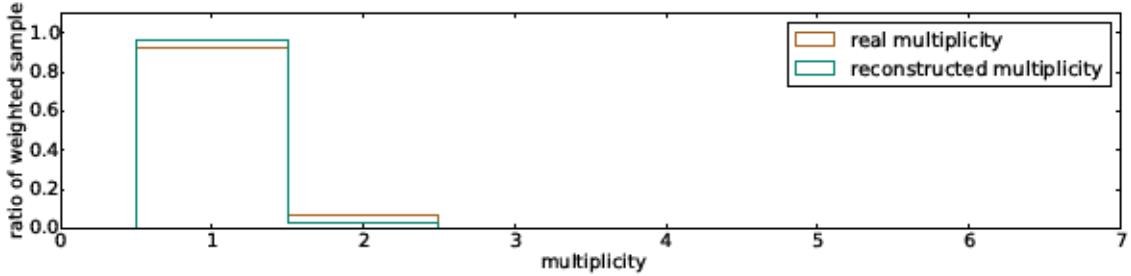
Figure 5.7: Multiplicity (number of coincident events) for the final level selection of STeVE.

5.3. Event selection

The event selection used in the point-like source search is the result of several steps of selection, here called levels. The first level, L1, is the triggering of events described in section 3.3.4. On the following levels the number of background events is reduced and the passing events are reconstructed with more sophisticated, but also more expensive algorithms computational-wise. At the same time the selection is optimized to keep signal events using signal simulations.

5.3.1. Level 2

The detector triggers events with a rate of about 2800 per second. The goal of the Level 2 procesing is to preselect potential starting muon tracks out of this large number (almost 100 billion events a year). The first selection, called a filter, is applied at the South Pole after events are triggered. This generates two limitations: Computational power (not all events can be reconstructed with sophisticated methods "on-the-fly") and transmission bandwidth to the North (not all events can be sent to the North via satellite). Several filters are applied on the triggered data. For the purpose of selecting starting events a specific filter ("Full-sky starting" filter / FSS) has been developed for an analysis optimized to search for events with energies below a few TeV (LESE) [166] (see section 4.4.3). The selection is optimized for starting tracks and and can also be used here. One difference to the selection criteria of the HESE and MESE searches is the lack of a charge cut in this filter rendering it suitable for starting events of all energies.

The FSS filter operates in two steps. In the first step, the information of pulses fulfilling the "local coincidence" condition (LC, see section 3.3.4) is used. The position of the first of these pulses in time is used to discard events that are entering the detector by demanding that this pulse is not detected on the outer layer of strings (see Fig. 5.8). Additionally, none of the five top-most optical modules in regular, non DeepCore, strings is allowed to have detected charge in LC. This requirement rejects down-going atmospheric muons, but can also reject up-going neutrino events. Rejecting neutrino

events that appear to come from the northern sky is acceptable, as the focus of this analysis lies on the southern sky - as such, only down-going events are of interest.
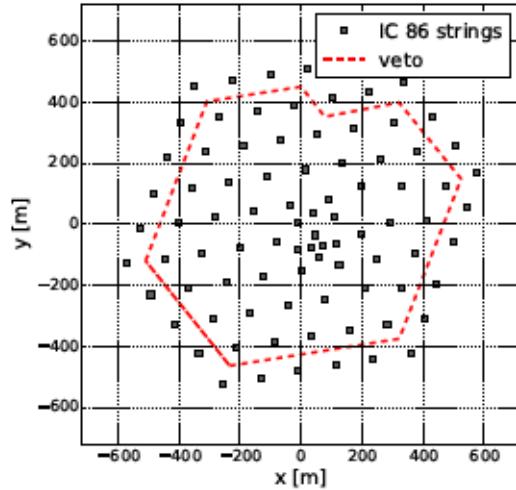

Figure 5.8: Veto region of outer layer strings that is used in both steps of the FSS filter.

In the second step, the length reconstruction described in section 5.2.3 is used to reconstruct the starting vertex of the event. If the starting vertex is reconstructed outside of the detector or in the veto region, then the event will be rejected.

About 190 events per second pass the selection described so far. These events are reconstructed using the SPE LLH angular reconstruction with two iterations described in section 5.2.2 and the energy reconstruction described in section 5.2.4. More sophisticated reconstructions are not feasible at this level due to their computational cost.

5.3.2. Level 3

To further reduce the number of background events the energy and topology of the events is used to discriminate background from data. As discussed in section 2.2.1 the spectrum of atmospheric muons is very steep ($\gamma \sim 3.7$) compared to an astrophysical signal ($\gamma \sim 2.0$). Thus, rejecting these low-energy events provides a selection that loses almost no neutrino events with energies larger than $10\,\text{TeV}$ compared to the previous selection level (see Fig. 5.9).

Due to the fact that the energy estimator changed between IC86-I and IC86-II+ two different event selections are used. Both selections use the estimated energy, the maximal distance between each pair of OMs with pulses that fulfil the LC condition and the information whether the second outer layer of strings was hit. Additionally, in IC86-I
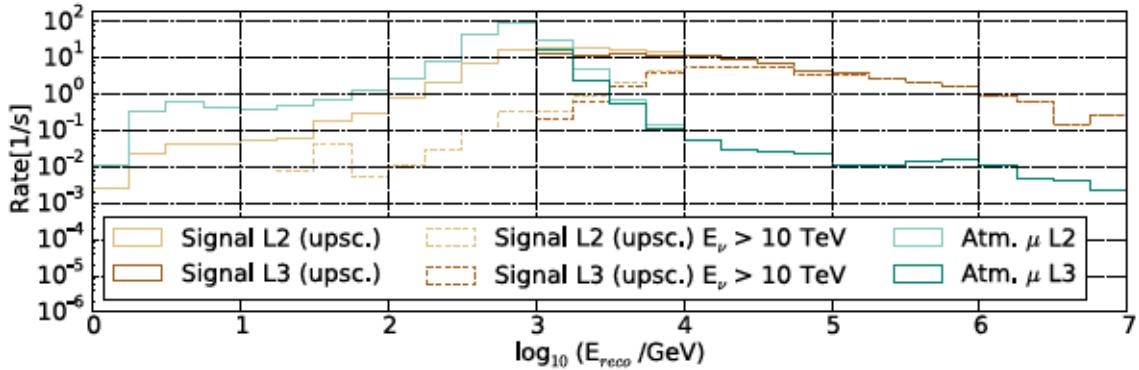
Figure 5.9: Impact of the Level 3 cut for the IC86-II+ selection: Compared are simulated atmospheric muon events (green curves) and simulated down-going and starting neutrino events (brown curves). The majority of background events (light green curve) is reconstructed with low energies. The contribution of neutrino events above $10\,\mathrm{TeV}$ is indicated by the dashed lines. The signal simulation is upscaled to the rate of the atmospheric muon simulation.

the summed up charge of the OMs on the string which carries the first OM reporting a pulse in LC is used. The charge and distance conditions are implemented to reject events in which the energy estimator is misled by a large charge deposition in a single OM very near to the reconstructed track. The additional layer two condition allows for events starting deeper inside the detector, thus less likely to be an atmospheric muon, to have a lower reconstructed energy. A visualization of these variables and the pass condition can be found in Fig. 5.10. For IC86-I one of the following two conditions has to be full filled
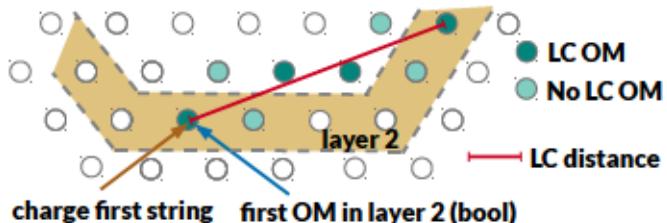
**Figure 5.10:** Level 3 variables. The grey dashed lines indicate the first outer two layers.

for an event to pass the level three selection:

- $\log_{10}(E_{\mathrm{reco\,11}} / \mathrm{GeV}) > 4$ and :

  - first OM **not** in layer 2 or :

  - $\log_{10}(Q_{\mathrm{firstLCstring}} / \mathrm{PE}) > 1.5$

- $\log_{10}(E_{\mathrm{11reco}} / \mathrm{GeV}) > 3.5$ and LC distance $> 150\,\mathrm{m}$ and :

- first OM **not** in layer 2 or :

- $\log_{10}$ ($Q_{firstLCstring}$ / PE) > 1.5

For IC86-II+ this is changed due to the changed energy estimator and one of the following three conditions has to be true:

- $\log_{10}$ ($E_{reco\,12}$ / GeV) > 4

- $\log_{10}$ ($E_{reco\,12}$ / GeV) > 3.5 and LC distance > 150 m

- $\log_{10}$ ($E_{reco\,12}$ / GeV) > 3 and first OM **not** in layer 2

5.3.3. Further reconstruction and final event selection

Since the number of background events was descreased by the Level 3 selection described in the previous section, more sophisticated reconstructions can be used. At this stage, the MPE likelihood with splines (splineMPE, discussed in section 5.2) is used for angular reconstruction. Topology and energy are reconstructed applying the algorithm described in section 5.2.5 using the reconstructed splineMPE track hypothesis.

These reconstructions provide variables that follow different distributions for well reconstructed and badly reconstructed events, or for signal-like and background-like events. Twenty and nineteen of the variables available were included in the selection of IC86-I and IC86-II+ respectively. These variables are described in Table 5.2. One variable was excluded from the IC86-II+ selection due to unsatisfying data to atmospheric muon Monte Carlo simulation agreement.

The correlation coefficients between the variables are shown both for signal, see Fig. 5.11, and background, see Fig. 5.12. The same plots for the IC86-I selection can be found in appendix A. There is correlation - for example between energy variables - as well as anti-correlations for example between *angle diff* and the length variables. *angle diff* is the angle between first-guess and final angular reconstruction. A large value can be caused by short tracks that are poorly reconstructed by the first guess estimator.

As the variables used in this selection are not independent of each other, the use of multivariate methods is suitable. For this analysis Boosted Decision Trees (BDT) are used. This method has been used in other IceCube analyses before [182].

Here, the PyBDT [183] tool is used. BDTs were chosen because of their good "out of the box" performance and the general simplicity of the method, which makes them both easy to use and to understand [184]. The principal idea behind a decision tree is sketched in Fig. 5.13. A training sample of signal and background events is created. One variable is then used to split the sample (root node in Fig. 5.13) with a one-dimensional cut.
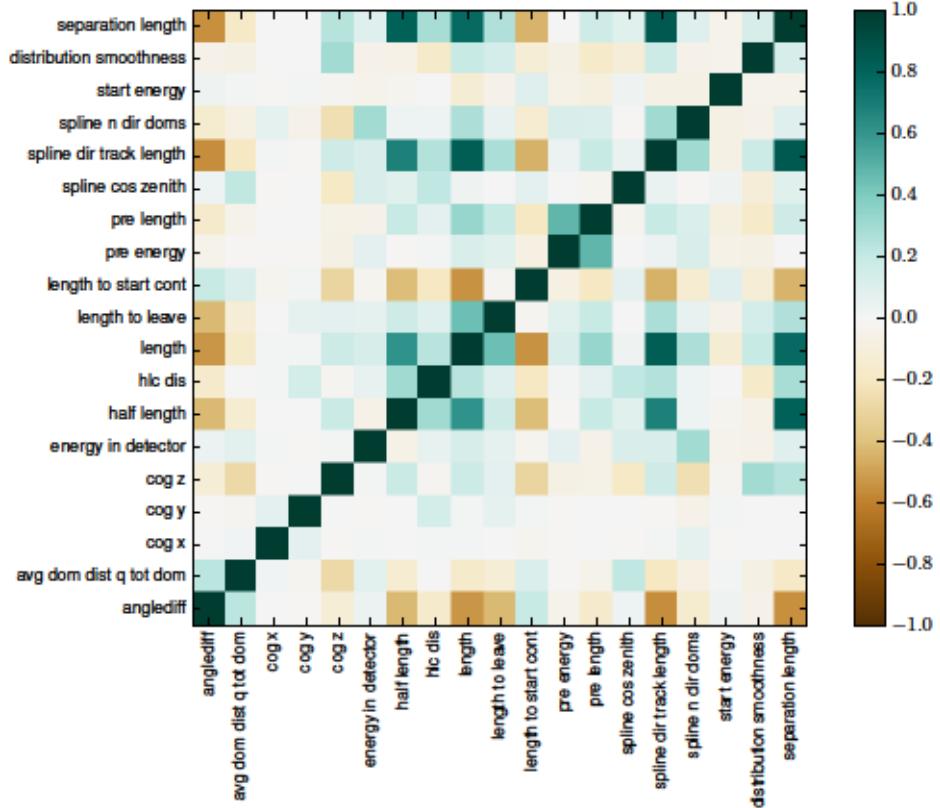
Figure 5.11: BDT variables correlation Matrix (Signal for the IC86-II+ selection.

For both background and signal a histogram for this variable is created and for each bin boundary the signal background separation is evaluated to determine the maximal separation in this variable. Here, the Gini criterion [185] is used which is defined as $g = p \cdot (1 - p)$ with p being the signal purity. Signal purity is defined as $\frac{w_s}{w_s + w_b}$ with w_s and w_b as sum over signal and background weights of the sample normed to one – the sum of both defines W. The maximal separation gain for the split of the sample in a left and a right sub-sample $\Delta S = W \cdot g(p) - W_L \cdot g(p_L) - W_R \cdot g(p_R)$ is chosen.

All events are separated in the chosen variable according to this cut value and two sub samples (nodes) are created. It is checked, whether this node fulfills an exit condition. In this case this so-called leaf node is classified as signal- or background-like, depending on a purity criterion p. The exit condition will be satisfied if the maximal number of iteration steps (depth of the tree, here three) is reached, if a node has less than a predefined number of events (here 20) or if it is a pure signal or background node.

If only leaf nodes remain, each of them will be classified either as a signal- or background-like node. This decision tree can then be used to classify events. For itself
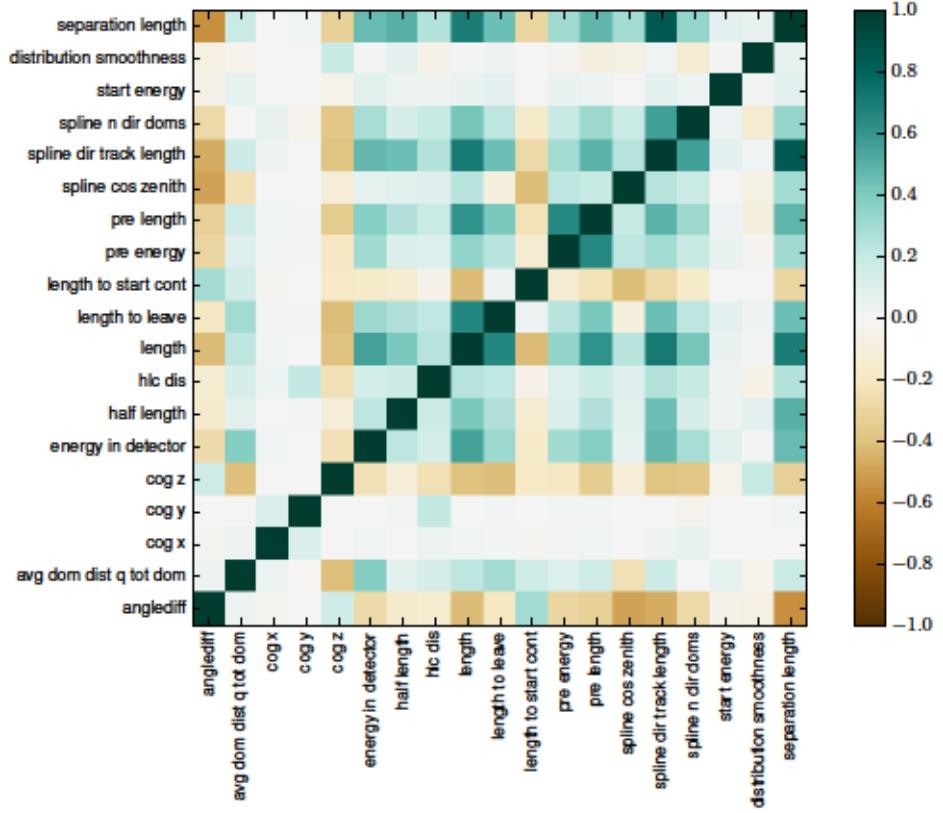
Figure 5.12: BDT variables correlation Matrix (Background) for the IC86-II+ selection.
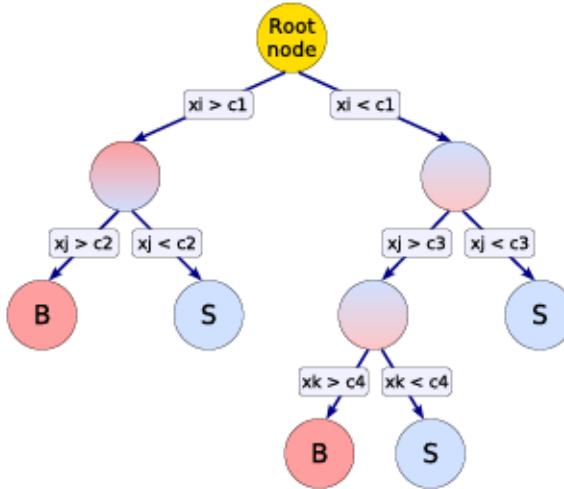

Figure 5.13: Sketch of a BDT: At each node the sample is separated in two with respect to the maximal separation gain Taken from [184].

such a decision tree is not a very efficient selection tool. However, adaptive boosting can improve the performance. In this method miss-classified events are given a larger weight and the decision tree is built again. This is repeated over and over (in this analysis 400 times) with the result of all trees ultimately being combined in a single classifier.

Additionally, the trees can be "pruned" to simplify the selection and avoid over-training. Over-training will happen if a classifier performs well on the specific events used for training, but fails to classify correctly other data because it used statistical fluctuations in the training sample for separation. Pruning eliminates leaf nodes that provide no or only small separation power. These leaf nodes are then destroyed and their parent node is classified as signal or background leaf node. Here, two pruning operations are applied. First, every node that has two leafs with the same classification is pruned as it does not add separation power. Then, for every node its separation gain is calculated. In the setting used in this analysis the nodes with the 30 % smallest gains are then pruned. The classifier returns a value between -1 to 1, with larger values being more signal-like.

In this event selection signal events are taken from Monte Carlo simulations, as described in section 3.4. For background events real data is used. The signal simulation is weighted to an E^{-2} spectrum and normed to one; the sum of all data events is also normed to one. While experimental data at this selection level most likely contains some astrophysical neutrino events, it is dominated by atmospheric muons.

In an analysis using starting events of all flavors to measure the diffuse neutrino flux [186] from both atmospheric and astrophysical neutrinos, 388 events in 641 d were detected, with about 90 of them expected to be of astrophysical origin. This can be compared to about a billion events after Level 3 cuts in this analysis. Hence, it is not expected for these events to have a major impact on any background distribution drawn from experimental data at this level. The use of experimental data makes the analysis also more robust against the influence of unknown systematic effects as they can only affect simulated signal events but do not affect the background events. While this creates independence from the quality of the atmospheric simulation, systematic uncertainties still play a crucial role for the the interpretation of the results – which depends on the simulated neutrinos.

For this analysis the focus lies on well reconstructed and down-going tracks from CC muon-neutrino interactions that start inside the detector boundaries. Hence, non-starting neutrino events or those who interact over a neutral-current or are are excluded from the training selection.

Additionally, both neutrinos at energies above 100 TeV and neutrinos from the Northern sky can lead to events that are easy to select by the BDT due to the small

number of background events for this energy and zenith range. However, these are already part of other dedicated IceCube searches for point-like neutrino emission and do not reflect the expected spectrum and position in the sky from galactic point-like sources, which are the focus of this work.

Hence, simulated signal events that are up-going are excluded as well as events with a true neutrino energy $\log_{10}(E_\nu/\text{GeV}) > 4.5$ in IC86-I. In IC86-II+ ,this condition was somewhat softened to exclude neutrinos with $\log_{10}(E_\nu/\text{GeV}) > 5$. As a last signal pre-selection criterion neutrinos with energies $\log_{10}(E_\nu/\text{GeV}) < 3$ are excluded from training selection to avoid badly reconstructed low energy signal events influencing the training. This pre-selection results in a substantial change of the signal sample, as can be seen for one of the training variables, the reconstructed zenith, in Fig. 5.14.
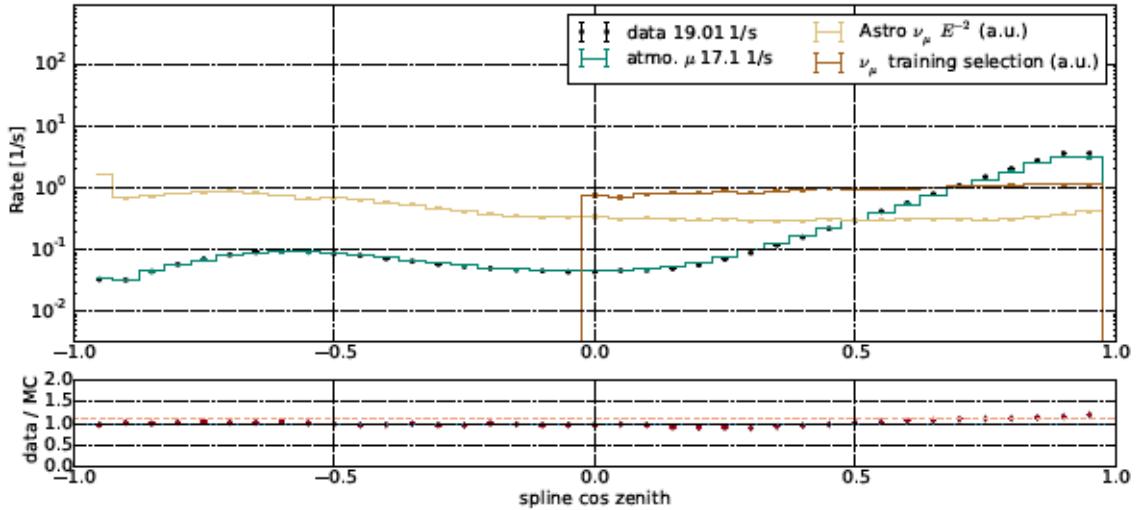

Figure 5.14: Cos(zenith) variable both for IC86-II+. Below the plots the ratio between data and atmospheric muon Monte Carlo is shown. The overall ratio between data and atmospheric muon Monte Carlo is indicated by the light red dashed line.

The variables used for BDT training are presented in appendix B and appendix C and are summarized in table 5.2. In 2012, the "lf speed" variable was excluded from training due to bad data / MC agreement. As can be seen in table 5.2, this variable had the smallest separation power of that training. The overall classification is not negatively influenced by its exclusion for IC86-II+.

Table 5.2.: Variables used in BDT training. The rank is calculated by counting how often it is used in the final trees (after pruning) and ordering the variables from often used to rarely used.

Variable name and description	Rank (IC86-I)	Rank (IC86-II+)
spline dir track length Based on the track reconstruction using an MPE LLH with splines all hits compatible in time with emission from the reconstructed track along the Cerenkov angle without scattering (direct) are selected. The maximal distance along the track between these points of hypothetical emission gives the "direct track length".	8	8
anglediff Opening angle between first guess analytical reconstruction and LLH reconstruction using a MPE LLH with splines.	18	12
energy in detector Sum of the reconstructed energy losses inside the detector volume as given by the algorithm in section 5.2.5.	1	1
length to start cont Distance between veto layer and first energy loss.	4	4
spline n dir doms Number of OMs with "direct" hits.	2	3
pre energy Sum over the reconstructed energy losses prior to the maximal energy loss.	10	5
half length The detected hits are split in time in the middle of the event. For both halfs the "center of gravity" (cog), the average position in x,y,z is calculated. The distance between both calculations gives the half length.	14	9
cog x Average position (x-coordinate) over all OMs with detected charge.	9	15
cog y Average position (y-coordinate) over all OMs with detected charge.	13	17
cog z Average position (z-coordinate) over all OMs with detected charge.	15	16
hlc dis Maximal distance between two OMs with hits fulfilling the LC conditon, see also Fig. 5.10.	5	7

separation length Similar to half length but with the cog 11 10
difference between first and last quartile. Here, values can
be positive and negative, also providing separation power
between up-going and down-going events.

pre length Distance between first reconstructed energy loss 6 11
and maximal energy loss.

distribution smoothness Describes the hit pattern along 19 13
the track. It yields 0 for a track with an uniform hit pattern
and values approaching -1/1 for tracks with a majority of
hits at the beginning/end of the track.

start energy First reconstructed energy loss. 18 19

length Reconstructed length of the event. Defined by the 17 12
distance between the first and last reconstructed energy loss
along the track.

spline cos zenith Cosine of the reconstructed zenith angle 3 2
using an MPE spline LLH.

lf speed Reconstructed velocity of the track using the first 20 –
guess analytical reconstruction presented in section 5.2.2.

length to leave Distance between last reconstructed energy 16 6
loss and projected exit point of the inner detector volume.

avg dom dist q tot dom Average distance between the 7 14
OMs detecting hits and the OM with the largest detected
charge.

The result of the training is shown in Fig. 5.15. The optimal value for the final
event selection is found by optimizing the cut in terms of sensitivity. Sensitivity will be
explained in detail in section 6.1 but summarized briefly, it is a measure for the lowest
possible flux detectable with this analysis. As discussed above this analysis is targeted at
muon neutrinos with $E_\nu < 100 \, \text{TeV}$.

In Fig. 5.16 the sensitivity for this scenario and different cut values for the BDT
are shown. In addition to the cut on the BDT value events in data and signal Monte
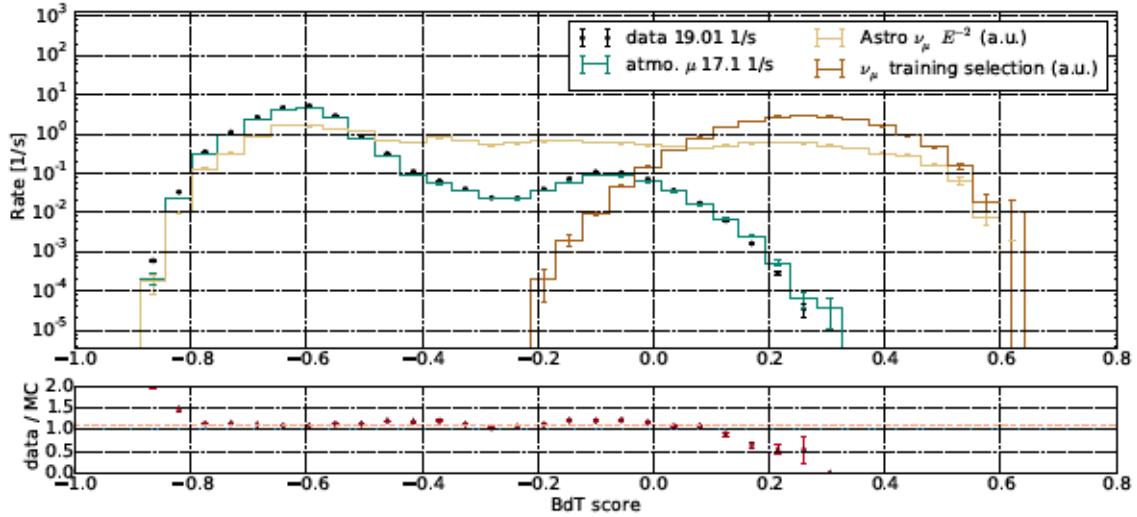
Figure 5.15: BDT score distribution for IC86-II+. Below the plot the ratio between data and atmospheric muon Monte Carlo is shown. The overall ratio between data and atmospheric muon Monte Carlo is indicated by the light red dashed line.

Carlo had to fulfil some track quality parameters, be reconstructed as down-going and have a reconstructed energy in the detector larger than $1\,\mathrm{TeV}$. This yielded a BDT cut value of 0.15 for IC86-I and 0.28 for IC86-II+.
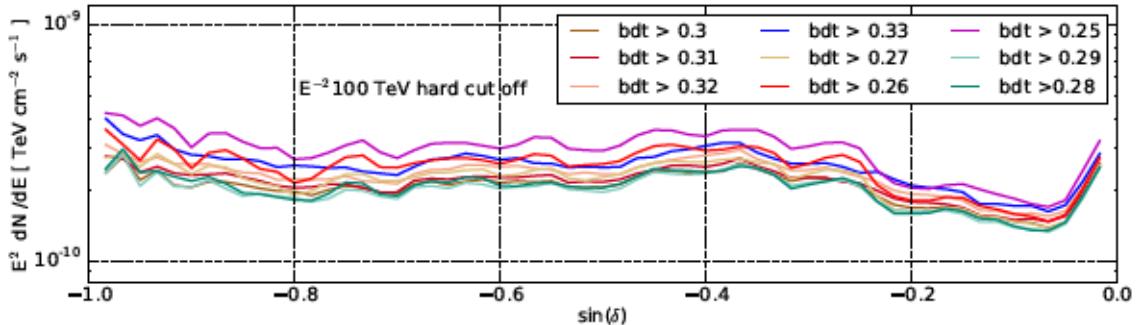

Figure 5.16: Performance in terms of sensitivity for different BDT cut values for IC86-II+.

BDT quality checks The usage of multivariate methods, like the BDT used here, comes with the risk of overtraining, as mentioned above. To estimate this risk the used sample can be split with one part used for training and the other part being used as test sample. After the BDT is trained both test and training sample events are classified. This is shown in Fig. 5.17 for IC86-II+ and in appendix A for IC86-I.
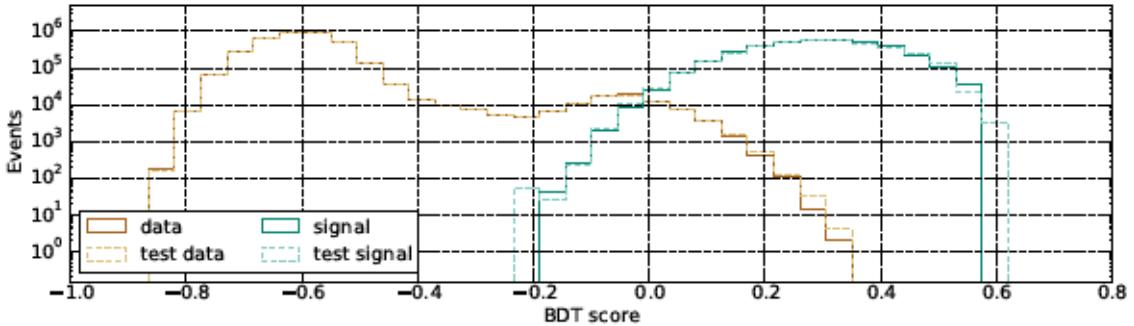
Figure 5.17: Comparison between training and test sample for signal and data for IC86-II+. The histograms for signal and test signal are scaled up to fit the number of events in data.

To compare these samples a Kolgomorov Smirnov (KS) test [187] is used. For IC86-II+ both data (background) and signal training and test signal agree reasonably well (KS $p_{data} = 0.95$ and KS $p_{signal} = 0.64$). For IC86-I (KS $p_{data} = 0.69$ and KS $p_{signal} = 0.05$) signal has a poor performance in the KS test. However, the disagreement origins mainly at low BDT scores where the relative abundance compared to the total signal distribution is small (see Fig. A.1). Hence, even if the classifier does not perform as well on test signal as on training signal it, will still provide good separation power.

Properties of the final event selection The selections used in IC86-I and IC86-II+ perform similar in terms of sensitivity. However, they also differ in a number of points like the number of events, the effective area and the angular resolution in the sample. The final sample of IC86-I (337 days livetime) contains 15043 events, whereas the following three years of IC86-II+ (1031 days livetime) yield 7005 events. In both cases the vast majority of these events are atmospheric muons. The effective area is comparable between both selections, but the IC86-I event selection provides a better median angular resolution, see Fig. 5.18.

The effective area is zenith dependent, see Fig. 5.19. Hence, the number of neutrino events expected to interact within IceCube varies. This dependence is strongest at lowest energies. At energies above 30 TeV the effective area is (almost) zenith angle independent. The effective area below 30 TeV is largest for the most vertical angles. A possible explanation would be that vertical background events are easier to reject – leading to higher BDT scores for signal events from this region in the sky on average.

The effective areas can be used to calculate the number of expected events from both atmospheric and astrophysical neutrinos (see Fig. 5.20). For the atmospheric neutrinos the model with self-veto probability discussed in section 4.3.2 and [160, 161]
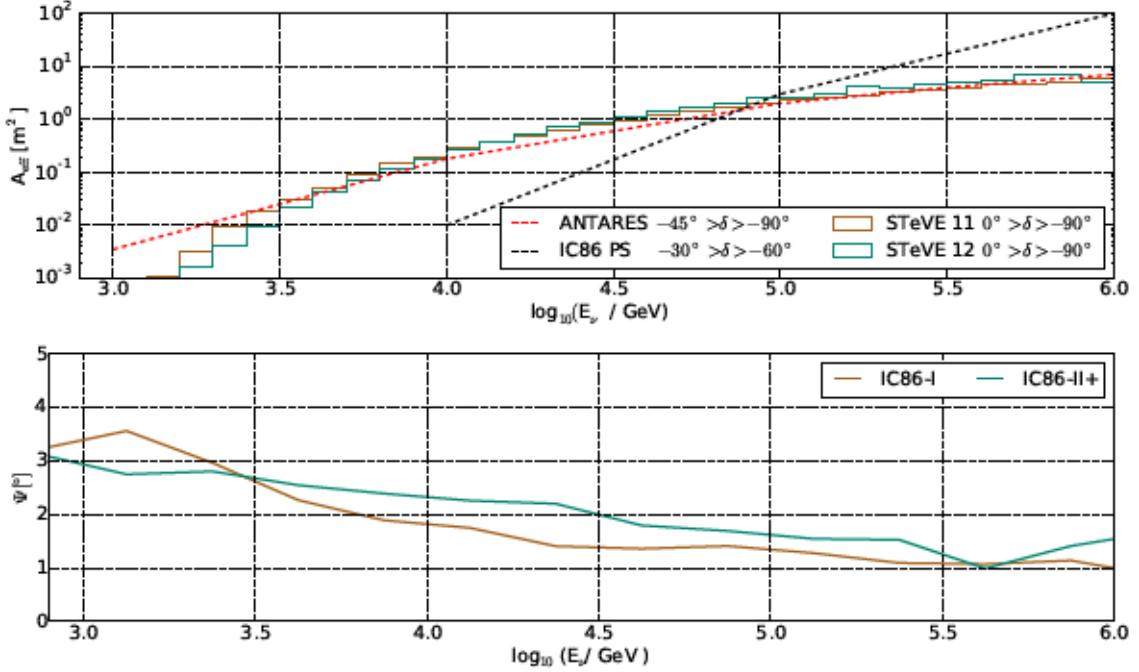
Figure 5.18: Top: Effective area for IC86-I and IC86-II+ compared to the through-going muon analyses of IceCube [149] and ANTARES [162]. Bottom: Median angular resolution for IC86-I and IC86-II+.
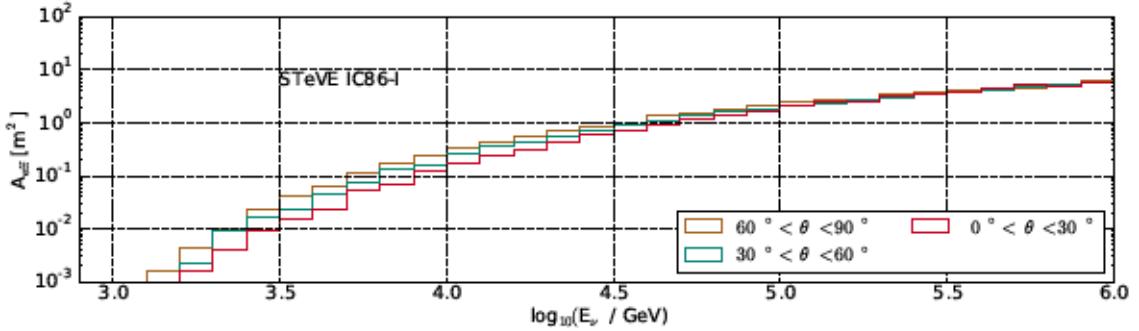

Figure 5.19: Effective area for IC86-I for three different zenith bands.

is used. For the astrophysical neutrino flux the combined best-fit from [92] is used. In both selections the number of expected neutrinos is small compared to the number of data events (which are expected to be mostly atmospheric muons). Also visible is the significant larger number of data events at lower energies in IC86-I.

As discussed in section 5.2.2, the angular error estimator has to be corrected since it overestimates the resolution at high energies. This is achieved by plotting the ratio (pull) of reconstructed direction over Monte Carlo true neutrino direction versus the
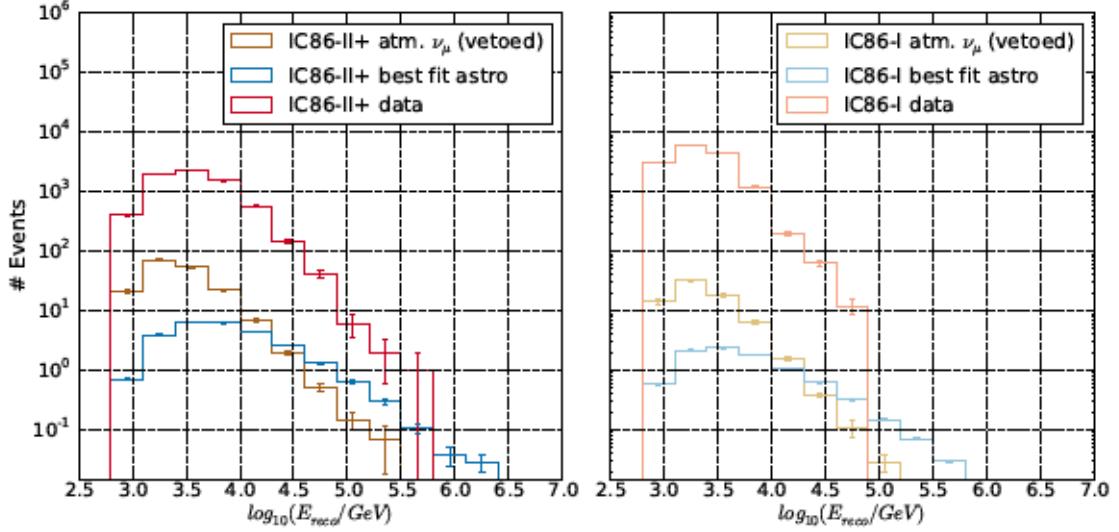
Figure 5.20: Expected number of atmospheric and astrophysical neutrinos for IC86-I and IC86-II+ selection, dependent on reconstructed energy, for the final event selection. Also shown is the distribution of the data events.

deposited total charge inside the detector Q_{tot} and parametrizing the overestimation by eye (see Fig. 5.21).
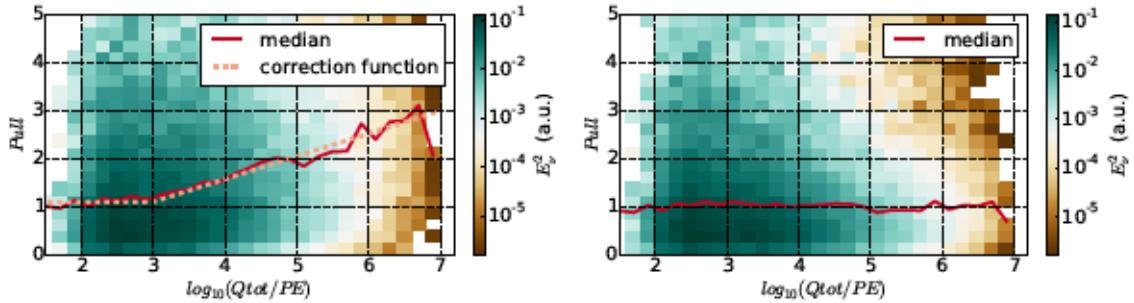

Figure 5.21: Two dimensional histogram of the difference between estimated angular error and true error between reconstruction and simulated neutrino in the dependence of logarithm of the charge deposited in the detector. Left: Pull uncorrected Right: Pull corrected.

Both for IC86-I and IC86-II+ a composite function of a steady ratio a at small charge (less than 1000 PE for IC86-I and less than 100 PE for IC86-I) and a slope $a + b \cdot \frac{\log_{10}(Q_{tot}/PE) - c}{d}$ at higher charges describes the charge dependent overestimation well and is used to correct for it (see Fig. 5.21). The parameter values used in IC86-I and IC86-II+ are shown in Table 5.3.

Table 5.3.: Parametrization parameters for angular error estimator correction

Event selection	a	b	c	d
IC86-I	1.1	1.9	3	4
IC86-II+	1.1	1.9	2	5

The energy of an event will be used as a term in the likelihood-based search for point-like neutrino emission in the following chapter. In Fig. 5.22 neutrino energy and reconstructed energy inside the detector (using the reconstruction from section 5.2.5) are compared. For both years there is a clear correlation between neutrino energy and reconstructed energy. Additionally, the effect of the different Monte Carlo used in IC86-I and IC86-II+ can be seen. For IC86-I, neutrino events are generated following an E^{-1} spectrum, providing good statistics even at the highest energies. For IC86-II+ a data set with neutrino events generated to follow an E^{-2} spectrum is used. This leads to a lack of statistics at energies above $1\,PeV$. At energies below $10\,TeV$ the neutrino energy is overestimated for a small fraction of events in IC86-II+. A probable explanation is the larger statistic for the E^{-2} dataset at these energies as a similar effect can be seen for high energy neutrinos in the IC86-I Monte Carlo that are underestimated.
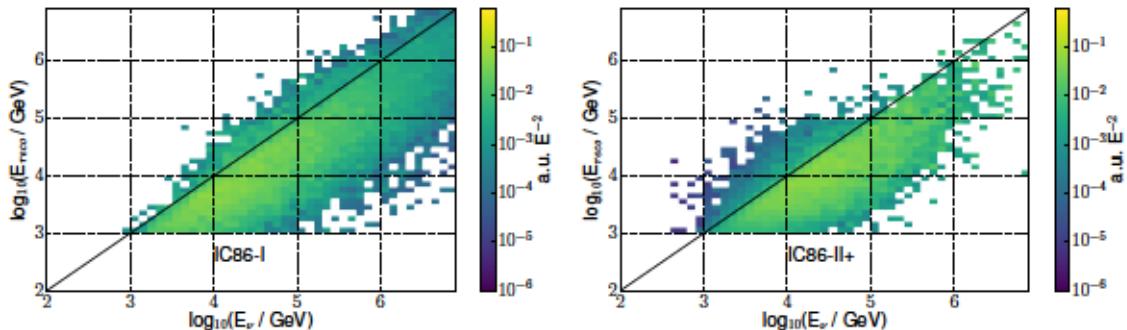

Figure 5.22: Neutrino energy versus reconstructed energy in the detector for IC86-I (left) and IC86-II+ (right) at final selection level. The energy dependent difference in statistics for both samples is visible.

5.3.4. Events in STeVE that appear in HESE, MESE or LESE

With four searches dedicated to detect starting events some overlap is to be expected. First, the overlap between **STeVE** and the HESE sample is investigated. Here the four year HESE sample [188], taken between 2010 and 2014, consisting of 54 events is used. In the period prior to May 2011 the FSS was not implemented and the **STeVE** analysis has no data. From the remaining 45 events two also appear in the **STeVE** sample. Both events (HESE event 19 and 51 in order of time) are classified as shower-like. Both

interact in the lower part of the detector and are to some degree extended.

Their reconstructed energy in the HESE analysis is $(71 \pm 7)\,\text{TeV}$ and $(66 \pm 6)\,\text{TeV}$. This can be compared to the values from the **STeVE** reconstruction giving $68\,\text{TeV}$ and $56\,\text{TeV}$. The good energy reconstruction considering the wrong track hypothesis shows the strength of the used topology and energy reconstruction. It can reconstruct the initial energy loss well - independent if it is followed up by a muon track. In terms of reconstructed direction the results of the **STeVE** reconstruction show strong deviations from the HESE results. Given the wrong event hypothesis of a track instead of a cascade this is no surprise.

The question arises why no track-like event detected in HESE between 2011 and 2013 appear in the **STeVE** sample. Of all 45 events in these three years eleven are classified as track-like and in total 22 pass the FSS filter. Of these 22 events four are classified as track-like. One of these four events is down-going. This is the only event that could pass the BDT selection. An evaluation of the BDT score for this event shows a value of 0.08 – slightly below the chosen optimal cut value of 0.15. As for the seven tracks that do not pass the FSS condition it is interesting that six of them are reconstructed as down-going. Hence, it seems challenging for down-going HESE tracks to even pass the first selection step of the LESE and **STeVE** analysis.

The MESE event sample consists of 546 Events. 167 Events were taken before the implementation of the FSS filter. Of the remaining 379 events 85 pass the FSS filter. In total 48 MESE events (23 in IC86-I and 25 in IC86-II+) pass the level three condition of **STeVE** and are scored with a value larger than zero by the corresponding BDT for IC86-I or IC86-II+. Of these events seven pass the final **STeVE** event selection (four in IC86-I and 3 in IC86-II+). The distribution of these events is visualized in Figure 5.23.
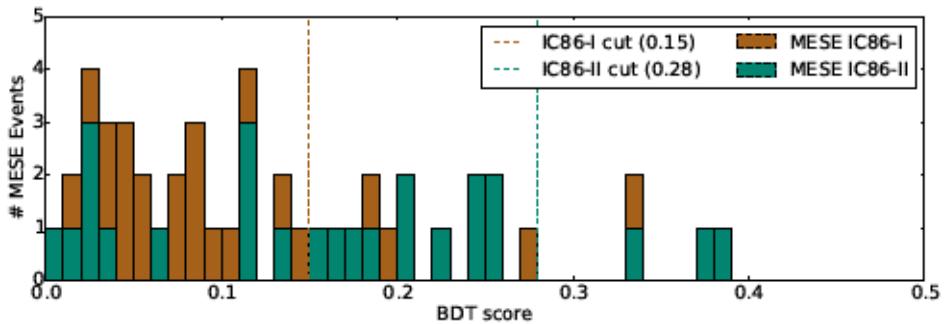

Figure 5.23: BDT scores of MESE events and selection cuts for final event selection of IC86-I and IC86-II.

The size of the overlap might differ in signal simulation. If it was comparable to

the background overlap, the samples would be almost disjoint – increasing the gain of a joint analysis.

As for the other starting event searches the overlap between LESE and **STeVE** is small. 86 events appear in both samples leading to an overlap of roughly 1 %. In total 330 events of the LESE event sample pass the Level 3 condition of **STeVE** and are scored with a value larger than zero by IC86-I BDT. The BDT score distribution of these events is shown in Fig. 5.24.
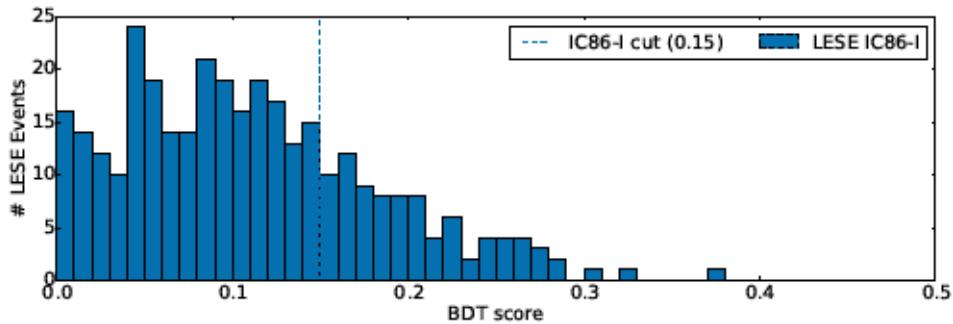

Figure 5.24: BDT scores of LESE events and selection cuts for final event selection of IC86-I.

In general these results were expected. MESE, LESE and **STeVE** are all dominated by atmospheric muons. Due to their vast number (about 100 billion detected each year) and the focus on different energy ranges it seems reasonable to argue that a large number of them show a topology similar to starting events. The searches then draw events from this vast pool, each having a different focus. This leads to the small overlap. For all three other starting samples (HESE, MESE and LESE) additional events are close to the optimal BDT score cut selected in **STeVE**. This can be seen as cross-validation of the four samples used to identify events with a starting-like topology.

5.3.5. Data quality

The IceCube detector can be operated in different modes of data taking. The most trivial mode is off. This can happen in case of maintenance to solve technical problems. The detector can be calibrated using emission of LEDs on the OMs. Due to this additional light source these periods of data taking are not used. Data taken over several hours (typical eight hours) is combined in a run. Sometimes parts of the detector stop data taking due to hardware problems. While these problems persist, the detector is operated excluding the non-working optical modules and data is saved in new runs.

These cases are potentially harmful for the analysis presented here since it depends on the outer layer of the detector being capable to detect tracks entering the detector volume.

One simple example: The detector is split in half. One half is operational while the other one is off. For the filter and the reconstruction events arriving from the off direction appear to start inside the volume, see Fig 5.25.
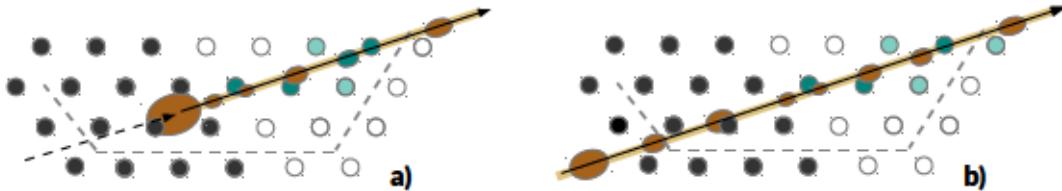

Figure 5.25: Impact of a partial detector configuration. If parts of the detector are disabled (grey OMs), it can be very challenging to distinguish atmospheric muons from starting tracks.

To avoid such a scenario and the corresponding increase in background events, all runs that are taken during periods in which 50 or more optical modules in the veto region are deactivated are excluded. As shown in Fig. 5.26 this cut eliminates the vast majority of runs with an atypical rate variation. The remaining modulation is due to the annual atmospheric changes leading to a variation in the overall muon flux.

42 OMs in the veto region are out of service permanently. While partial detector operation should only increase the number of detected events from a broad region in most of the cases, a scenario can be constructed in which only a few OMs on one veto layer string are deactivated. Muons could then arrive primarily from this direction. If a run during such a partial detector operation lasts for several hours, the rotation of the Earth should smear out this effect. However, for very short periods of partial detector configuration it might be problematic since the smearing might not occur. Since short runs are typically related to some problems during data taking, all runs that last for less than thirty minutes are excluded. While these measures avoid potential harm, the livetime of the sample after these cuts is almost identical to the total livetime (see Fig. 5.27).
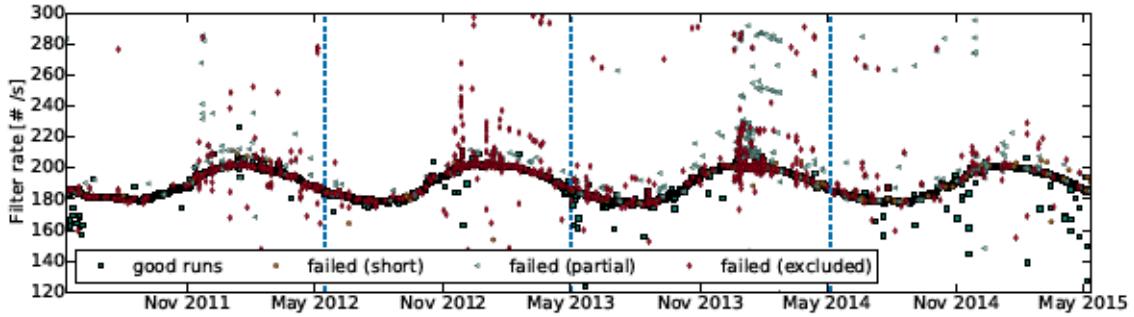
Figure 5.26: Rate of the FSS Filter. Vertical lines indicate the beginning of a new year of data-taking. Runs are classified in four categories. Runs during which the detector was calibrated or operated in a faulty state are marked as excluded. Partial runs (more than 50 OMs in veto region deactivated) are runs during which the detector was operated with a subset of OMs but otherwise worked as intended. Short runs are runs that took less than 30 minutes. Good runs are all remaining runs. The increased number of partial runs in winter months (Northern hemisphere winter, Antarctic summer from November to February) can be explained by increased maintenance and calibration of the detector in this time. The filter rate calculation shown here is not very precise for runs with very small run time - leading to outliers that are not partial. For some good runs the shown rate is unexpectedly low. This has been identified as faulty entries in the used monitoring database and not in the data.
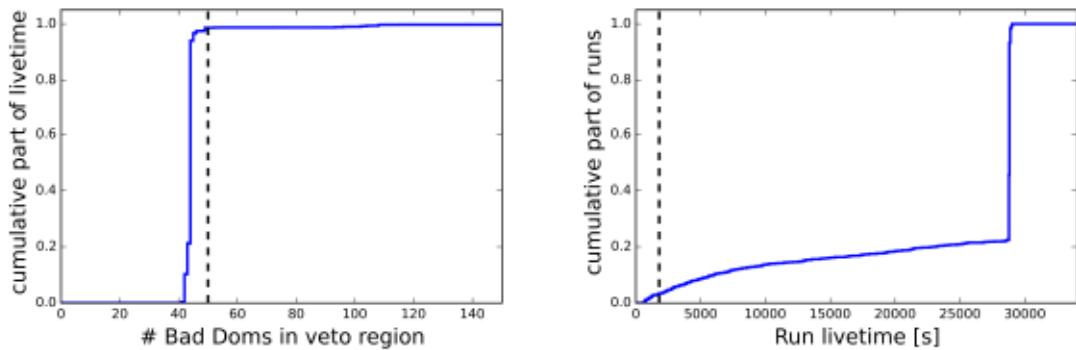

Figure 5.27: Cumulative livetime of the IC86-I selection normalized to one for both the partial (left) and short (right) run exclusion.

6. Point-like source analysis and results

This chapter discusses how to search for a neutrino point-like source in the data provided by the event selection presented in the previous chapter. First, the statistical method used, the unbinned maximum likelihood method, is explained both in general and for the IceCube-specific implementation. This is followed by a discussion on how to translate these results into an expression of probability for a point-like emission of neutrinos from a certain point in the sky. This analysis is applied both for a list of interesting objects, discussed in section 6.4, and in an unbiased search of the entire southern hemisphere, discussed in section 6.5.

6.1. The unbinned likelihood method

The simple approach to search for a point-like emission is to define a search bin around an investigated point in the sky, count the events in it and compare this number with the expected number of background events. However, it has been shown in [189] that the number of events required for a detection can be decreased by using the unbinned likelihood approach which includes energy information as described next[1]. The binned approach can be improved by calculating the probability density $\mathcal{S}_i$ to origin from the investigated source and the probability density $\mathcal{B}_i$ to be a background event for each event. Both probability densities are composed of a spacial and an energy term:

$$\mathcal{S}_i = S_i(|\vec{x_i} - \vec{x_s}|, \sigma_i)\, \mathcal{E}_i(E_i, \delta_i, \gamma_i) \tag{6.1}$$

$$\mathcal{B}_i = B_i(\delta)\, \mathcal{E}_i(E_i, \delta_i) \tag{6.2}$$

The spacial term of the signal PDF S_i used in this analysis takes into account the distance between the reconstructed position in the sky of the event $\vec{x_i}$ the position of the investigated source $\vec{x_s}$ as well as the estimated error of the angular reconstruction σ:

$$S_i(|\vec{x_i} - \vec{x_s}|, \sigma_i) = \frac{1}{2\pi\sigma_i^2} e^{-\frac{|\vec{x_i} - \vec{x_s}|^2}{2\sigma_i^2}}. \tag{6.3}$$

Due to its position at the South pole the rotational axis of the detector coordinate system and the equatorial coordinate system are aligned. Hence, the acceptance of the detector

---

[1]In the example given in [189] the required flux for a discovery will decrease by 10 % and up to about 50 % if an additional energy PDF is used.

averaged over a long data taking period like a year is independent of right ascension and only dependent on the declination δ of the source. The number of expected background events near the investigated source can be estimated by averaging over the number of events in a declination band. In this analysis 40 bands in $\sin(\delta)$ are used in the southern sky. The acceptance of the detector is dependent both on energy and declination, as shown for the effective areas discussed in section 5.3.3 and Fig. 5.19.

Thus, a two dimensional PDF is used estimating both energy and zenith for signal and background. For signal this PDF depends additionally on the assumed spectral index of the signal γ. The PDFs are generated by creating two-dimensional histograms in units of sinus of declination and $\log_{10}$ of the reconstructed energy and interpolating between the histogram values using a spline function. The PDFs for signal and background are then combined in a single PDF $f(n_s)$:

$$f_i(n_s) = \frac{n_s}{N} \mathcal{S}_i + \left(1 - \frac{n_s}{N}\right) \mathcal{B}_i. \tag{6.4}$$

Here, N is the number of events in the sample and the signal strength is expressed in n_s, a free parameter. n_s is correlated, but not equivalent to the number of signal events due to the energy dependence of $\mathcal{S}_i$ and $\mathcal{B}_i$. This energy term can lead to high energy events yielding higher n_s values than their injected number and vice-versa for low-energy events. The product of the individual PDFs of all events N multiplied defines the likelihood $\mathcal{L}$:

$$\mathcal{L}(n_s) = \prod_i^N [f_i(n_s)] \tag{6.5}$$

Two hypotheses are compared: The likelihood of the data set to consist of background-only events and thus, a "signalness" parameter $n_s = 0$ is compared with the maximized likelihood for the data set with n_s and γ as free parameters. The latter yields the optimal combination of both parameters $\hat{n}_s$ and $\hat{\gamma}$. The ratio between the null hypothesis and maximized likelihood defines the test statistic TS:

$$TS = -2\log\left(\frac{\mathcal{L}(n_s = 0)}{\mathcal{L}(\hat{n}_s, \hat{\gamma})}\right) \tag{6.6}$$

Larger values of TS are less compatible with the background-only hypothesis. If the right ascension of the data is scrambled, it will be possible to generate many skies for which any correlation between events is purely coincidental. This is done by replacing the reconstructed right ascension by a random value. By calculating the TS at the investigated point for each of these skies it can be estimated how likely it is to measure a

certain TS under the background-only hypothesis.

By injecting signal events according to a certain flux strength the sensitivity, discovery potential and upper limits for a certain point in the sky can be estimated. The sensitivity is defined as the neutrino flux from a point-like source for which in 90% of the cases the TS is larger than the median of the background-only TS distribution (see Fig. 6.1 for a visualization). The following definitions are also depicted in Fig. 6.1. The discovery potential is defined as the flux yielding a median TS with a background only probability for a TS this large or larger of $2.87 \cdot 10^{-7}$ (5σ) or less. The upper limit is defined following the classical approach by Neyman [190] as an injected flux that yields a higher TS value than the calculated one for the unscrambled sky at this point in 90% of the cases. In this analysis the likelihood calculations are provided by the skylab package[2].
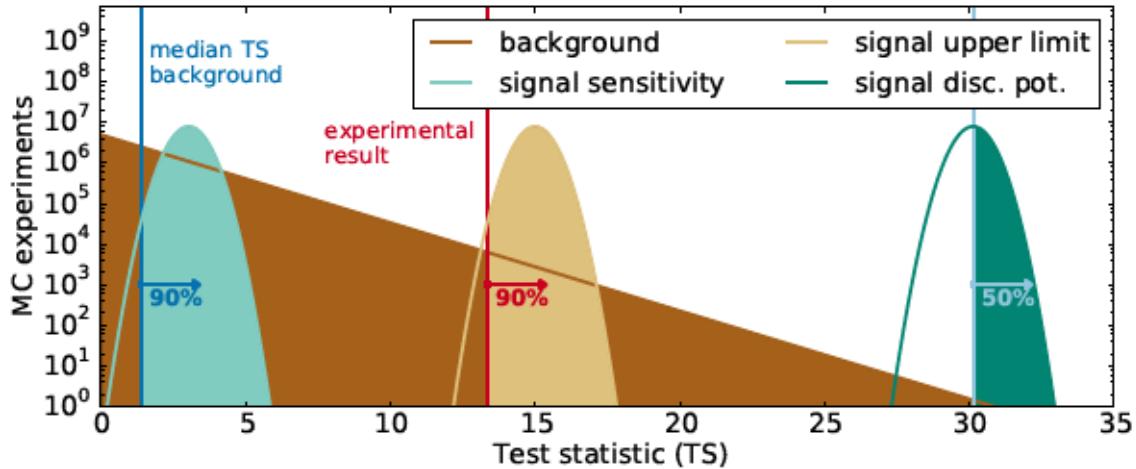

Figure 6.1: Sketch of background-only TS distribution and TS distributions for a neutrino flux from a point-like source corresponding to sensitivity flux, upper limit flux and discovery potential flux.

While it is possible to obtain sufficient statistics in TS distributions to evaluate upper limit and discovery potential, this can be computationally expensive. One solution is the description of the TS distribution by a χ^2 function [191]. Due to the restriction of $n_s \geqslant 0$ underfluctuations in the sky will yield a TS of zero. This is corrected by adding an additional parameter η, defined by the ratio of trials yielding a TS larger than 0. Hence, the TS values larger than zero can be described by $\eta \cdot \chi^2(N_{\mathrm{d.o.f}})$. As two parameters ($n_s$ and γ) are fitted, the expected $N_{\mathrm{d.o.f}}$ is two. In a random sky, underfluctuations are naively expected for fifty percent of cases ($\eta = 0.5$). If the number of trials in which n_s is fitted to 0, equalling a TS value of 0, is evaluated it is found that this value differs from 0.5 and seems to prefer lower values of η, larger percentage of under fluctuations.

One likely explanation for the observed abundance of underfluctuations is the use of the energy term in the LLH. It has been shown in more detail in [192] that the number of data events used in IceCube analyses is too small to sample the background PDF correctly. An example of such a TS distribution and a comparison of a fitted χ^2 and the expected χ^2 can be found in Fig. 6.2 for $-30°$ declination.
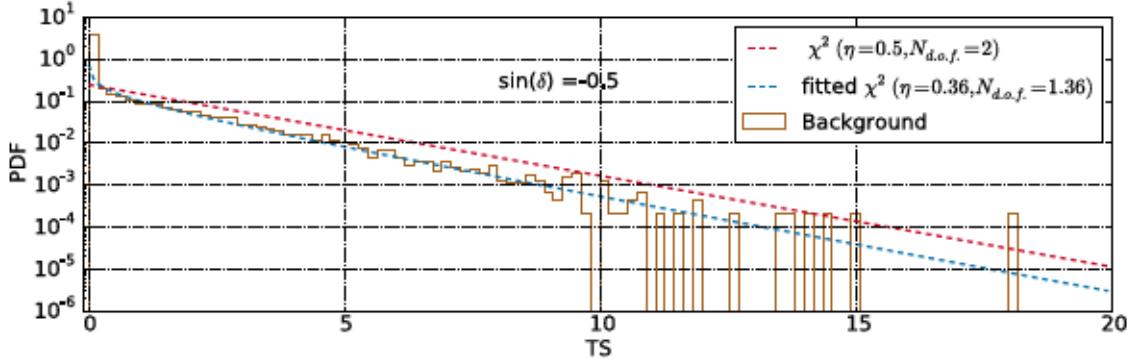

Figure 6.2: χ^2- fit to the background-only TS distribution.

Both η and $N_{d.o.f}$ are zenith-dependent, see Fig. 6.3. For this analysis spline functions are fitted to both distributions in order to estimate η and $N_{d.o.f}$ for every declination. The values of these spline are then used to convert the evaluated TS values into p-values.
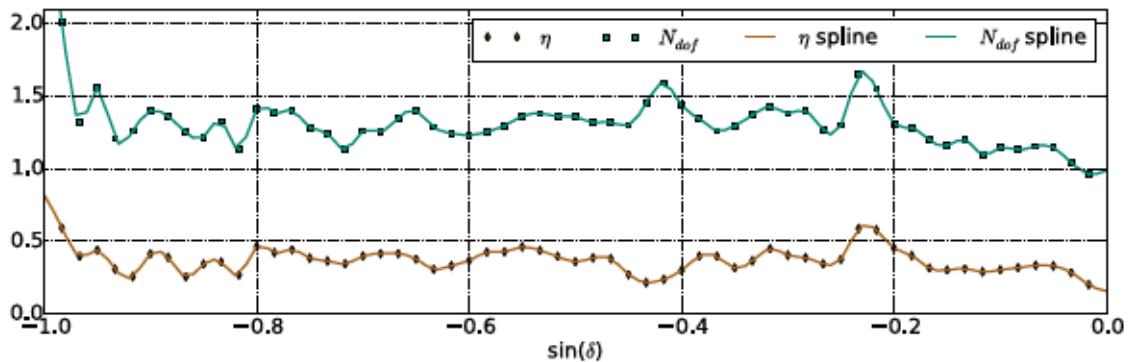

Figure 6.3: Zenith dependence of the two χ^2 parameters η and $N_{d.o.f}$

6.2. Sensitivities

The sensitivity of this analysis is shown in Fig. 6.4. Here, both the sensitivity for a point-like source with an unbroken E_ν^{-2} spectrum and for different cutoff scenarios is

shown. As expected an unbroken spectrum gives the best sensitivity. Noteworthy is also the almost zenith-independent behaviour for all, but the 10 TeV sensitivity curve. An explanation for the zenith dependence below 10 TeV can be the lower number of background events near the horizon due to the zenith-dependence of the atmospheric muon flux. As the muon spectrum is steeper than the expected neutrino spectrum, this effect is more prominent at lower energies where the energy term in the LLH function brings little gain.
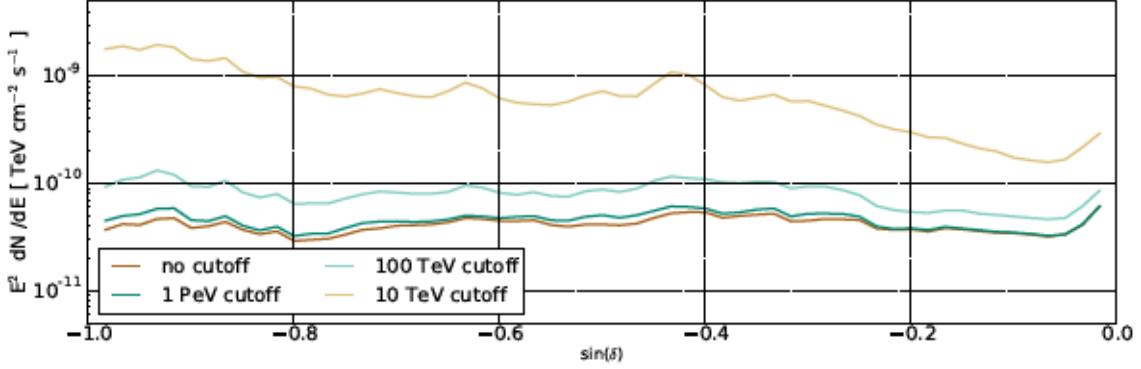

Figure 6.4: Sensitivity of the **STeVE** analysis for an E_ν^{-2} flux with different cutoffs in neutrino energy.

This analysis was optimized for neutrinos with $E_\nu < 100\,\text{TeV}$. Therefore, a cutoff is implemented excluding all neutrinos with $E_\nu > 100\,\text{TeV}$ from the likelihood calculation. In Fig. 6.5 the sensitivity of **STeVE** is compared to the sensitivity of the combined MESE and through-going search and the sensitivity of ANTARES, all discussed in section 4.4. While, **STeVE** performs better than the previous IceCube searches (about a factor two improvement for this scenario), it is outmatched by the ANTARES search by about a factor 3.5. This is not surprising taking the better angular resolution, equal or larger effective area and lower number of background events of the ANTARES search into account, which can use the Earth as shield against atmospheric muons when looking at the southern sky.

Not only the zenith-dependence but also the energy dependence of the sensitivity is of interest. In the section above, the 100 TeV cutoff scenario has been presented. To get a more detailed description of the energy dependence the differential sensitivity is calculated as well. For this an upper and lower cutoff in energy is used. In this study four bins per energy decade are used. In each bin the events are weighted to an E^{-2} spectrum. The differential sensitivity is calculated for **STeVE** and the three other IceCube searches for point-like sources discussed in section 4.4. For a better comparison the data of the through-going and LESE analysis are scaled up to the livetime of the MESE analysis (about 1000 days). Together these four analyses cover more than six decades of energies, as shown in Fig. 6.6. **STeVE** is the most sensitive analysis of these four between 10 TeV
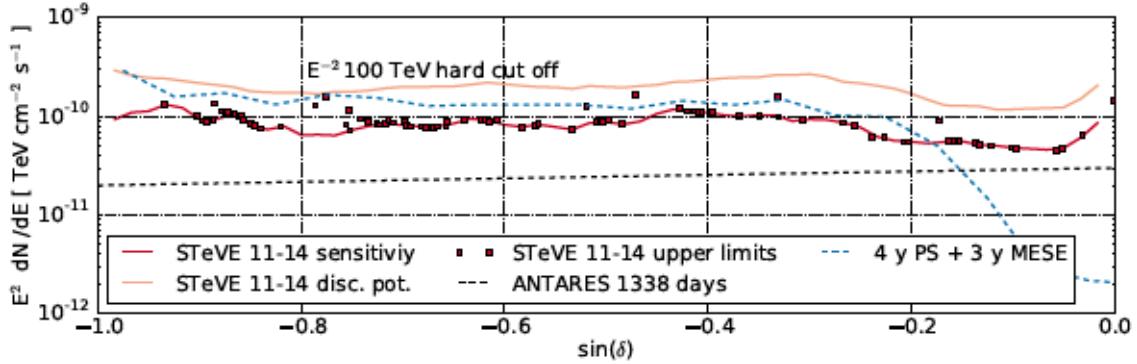
Figure 6.5: Sensitivity for a point-like source for **STeVE** and combined through-going + MESE IceCube search and the ANTARES search. All shown for an E^{-2} neutrino flux with a cutoff at $100\,\mathrm{TeV}$.

and $100\,\mathrm{TeV}$.
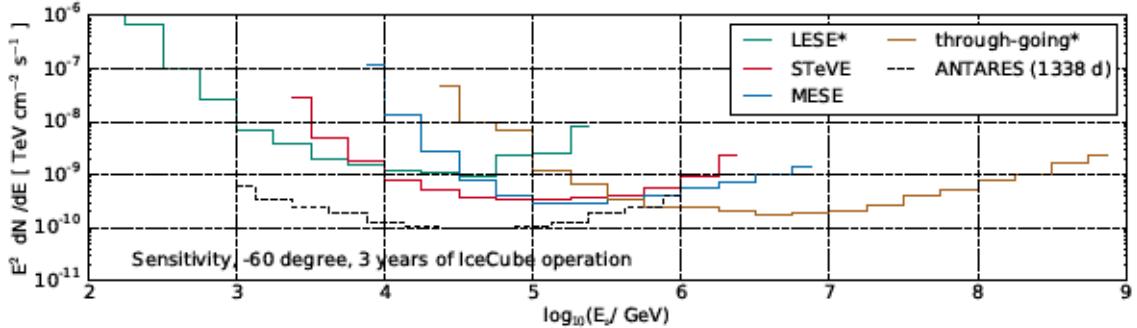
Figure 6.6: The differential sensitivities for four IceCube point-like source searches in the southern sky and ANTARES [193]. The sensitivities for LESE [166]and the through-going analysis [149] are estimated simulating events with a livetime of MESE [165]. For **STeVE** the three years of IC86-II+ are used.

A comparison of the differential sensitivity of all single years and the combined four year differential sensitivity are shown in Fig. 6.7. The three years of IC86-II+ selection perform better than the first year – possibly due to the significant reduction of background events (about 7.5 times less) in combination with comparable effective area and median angular resolution in the most sensitive energy range between $10\,\mathrm{TeV}$ to $1000\,\mathrm{TeV}$. This is caused by the different and improved event selection for IC86-II+. There is no large difference visible between them – not unexpected given the identical event selection and comparable number of livetime ($324\,\mathrm{d}$, $345\,\mathrm{d}$, $362\,\mathrm{d}$).

While it would be possible to redo the IC86-I selection based on IC86-II+ recon-
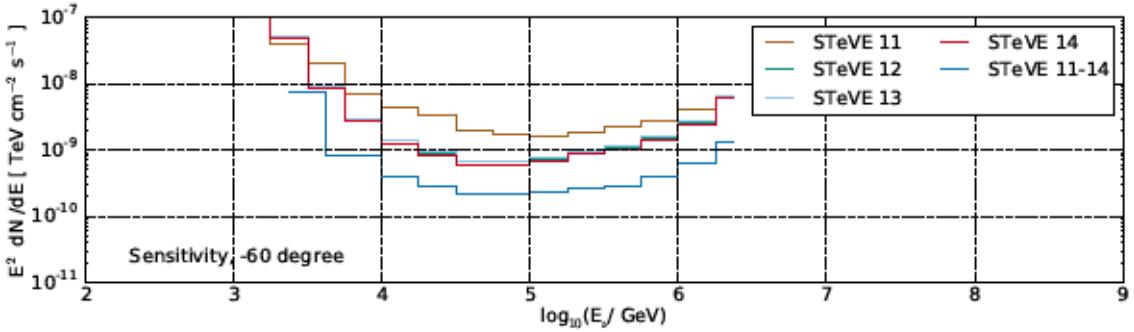
Figure 6.7: Comparison of the differential sensitivities for the four years of data and the combined four year set. The three IC86-II+ years are almost indistinguishable.

struction algorithms and variables, the gain would not justify the resources required to do so.

Can one do better than an energy-zenith PDF? The usage of an energy-zenith PDF as additional LLH term has been used in IceCube searches for point-like emission before. However, due to the similar energy range of background and data for the **STeVE** analysis other variable combinations could yield better results in terms of performance. Three additional LLH implementations were considered and tested: Using only a spatial term, replacing the energy with the BDT score and replacing energy with *length to start*. The sensitivity using these implementations is shown in Fig. 6.8. As the performance is not increased significantly the "traditional" LLH implementation is used. These tests were performed for the IC86-I sample.
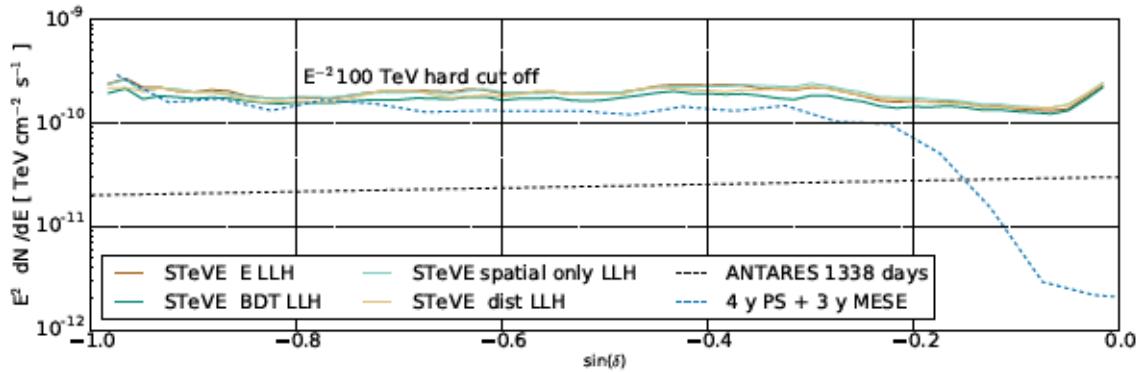

Figure 6.8: Zenith-dependent sensitivity for four LLH implementations for the **STeVE** sample (here only IC86-II (324 days)). For orientation also the sensitivity curves of the MESE + through-going analysis and the ANTARESE analysis are shown. All sensitivities are given for an E_ν^{-2} 100 TeV cutoff scenario.

6.3. Studies of systematic uncertainties

For the generation of the random skies, used to calculate the sensitivity, a seeded random generator is used. The sensitivity calculations differ if different seeds are used. The size of this variation is estimated by calculating the sensitivity for one declination 5,000 times (see Fig. 6.9). On average the calculations differ by less than 1%. In this analysis
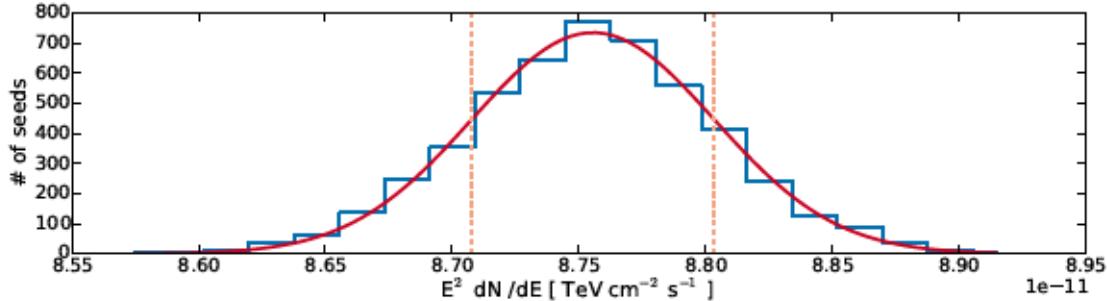

Figure 6.9: Statistic study with 5,000 different seeds used to calculate the sensitivity of the IC86-II+ sample at $-60°$ declination (blue histogram). Also shown is the result of a Gaussian function (solid red line) $a \cdot e^{\frac{-(x-\mu)^2}{2\sigma^2}}$ fitted to this histogram ($a = 735$, $\mu = 8.75 \cdot 10^{-11}$, $\sigma = 4.79 \cdot 10^{-13}$ (indicated by dashed light red lines)).

the background is estimated by scrambling data events. The presented p-values are calculated using only these data events. If the calculated TS or p-value is translated into a sensitivity or upper limit, signal simulation will be required and with this come the uncertainties on detector properties, ice properties, cross-sections, energy losses of muons and properties of the rock below the Antarctic ice.

Here, the uncertainties regarding detector properties are expressed by considering three scenarios. One with the nominal quantum efficiency of the OM to convert arriving photons into charge, one with a quantum efficiency decreased by 10% and one with a quantum efficiency increased by 10%. The uncertainties on the ice properties of scattering and absorption are expressed by four scenarios. One with the ice properties obtained by the best fit in [155], one with the scattering length unchanged but the absorption length decreased by 10%, one with the scattering length decreased by 10% and the absorption length unchanged and one with both absorption and scattering length increased by 7.1%. These three ice scenarios are thought to be very conservative estimations of the uncertainties. Both OM efficiency and ice properties are also investigated combined leading to a total of twelve data sets. For computational reasons this systematic check was performed for the IC86-II+ selection only. However, as the selections perform similar in terms of overall neutrino properties such as effective area and resolution, the results can also be used to estimate the error for the IC86-I selection.

The twelve simulation data sets were processed with the IC86-II+ scheme. To estimate the impact of these systematic changes the zenith-dependent sensitivity for a 100 TeV cutoff was calculated and compared to the base settings. Statistic variations in the sensitivity calculation are minimized by repeating the sensitivity calculation a 100 times with different seeds for the random sky generation and averaging the result and providing a standard error. The ratio of sensitivities is shown in Fig. 6.10, Fig. 6.11, and Fig. 6.12.
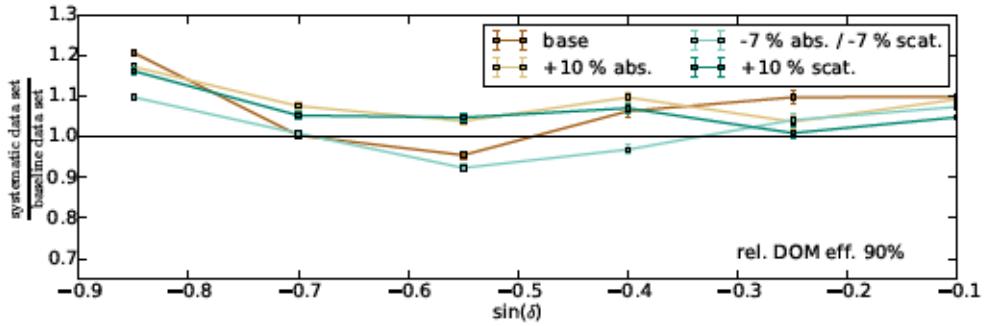

Figure 6.10: Systematic study with -10% OM efficiency and four different realizations of the ice model. Shown is the ratio of the sensitivity over the sensitivity of the baseline dataset.
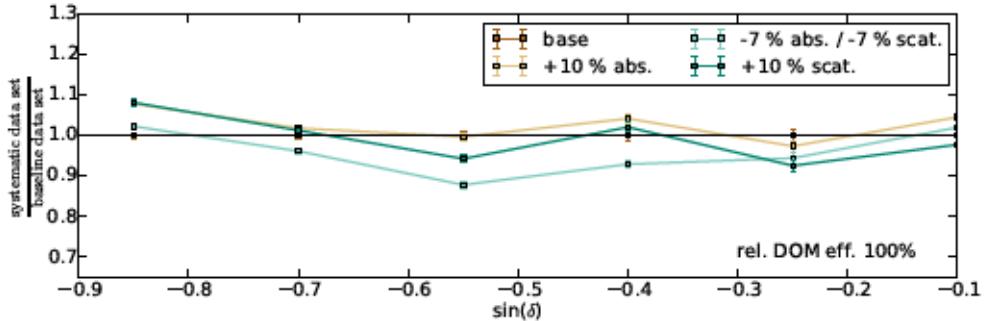
Figure 6.11: Systematic study with nominal OM efficiency and four different realizations of the ice model. Shown is the ratio of the sensitivity over the sensitivity of the baseline dataset.

In general, lower quantum efficiency leads to lower sensitivity. This is expected as this analysis uses energy as a discriminator on several occasions. The deposited energy is usually associated with the detected charge in the vicinity of the energy deposition. Hence, more detected charge leads to higher energy estimates and, hence, leads to higher chances of passing the Level 3 and BDT selection.
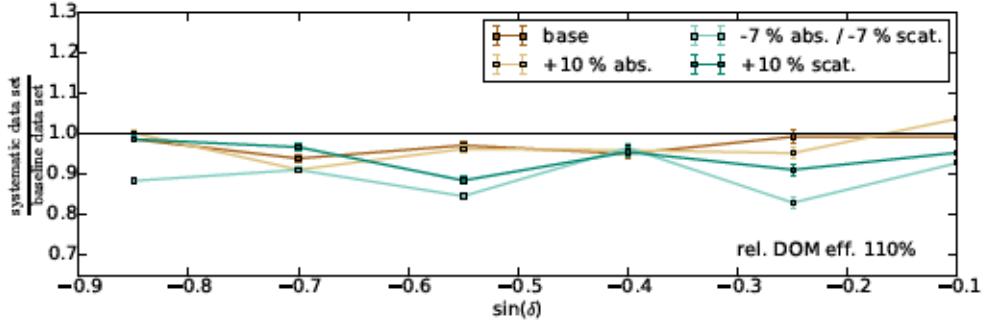
Figure 6.12: Systematic study with +10% OM efficiency and four different realizations of the ice model. Shown is the ratio of the sensitivity over the sensitivity of the baseline dataset.

For the ice properties a similar behavior can be observed. Similar to the quantum efficiency a shorter absorption length leads to less detected charge and, hence, to lower reconstructed energy – reducing the probability of a signal event to pass the event selection. For the increased scattering length two effects have to be taken into account. On the one hand more scattering should, on average, lead to less detected light - decreasing the sensitivity. On the other hand, increased scattering can keep more photons close to the energy loss of the muon leading to a higher charge deposition in OMs close to the track. This could have a positive impact on some of the variables in the BDT (like energy deposited in the largest energy deposition).

A closer look at the presented ratios reveals some inconsistencies. As an example, in Fig. 6.11 at $\sin(\delta)$ = -0.25 the sample with more absorption yields a better sensitvity than the baseline sample. This is not an expected behavior. One possible explanation of increasing absorption enables muons from non-starting events to easier pass the veto conditions is disfavored when the number of total simulated events is compared to the number of simulated starting events (see Fig. 6.13). Both simulation datasets are dominated by starting events and at $\sin(\delta)$ = -0.25 the baseline dataset has less events than the dataset with +10% absorption length. This leaves two possible explanations. First a lack in statistics in simulated events. For this analysis the baseline dataset consists of 45621 simulated events and the dataset with +10% absorption length of 47437 events. Alternatively, this difference can be explained by a selection effect of the BDT that prefers events simulated with more absorption for this declination.

Clarification of this issue requires either more statistics in the present systematic datasets or additional data sets with intermediate ice properties to better understand the transition in sensitivity between them. As both options are not available at this time a conservative estimate of the combined systematic uncertainties on ice and optical module properties of 20 % is assumed.
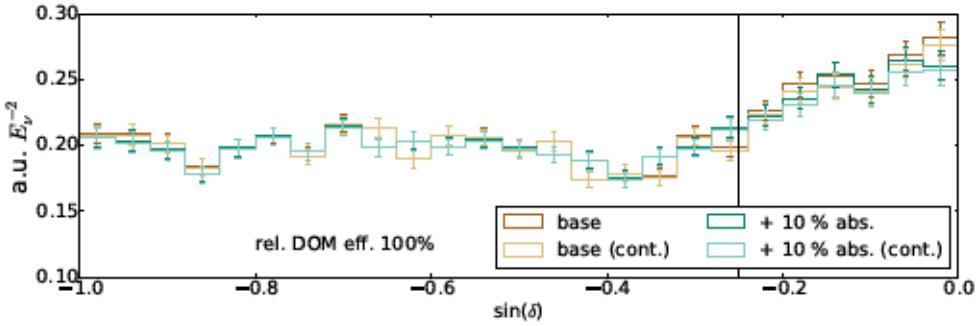
Figure 6.13: Comparison between the expected neutrino events weighted to an arbitrary E^{-2} flux between the baseline ice model and an icemodel with $+10\%$ absorption length. Both the entire simulated neutrino sample and the subsample of events starting inside the detector (lighter colors) are shown. Additionally, the declination on which the $+10\%$ absorption length ice models yields a better sensitivity in Fig. 6.11 is indicated.

Uncertainties on neutrino cross-sections are estimated to be less than 5% following the study in [167].

Tau-neutrinos interacting inside the detector produce a tau. While no such event has been identified yet, in principle a contribution to the **STeVE** selection can be expected from these events. Two scenarios are possible here. For very high energetic taus ($E_\tau > 10\,\mathrm{PeV}$) the track of the tau itself could be reconstructed and the event could be subsequently used in the analysis. For energies below the tau is expected to decay very fast. 17% of the taus decay directly into a muon (and the corresponding neutrinos) [15] which in term can produce a long track. This long track and the large initial energy deposition caused by both the initial neutrino interaction and the tau decay can lead to a signature that is detectable by the **STeVE** selection. For now the contribution of tau-neutrinos is neglected as its overall contribution is expected to be small (14.5% or less if euqal numbers of muon- and tau-neutrinos are expected at Earth.). Implementation of tau-neutrino contribution is expected to slightly improve the results as the number of expected events from a point-like source would be increased.

6.4. Results for the Source Catalog

As has been shown in section 2.5, TeV gamma ray emission could be accompanied by neutrino emission from the same sources. Hence, TeV gamma ray sources are a natural choice to look for point-like emission of neutrinos. The TeVCat presented in section 4.1 provides these sources. To ensure compatibility between the different years of data selection the source candidates used in the analysis of IC86-I are used also for IC86-II+.

Additionally, twelve source candidates used in previous IceCube searches are added. The results of the LLH minimization for each source and upper limits for an E_ν^2 spectrum as well as for three cutoff scenarios can be found in tables 6.1 (Binaries) , 6.2 (SNRs), 6.3 (PWNs) ,6.4 (Clusters), 6.5 (Unidentified sources), 6.6 (Extra-galactic sources) and 6.7 (Others). The twelve sources not present in the TeVCat are indicated by an asterisk. A special case are the three objects found in the Large Magellanic Cloud, a satellite dwarf galaxy of the Milky Way. For this analysis they are added in the category "Others". At a distance of about 50 kpc [8] these sources are in an intermediate distance between galactic and extra-galactic.

HESS J1616-508 is the source candidate with the lowest background probability. It yields a p-value of 0.2 %. Nonetheless, the probability to detect such an overfluctuation in a sample of 96 points by chance has to be accounted for. This can be estimated by scrambling the right ascension of the final level events randomly. By following this approach random skies on which every over-fluctuation is purely coincidental are generated. The usage of many thousand random skies, here 20,000 random skies, helps to estimate the background probability. After correcting for these trials the background probability for HESS J1616-508 becomes 19.8 %, see Fig. 6.14.
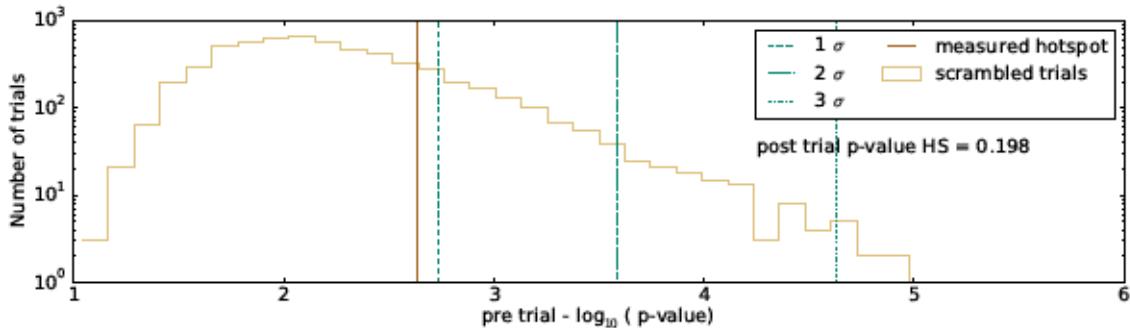

Figure 6.14: Distribution of pre-trial p-values for 20,000 random skies. This distribution is used to evaluate the significance of the measured p-value of the real sky.

Hence, no indication for neutrino emission from any of the investigated source candidates has been found.

6.5. Results for the all-sky scan

This approach is motivated by the possibility of point-like neutrino emission from an object that has not been detected by observation of other messenger particles. This is implemented by evaluating the test statistic on a grid with a binning below the angular resolution of the analysis. The coordinates of the points investigated are provided by a HEALpix [194] grid with a bin width of 0.46°.

Table 6.1.: Table of all sources classified as binaries according to TeVCat. Asterisks indicate the source candidates which are not present in TeVCat but in previous IceCube searches. Listed are the signalness parameter $\hat{n}_s$, the fitted spectral index $\hat{\gamma}$, the calculated background probability before and after trial-correction and the upper limit on the flux for an E^{-2} spectrum without a cutoff and three scenarios with a hard cutoff in units of $10^{-12}\,\mathrm{TeV}^{-1}\mathrm{cm}^{-2}\mathrm{s}^{-1}$. A dash in the $\hat{n}_s$ column indicates a calculated TS of 0. In this case p-values are not given as this is an underfluctuation.

Source	$\hat{n}_s$	$\hat{\gamma}$	p-val$_{pre}$	p-val$_{post}$	$\Phi^{90\%}_{\nu_\mu+\bar{\nu}_\mu} \times 10^{-12}\,\mathrm{TeV}^{-1}\mathrm{cm}^{-2}\mathrm{s}^{-1}$ E_{cut}			
					None	1 PeV	100 TeV	10 TeV
PSR B1259-63	–	–	–	–	36	42	91	1372
HESS J1018-589	–	–	–	–	40	44	92	1233
GX 339-4 *	–	–	–	–	33	37	72	639
LS 5039	–	–	–	–	47	51	82	432
Cir X-1 *	–	–	–	–	34	36	76	1001

Table 6.2.: Table of all sources classified as supernova remnants according to TeVCat. See Tab. 6.1 for a more detailed description.

Source	$\hat{n}_s$	$\hat{\gamma}$	p-val$_{pre}$	p-val$_{post}$	$\Phi^{90\%}_{\nu_\mu+\bar{\nu}_\mu} \times 10^{-12}\,\mathrm{TeV}^{-1}\mathrm{cm}^{-2}\mathrm{s}^{-1}$ E_{cut}			
					None	1 PeV	100 TeV	10 TeV
RCW 86	–	–	–	–	37	43	91	1301
HESS J1800-240B	<0.1	4.0	0.267	1.0	53	60	110	950
SNR G015.4+00.1	–	–	–	–	45	52	85	476
RX J0852.0-4622	–	–	–	–	38	45	81	741
W 28	–	–	–	–	53	57	110	766
SN 1006 SW	–	–	–	–	42	45	80	650
CTB 37A	–	–	–	–	48	49	94	830
CTB 37B	–	–	–	–	47	49	92	781
RX J1713.7-3946	–	–	–	–	45	47	91	832
HESS J1800-240A	1.2	4.0	0.239	1.0	54	61	111	938
SNR G349.7+00.2	1.0	2.5	0.23	1.0	51	54	93	801
HESS J1731-347	–	–	–	–	45	48	81	539
SN 1006 NE	–	–	–	–	41	43	79	628
SNR G318.2+00.1	–	–	–	–	42	47	99	1343
HESS J1745-303	–	–	–	–	41	51	87	690

Table 6.3.: Table of all sources classified as pulsar wind nebula according to TeVCat. See
Tab. 6.1 for a more detailed description.

Source	$\hat{n}_s$	$\hat{\gamma}$	p-val$_{\text{pre}}$	p-val$_{\text{post}}$	$\Phi^{90\%}_{\nu_\mu+\bar{\nu}_\mu} \times 10^{-12}\,\text{TeV}^{-1}\text{cm}^{-2}\text{s}^{-1}$			
							E_{cut}	
					None	1 PeV	100 TeV	10 TeV
HESS J1825-137	–	–	–	–	36	39	61	339
Vela X	2.2	4.0	0.201	1.0	42	48	90	933
HESS J1303-631	–	–	–	–	36	41	89	1355
HESS J1813-178	–	–	–	–	43	50	91	598
HESS J1458-608	0.8	2.3	0.237	1.0	44	51	108	1583
HESS J1718-385	–	–	–	–	48	50	95	829
Kookaburra (PWN)	–	–	–	–	44	50	108	1512
HESS J1708-443	1.5	4.0	0.294	1.0	43	47	86	835
HESS J1831-098	5.4	2.9	0.034	0.973	59	61	90	486
HESS J1640-465	–	–	–	–	38	45	82	726
SNR G327.1-01.1	–	–	–	–	36	40	79	998
HESS J1837-069	–	–	–	–	34	35	50	202
HESS J1026-582	–	–	–	–	36	40	83	1097
HESS J1632-478	3.6	4.0	0.115	1.0	44	50	94	992
Kookaburra (Rabbit)	–	–	–	–	43	49	106	1496
SNR G292.2-00.5	3.6	4.0	0.134	1.0	48	53	111	1757
HESS J1809-193	–	–	–	–	50	57	100	654
HESS J1356-645	–	–	–	–	40	47	99	1464
SNR G000.9+00.1	9.2	3.9	0.007	0.5	76	90	162	1591
MSH 15-52	1.9	4.0	0.166	1.0	43	48	99	1400
HESS J1616-508	4.4	2.2	0.002	0.198	70	79	157	1963
IGR J18490-0000	0.4	4.0	0.117	1.0	97	98	142	477
HESS J1846-029	–	–	–	–	32	32	47	164

Table 6.4.: Table of all sources classified as clusters according to TeVCat. See Tab. 6.1 for a more detailed description.

Source	$\hat{n}_s$	$\hat{\gamma}$	p-val$_{pre}$	p-val$_{post}$	$\Phi^{90\%}_{\nu_\mu+\bar{\nu}_\mu} \times 10^{-12}\,\text{TeV}^{-1}\text{cm}^{-2}\text{s}^{-1}$ E_{cut}			
					None	1 PeV	100 TeV	10 TeV
HESS J1614-518	3.1	2.2	0.013	0.742	58	64	127	1702
Westerlund 2	–	–	–	–	36	38	80	1032
Westerlund 1	–	–	–	–	38	43	85	739
HESS J1848-018	–	–	–	–	43	44	64	225
Terzan 5	–	–	–	–	54	61	113	1068

Table 6.5.: Table of all sources classified as unidentified according to TeVCat. See Tab. 6.1 for a more detailed description.

Source	$\hat{n}_s$	$\hat{\gamma}$	p-val$_{pre}$	p-val$_{post}$	$\Phi^{90\%}_{\nu_\mu+\bar{\nu}_\mu} \times 10^{-12}\,\text{TeV}^{-1}\text{cm}^{-2}\text{s}^{-1}$ E_{cut}			
					None	1 PeV	100 TeV	10 TeV
HESS J1626-490	2.8	3.2	0.218	1.0	37	42	82	857
HESS J1634-472	2.1	4.0	0.18	1.0	41	48	89	883
HESS J1804-216	–	–	–	–	48	52	101	583
HESS J1808-204	–	–	–	–	51	57	102	630
HESS J1729-345	–	–	–	–	45	48	82	541
HESS J1708-410	1.9	2.6	0.286	1.0	45	48	87	777
HESS J1834-087	–	–	–	–	37	38	55	245
HESS J1641-463	–	–	–	–	38	44	82	753
HESS J1841-055	–	–	–	–	33	34	47	171
HESS J1427-608	–	–	–	–	43	49	107	1536
HESS J1843-033	–	–	–	–	31	32	46	157
HESS J1507-622	4.4	2.3	0.039	0.986	38	44	92	1328
HESS J1741-302	–	–	–	–	41	51	88	702
HESS J1702-420	–	–	–	–	40	43	78	629
Galactic Centre	–	–	–	–	41	48	84	656
HESS J1832-093	–	–	–	–	39	39	55	258
HESS J1503-582	–	–	–	–	37	40	83	1103

Table 6.6.: Table of all sources classified as extra galactic according to TeVCat. See Tab. 6.1 for a more detailed description.

Source	$\hat{n}_s$	$\hat{\gamma}$	p-val$_{pre}$	p-val$_{post}$	$\Phi_{\nu_\mu+\bar{\nu}_\mu}^{90\%} \times 10^{-12}\,\mathrm{TeV}^{-1}\mathrm{cm}^{-2}\mathrm{s}^{-1}$ E_{cut}			
					None	1 PeV	100 TeV	10 TeV
PKS 1454-354 *	–	–	–	–	43	47	78	562
PKS 1622-297 *	1.2	4.0	0.278	1.0	43	53	92	795
H 2356-309	0.6	4.0	0.33	1.0	42	51	88	728
Centaurus A	–	–	–	–	40	43	79	645
1ES 0347-121	–	–	–	–	36	36	54	304
AP Lib	–	–	–	–	54	61	110	973
PKS 1406-076 *	–	–	–	–	37	37	53	217
PKS 0727-11 *	–	–	–	–	36	37	54	304
SHBL J0013-188	<0.1	3.3	0.425	1.0	47	54	94	609
KUV 00311-1938	6.7	2.8	0.05	0.995	79	89	159	1059
QSO 1730-130 *	1.6	2.5	0.45	1.0	38	39	59	359
ESO 139-G12 *	–	–	–	–	44	49	105	1449
1ES 1101-232	<0.1	4.0	0.308	1.0	54	58	108	811
1RXS J1010-311	4.9	4.0	0.051	0.996	59	69	122	1213
PKS 0454-234 *	–	–	–	–	55	59	110	802
PKS 0548-322	<0.1	4.0	0.437	1.0	39	45	75	568
NGC 253	–	–	–	–	54	61	118	1095
PKS 2155-304	0.7	3.5	0.324	1.0	43	51	89	743
PKS 1510-089	–	–	–	–	37	38	55	257
PKS 0426-380 *	–	–	–	–	46	47	90	753
PKS 0301-243	–	–	–	–	54	60	108	932
QSO 2022-077 *	–	–	–	–	35	36	51	216
1ES 1312-423	–	–	–	–	39	42	77	646
3C 279	–	–	–	–	34	35	48	174
PKS 2005-489	6.9	3.2	0.037	0.982	51	58	115	1301
PKS 0447-439	–	–	–	–	39	43	79	655
PKS 0537-441 *	–	–	–	–	39	43	80	685

Table 6.7.: Table of all sources that do not belong to any of the categories above. These are the Vela Pulsar and the three objects in the Large Magellanic Cloud: SNR LMC N132D, supperbubble 30 Dor C and PWN LHA 120-N 157B. See Tab. 6.1 for a more detailed description.

Source	$\hat{n}_s$	$\hat{\gamma}$	p-val$_{pre}$	p-val$_{post}$	$\Phi^{90\%}_{\nu_\mu+\bar{\nu}_\mu} \times 10^{-12}$ TeV^{-1}cm^{-2}s^{-1}			
					E_{cut}			
					None	1 PeV	100 TeV	10 TeV
Vela Pulsar	1.1	4.0	0.293	1.0	40	45	86	836
LMC N132D	–	–	–	–	43	56	129	1943
LHA 120-N 157B	–	–	–	–	46	57	132	2015
30 Dor C	–	–	–	–	46	57	132	2013

After evaluating the likelihood at every point of the sky the point with the lowest background probability defines the "hottest spot". While the background probability of such a point being significant due to background fluctuations is very low, in the combined four years of **STeVE** as low as $10^{-4.93}$, this has to be related to the large number of analysed points (trials) in the sky (here 98304^3 points). As discussed above randomly generated skies can be used by scrambling the event's right ascension and calculating the hottest spot for each of them. Now, it can be evaluated how significant the "hottest spot" of the real sky map is in comparison. A histogram of the p-values for 20,000 random skies and the measured "hottest spot" is shown in Fig. 6.15. With 34.4 % of random skies generating a "hottest spot" equal or more significant this is well within the expectations of a background-only hypothesis.
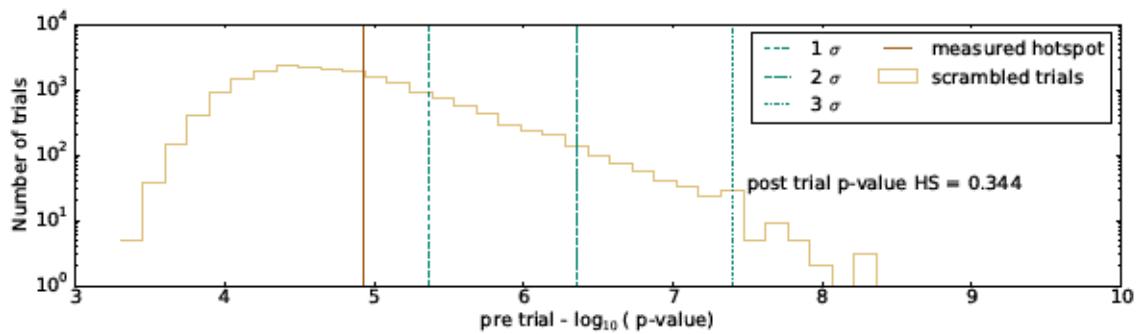
Figure 6.15: Distribution of pre-trial p-values for 20,000 random skies. This distribution is used to evaluate the significance of the measured p-value of the real sky.

---

[3]Half of the grid point of a healpy map with a bin width of 0.46° / nside = 128.

Hence, there is no indication for a point-like source of neutrino emission. The p-value map of the southern sky is shown in Fig. 6.16. Three additional points of comparable significance are also visible by eye. With the most significant point described well by the background only hypothesis this is also true for them. Additionally, three of four points are close to the horizon. In this region, the search with through-going events and the search combining MESE and through-going events provide a better sensitivity than **STeVE**.
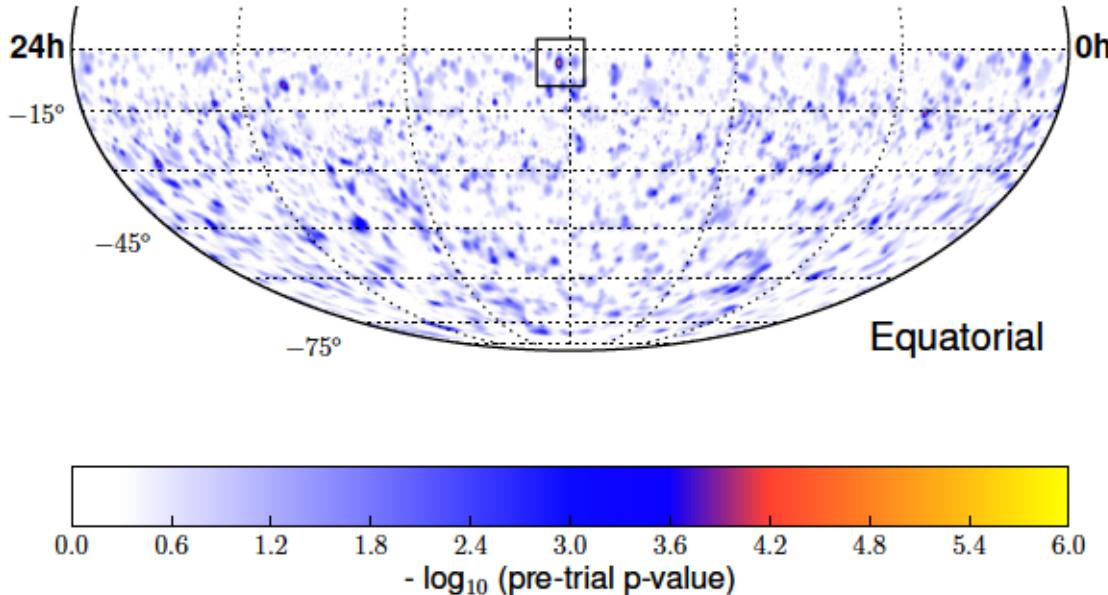
Figure 6.16: Four year skymap of the Southern sky with **STeVE**. The point with the lowest background probability is indicated by the black box.

6.5.1. Discussion of the results

Comparison with other IceCube searches

This search improves the sensitivity of IceCube for sources of point-like neutrino emission below 100 TeV in the southern sky by about 50 % to 100 %. For very horizontal points, closer than 10° to the horizon, the combined through-going and MESE search is more sensitive. Below 10 TeV **STeVE** performs worse than the LESE search - optimized for this energy range. The results of all IceCube analyses presented here (through-going, MESE, **STeVE** and LESE) are in agreement with the background-only hypothesis.

Comparison with other ANTARES searches

The sensitivity of ANTARES for a 100 TeV cutoff scenario is a factor two to four better than the sensitivity of **STeVE**. Similar to the other IceCube searches, the ANTARES data

is in agreement with the background-only hypothesis. Direct comparison of the ANTARES and the STeVE sample provides explanation of the difference in sensitivity. While both have a comparable effective area above 3 TeV, the ANTARES selection profits from both a lower number of background events – 4136 in 1338 days for ANTARES [195] compared to 15043 events in 337 days for the IC86-I selection or 7005 events in 1030 days for the IC86-II+ of STeVE and a better median angular resolution of ~0.4° [195]. The difference in sensitivity becomes more significant for energies below 10 TeV. Here, the effective area of STeVE is smaller and the median angular resolution worsens (larger than 2°).

Revisiting the gamma-neutrino connection

The gamma-neutrino models discussed in section 2.5.1 can be used and and related to the calculated TS. A similar approach has been chosen for the E_ν^{-2} scenarios with and without energy cutoff given in section 6.4. Using the parametrization given in [97] a model rejection factor (MRF) can be calculated. The MRF is defined as the upper limit over the flux prediction. Values smaller than one restrict the model, larger ones do not restrict the model. For some of the sources discussed in the paper (PWN VelaX and SNR RX J1713.7-3946) the ANTARES collaboration gives upper limits, e.g. in [162]. These and the upper limits provided by STeVE for both the most promising SNR and PWN candidates are shown and compared to the model predictions in Fig. 6.17 and in Fig. 6.18.

Neither the analysis by the ANTARES collaboration nor this analysis can restrict the models. Given the small sensitivity of STeVE for neutrinos below 10 TeV and the steep spectra and / or cutoff in energy at a few TeV or below for the sources it seems very challenging to restrict these models with STeVE even with additional years. Here, again the focus of the analysis on energies between 10 TeV and a few 100 TeV becomes visible. Both PWN have a higher expected neutrino flux between 50 TeV to 500 TeV yielding better rejections factors while the large contribution of neutrinos in the 10 GeV to 1000 GeV for the SNR is almost inaccessible for the STeVE analysis.

The differential sensitivity at the source declination for the four sources discussed here can be used to estimate to which part of the predicted flux the STeVE analysis is most sensitive. For this the differential sensitivity was calculated with a fine binning of twenty bins per energy decade, five times as fine as for the discussion in section 6.2. Inverted and multiplied with the flux prediction this yields a unit-less quantity, here called differential model rejection factor (DMRF), see Fig. 6.19.

While the absolute value of this quantity is arbitrary due its dependence on the width of bins for the differential sensitivity one can rank the bins according to it. Inspired by [196] the DMRFs of these ranked bins are added up until the sum is larger than 90 % of the total DMRF. The energy range provided by this method can be seen as an estimate of the sensitivity range of STeVE to a certain flux model and is indicated by a red line in Fig. 6.17 and Fig. 6.18. This quantity can help to visualize the "peak-sensitivity" of
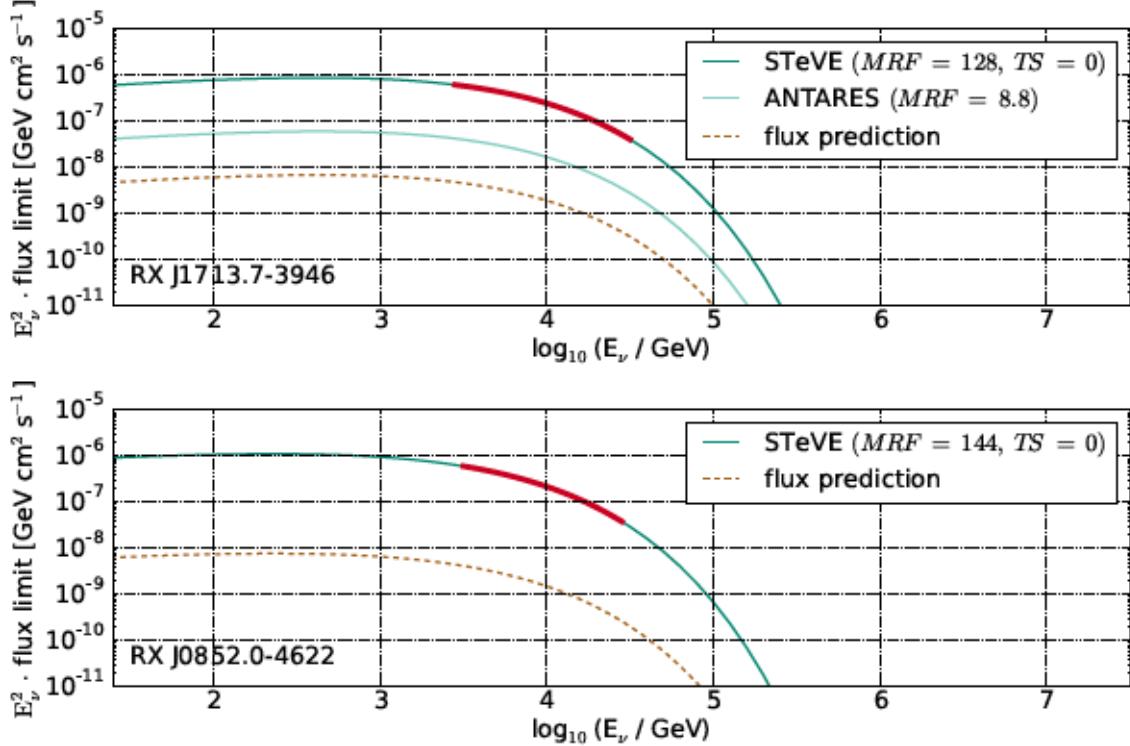
Figure 6.17: Upper limits and MRFs on neutrino emission predicted from the hadronic production model discussed in [97] for two supernova remnants. The results for ANTARES are taken from [162].

the analysis.

Similar to the SNRs and PWNs discussed above the observed gamma ray emission from the Galactic Centre can also be used to predict a neutrino flux [81]. However, similar to other galactic candidates the **STeVE** analysis can not confirm or restrict these models with the given sensitivity, see Fig. 6.20. As expected, the limits for scenarios with a higher cutoff yield better MRF as both more and higher energetic neutrinos are predicted.

How do the results of STeVE relate to the observed diffuse neutrino flux?

IceCube has measured a flux of astrophysical neutrinos. To investigate the relation between this flux and the results from **STeVE** some assumptions about its properties have to be made. First, the origin from a pion decay scenario. Every charged pion decay yields two (anti-)muon-neutrinos and one (anti-)electron-neutrino. As discussed in section 3.1.1, this becomes on average one of each flavor at Earth. Hence, a measurement of muon neutrinos can account for one third of the total astrophysical neutrino flux.
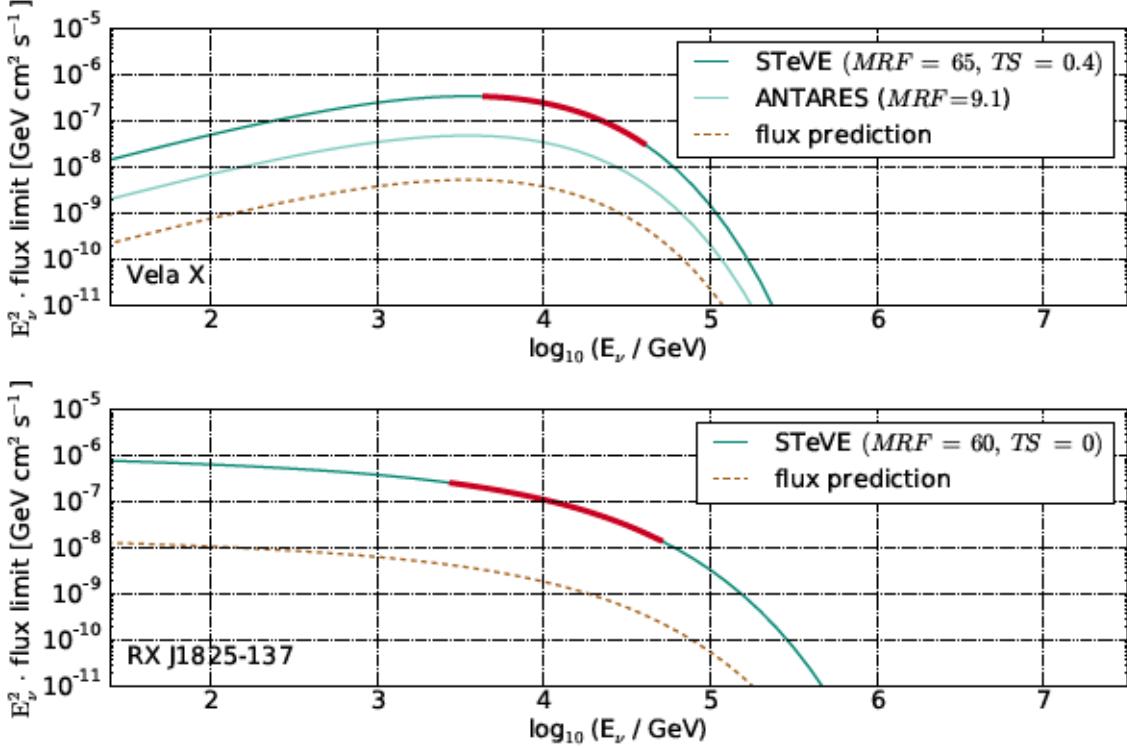
Figure 6.18: Upper limits and MRFs on neutrino emission predicted from the hadronic production model discussed in [97] for two pulsar wind nebulae. The results for ANTARES are taken from [162].
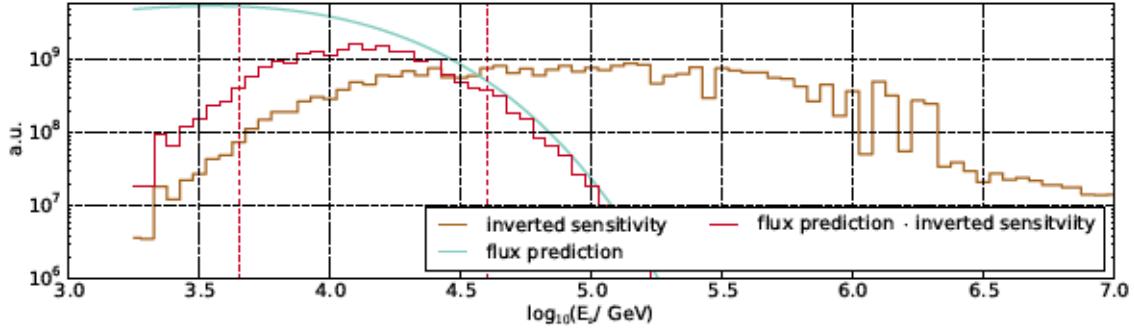
Figure 6.19: Example for the procedure that yields the differential model rejection factor (DMRF). The differential sensitivity at source position is inverted (brown line) and multiplied with the flux prediction (light blue line) in the center of the differential sensitivity bin, yielding the DMRF (red line). For this plot the three curves are scaled to fit in the same plot. The range of the bins yielding 90% of the total DMRF is indicated by two dashed red lines.
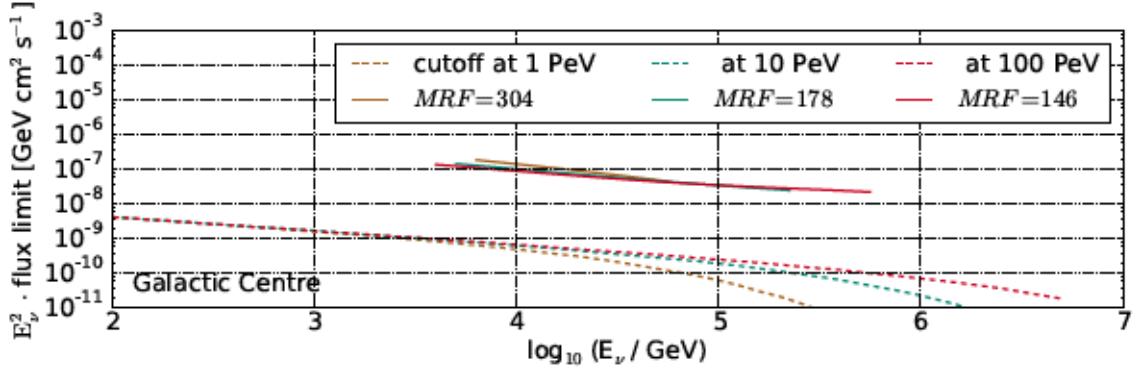
Figure 6.20: Upper limits and MRFs on neutrino emission predicted from the hadronic production model discussed in [81] for the Galactic Centre. The three models shown here assume an exponential cutoff in the parent proton spectrum at 1 PeV (brown), 10 PeV (turquoise) or 100 PeV (red).

As already discussed above, **STeVE** is most sensitive below 100 TeV. Thus, here the discovery potential for **STeVE** in a 100 TeV cutoff scenario is compared to the average diffuse flux below 100 TeV. Here, it is assumed that a point-like source is just below the average discovery potential of **STeVE**, see Fig. 6.5. This point-like source flux is then divided by 4π to translate it into a diffuse flux. As can be seen in Fig. 6.21, a potential point source just below the **STeVE** discovery flux would contribute 30% to 50% to the measured overall diffuse neutrino flux. This is in disagreement with isotropy measurements of the diffuse neutrino flux. Since the **STeVE** all-sky scan is in very good agreement with the background-only analysis, there is no indication for any single point-like source "around the corner". At the moment the differential diffuse flux is only provided for the entire sky, due to low event counts.
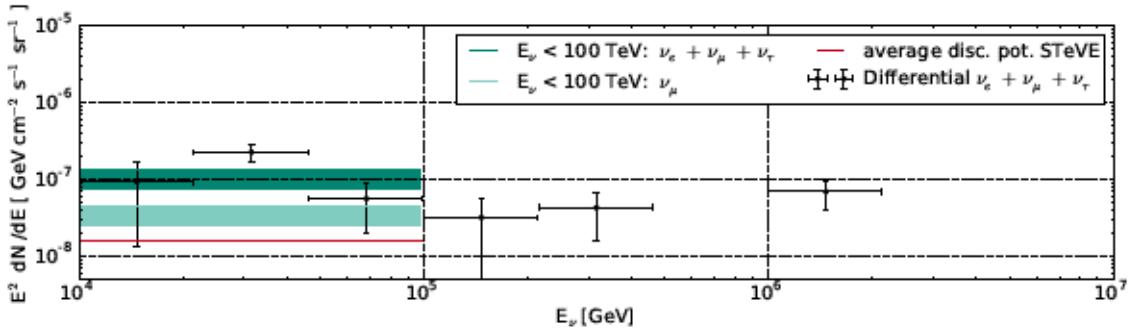
Figure 6.21: Shown here are the measured differential astrophysical neutrino flux, taken from [92], a fit of an E^{-2} spectrum to the data points below 100 TeV, and the predicted contribution of muon neutrinos to this flux. This is compared to the average discovery potential of **STeVE** transformed into a diffuse all-sky flux.

The calculated upper limits for the sources investigated in section 6.4 can also be related to the diffuse astrophysical neutrino flux. Here, the sum of all upper limits of one source class is compared to the diffuse astrophysical muon neutrino flux below 100 TeV. As shown in Fig. 6.22, only for the small source classes of binaries and galactic clusters (both consist of five sources) the sum of all upper limits is of the same magnitude as the measured diffuse flux. In combination with the observed isotropy of the diffuse flux it can be argued that these specific five sources cannot account for the observed diffuse flux.
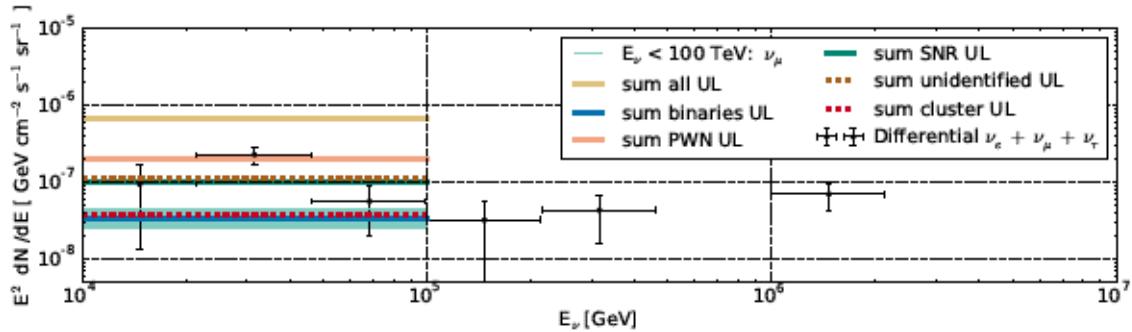
Figure 6.22: Like in Fig. 6.21 the differential diffuse flux and the predicted contribution of muon neutrinos to a fitted E^{-2} spectrum below 100 TeV are shown. Also shown are the sum of all upper limits for certain source classes of the **STeVE** analysis.

It should be noted that the method of summing up individual upper limits is inferior to a dedicated stacking analysis calculating the contribution to the diffuse flux as used in [149, 182, 197].

6.6. Future application of the STeVE event sample

The analysis presented here focused on potential neutrino emission from both known (source list) and unknown (all-sky scan) steady point-like sources. Three possible extensions to this source hypothesis deserve further investigation.

First, the event selection can be used to search for time-dependent emission. As briefly discussed in section 2.3, many sources have phases of high gamma emission. Time-dependent searches [198–200] take advantage of this to reduce the number of background events.

Second, extended regions of neutrino emission like the galactic plane or the Fermi bubbles, large spherical structures with a radius of the order 50° above and below the center of our Galaxy [58] can be investigated. The size of these regions increases the

number of background events. Poor angular resolution compared to other searches from ANTARES or IceCube might lead to relative smaller losses in sensitivity - making the **STeVE** sample interesting for extended source regions.

Third, using the event selection for a stacking analysis can help to find or restrict contribution of entire source classes to the diffuse neutrino flux. Supernova remnants are an obvious candidate due to observed gamma rays in the TeV range and the evidence for hadronic processes within them, as discussed in section 2.4.

One disadvantage compared to the ANTARES analysis is the worse angular resolution. This has (at least) three reasons. First, the optical properties of sea water and the deep glacial ice at the South Pole are different. While the ice has a longer absorption length, its scattering length is shorter. Hence, more directional information is lost in ice. Second, there is a decreased lever arm of a starting track compared to a through-going track. This cannot be changed if starting tracks are used as separation between atmospheric muons and astrophysical neutrinos.

The last point is the performance of the algorithm. The hypothesis used at the moment is a through-going muon track without stochastic energy losses. This does not represent the truth realistically. One other algorithm that might be suited to improve the angular reconstruction is the topology energy reconstruction described in section 5.2.5. The results of the energy loss fit can be used to calculate a likelihood. This likelihood can then be used as parameter for a minimizer to find the best fitting particle track. This algorithm provides a better median angular resolution than the MPE LLH algorithm using splines (about $0.4°$ below $10\,\mathrm{TeV}$ and about $0.1°$ above $1\,\mathrm{PeV}$), see Fig. 6.23. A disadvantage is that it is computationally expensive. This would become more problematic, if additional fits to estimate its error are needed. Nonetheless, in case of a very low background probability for a source it might be of worth to invest these computational resources.
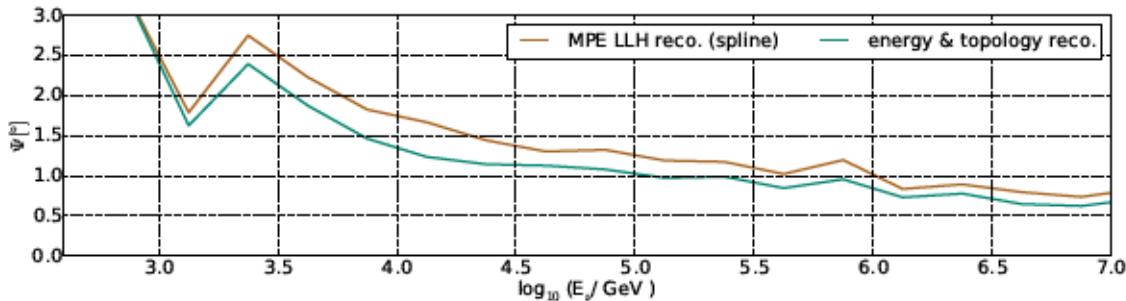
Figure 6.23: Median angular reconstruction for the MPE LLH algorithm using splines that is used for the **STeVE** analysis and for the energy and topology reconstruction discussed in section 5.2.5 used as angular reconstruction.

6.6.1. Path to a combined southern sky IceCube sample

Four general purpose event selections in the southern sky exist for IceCube in the 86 string configuration. All of them provide peak sensitivity at different energy ranges as discussed in section 6.2 and visible in Fig. 6.6. For the MESE and through-going event selection a joint sample was created by excluding every event passing the MESE event selection from the through-going sample for both signal and data. Since the through-going event sample relies on energy to discriminate background and signal, the average MESE signal event has only a low contribution to the sensitivity in the through-going sample.

One trivial way to add **STeVE** to this combined event selection is the exclusion of events with more than 1500 PE of deposited charge in the detector. Due to the charge threshold of MESE at this value the samples would be disjunct. For the merging of the through-going and the **STeVE** analyses, it has to be investigated how disjoint the two samples are. If the separation of MESE and **STeVE** search is achieved by a charge cut, the overlap between the through-going and the **STeVE** sample will be expected to be small for all but horizontal events due to the energy-dependent selection of the through-going sample [149]. At the horizon the background of atmospheric muons is very small, making the through-going sample viable even for lower energies. Here, the charge cut alone might not be a sufficient separator as it would also reject through-going tracks with deposited energy in the TeV range. Discarding all events that pass the FSS filter from the through-going track search can be an additional criterion.

Combining LESE and **STeVE** can be achieved by excluding events from the LESE event sample that pass the Level 3 cuts of **STeVE**. The proposed decision tree on how to separate the event samples can be found in Fig. 6.24. This scheme has the advantage that it is simple and relies on variables already available on Level 2 – making it in theory also viable for fast searches like an optical follow-up program. A disadvantage is that it is very likely to not separate optimally in terms of overall sensitivity.
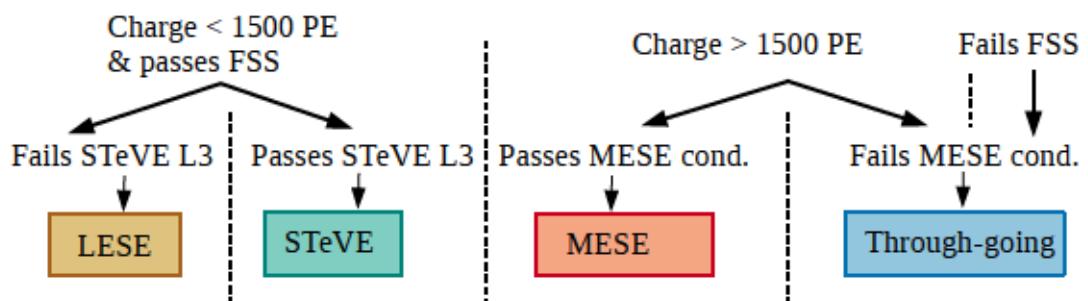
Figure 6.24: Sketch of the proposed scheme to merge the four IceCube point-like source search event samples.

7. Conclusions and Outlook

7.1. Summary and implications

The analysis presented here, **STeVE**, aimed at detecting neutrino emission from a point-like source in the southern sky. This region of the sky hosts the Galactic Center and many other galactic sources of TeV gamma ray emission which might be connected to astrophysical neutrinos and are candidate sites for cosmic ray acceleration. The detection of neutrinos from these sites would be a "smoking gun" for hadronic acceleration. While the astrophysical neutrino flux has been measured by the IceCube detector, there has not been any indication of an origin from one or more point-like sources. Hence, the sources of astrophysical neutrinos are still unknown.

For this search, data taken by the IceCube neutrino telescope between May 2011 and May 2015 has been used. The main challenge of this work is suppressing the background of atmospheric muons, which outmatches the second largest background of atmospheric neutrinos by about a factor 10^6 and amounts to almost a 100 billion events triggered and reconstructed with fast algorithms by the detector each year. The reconstructions different between the data taken between May 2011 and May 2012 and the data taken between May 2012 and May 2015. Thus, two different event selections were used in this analysis.

The strategy to suppress background followed in this study is the selection of events with a starting track topology. These events occur when a muon neutrino interacts within the detector volume and a track is detected that starts inside the detector. A filter developed to search for starting tracks is used to preselect these events. In combination with this filter the energy of the event is used to discriminate low energetic atmospheric muons from neutrinos withenergies between $10\,TeV$ to $100\,TeV$. These two selection steps reduce the number of background events by about a factor 100 while keeping more than $50\,\%$ of all starting muon neutrino events with $E_\nu > 10\,TeV$.

The remaining events are then reconstructed with better, but computationally more expensive algorithms. Variables calculated on the basis of these reconstructions are then used to train a boosted decision trees algorithm to further reduce the number of background events. This final selection leads to a number of 15043 events for the first year of data used here and 7005 events for the sum of the three following years. Almost all of these events are expected to be atmospheric muons – with exception of a few hundred atmospheric muons and about 37 expected astrophysical neutrinos from the

diffuse flux. The median angular resolution is about 2° at 10 TeV and the effective area for muon neutrinos is comparable with that of the ANTARES detector, located in the Mediterranean Sea, above a few TeV.

The search for point-like emission is performed using an unbinned likelihood method. No indication for a point-like source has been found in both a scan of the sky and a list of source candidates. While this search improved the sensitivity for IceCube in the southern sky for energies below 100 TeV, the ANTARES detector provides better sensitivity for equal livetime. This is not unexpected as ANTARES benefits from a better angular resolution and can use the Earth as shield against atmospheric muons. Being dominated by atmospheric neutrinos this yields a number of background events roughly half the one of the IC86-II+ selection.

The findings of this search were used to relate them both to the detected diffuse astrophysical neutrino flux and to a model connecting detected gamma ray spectra to neutrino emission. If this search had detected a source of point-like neutrino emission, it would have significantly contributed to the detected astrophysical flux (about 50%). The predicted neutrino flux from a model connecting gamma rays and neutrinos is in general too low to be constrained by this analysis.

7.2. Outlook

The current generation of neutrino telescopes is approaching a limit in terms of sensitivity for point-like sources. Additional years of data will only slowly improve the sensitivity. Improvements in data selection and reconstruction can happen, but the level of improvement is hard to predict.

The future for STeVE Additional years of data will improve the sensitivity, as shown in Fig. 7.1. It seems to be very challenging to even reach the current sensitivity of the ANTARES search. However, for every year of data taking the **STeVE** search will add more days due to the better up time.
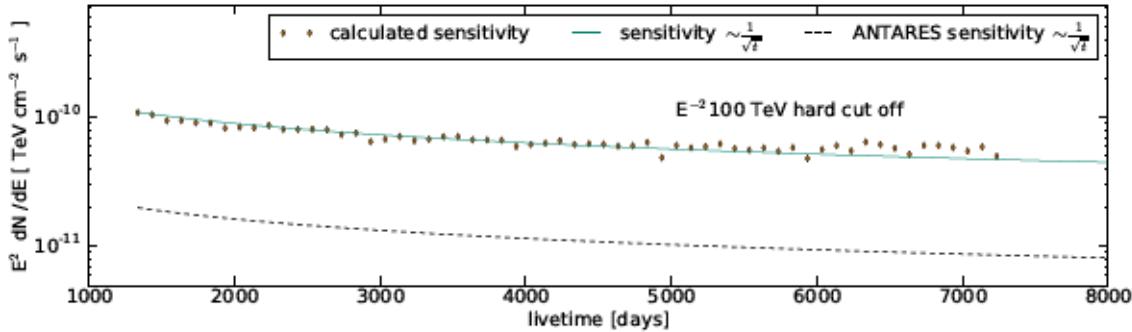
Figure 7.1: The gain in sensitivity by adding additional days or years to the current livetime of the **STeVE** and ANTARES analyses. For **STeVE** both the expected sensitivity by simulating additional livetime and by assuming a gain proportional to $\frac{1}{\sqrt{t}}$ are shown. For ANTARES [159] only the gain proportional to $\frac{1}{\sqrt{t}}$ is shown as it does not require access to the underlying data. The sensitivity is calculated at $-60°$ for an E^{-2} spectrum with a cutoff at $100\,\mathrm{TeV}$.

A new generation of detectors will enter the field Eventually, a new generation of neutrino telescopes is required for further improvement in terms of sensitivity. At the moment three projects are either in planning or construction stage which are expected to improve sensitivity for both the detected diffuse astrophysical neutrino flux and the search for point-like sources. Two of them, KM3NeT in the Mediterranean Sea, and GVD in lake Baikal are to be operated in the Northern hemisphere. Hence, they can use the Earth as shield against atmospheric muons for objects in the southern hemisphere. This has the large benefit that analyses are not limited to use only starting or very high energetic neutrino events in a search for point-like sources.

The strength of this effect is already visible when comparing the sensitivity of the ANTARES detector and the IceCube searches for neutrino energies below $100\,\mathrm{TeV}$. The ANTARES detector is about a factor 100 smaller than IceCube and still outperforms it by a factor of five. Another potential advantage is the use of cascade-like signatures for point-like sources. While the resolution is poor in IceCube, there are indications that a $2°$ resolution might be feasible in water [137] due to its better suited optical properties.

In their Letter of Intent [137] the KM3NeT collaboration presents the prospects to detect SNR RXJ1713 and PWN Vela X using comparable models as discussed in this thesis in section 2.5.1 and section 6.5.1. For these models, they expect a required observation time to detect a neutrino flux of seven years for the PWN and twelve years for the SNR at the 5σ level .

In the southern hemisphere an extension/ successor of the IceCube detector is planned

[201]. Part of these plans are the addition of strings around the IceCube detector, but with increased spacing, and a larger surface array to detect and veto cosmic ray showers.

The increased volume of the detector will increase the volume usable for a search for starting events. However, starting events are only a useful event topology if the number of background events can be reduced to a few thousand or less. The increased spacing between the new strings might make it easier for atmospheric muons to pass the veto region without depositing charge in one of the OMs. For galactic TeV sources the vetoing of atmospheric muons could become even more challenging than it is now.

The enlarged surface array could be used to veto muons in IceCube that are accompanied by a detected cosmic ray shower. If the veto efficiency is very high (approaching 100 %) any down-going event detected will almost certainly be an astrophysical neutrino. For galactic TeV sources a surface veto is confronted with two difficulties. First, the Galactic Centre and many sources along the Galactic Plane are around $-30°$ declination or below. Hence, a surface veto capable to detect cosmic rays from this direction has to extend several kilometres over the footprint of IceCube and its extension. Second, the detection efficiency has to be very high. In most design studies for the surface array it only achieves high signal purity above 100 TeV neutrino energy while TeV neutrinos from (most) galactic sources are expected.

While an extension of the IceCube detector would give higher statistics for neutrinos with energies above 100 TeV, it seems very challenging to find a design that can provide significant improvement for southern TeV sources without being prohibitory expensive.

The discovery of a galactic point-like source of TeV neutrino emission is in reach, but might take another decade.

8. Acknowledgements

This thesis is the culmination of a one decade-long journey through the amazing world of physics. Following this path lead to interaction with many people I owe my gratitude.

First I would like to think my adviser, professor Alexander Kappes, for giving me the opportunity to do the research leading to this thesis. His advice and guidance as well as his support were always welcome.

Also I am grateful for everyone who agreed to be part of my committee.

I would like to thank the entire astroparticle community in Zeuthen and especially the IceCube group for the countless scientific and social activities they offered to me.

Big thanks to Dr. Rolf Bühler, Dr. Juan-Pablo Yanez, Dr. Thorsten Glüsenkamp and Mister Angel Cruz for proof-reading my thesis and their suggestions. To Emanuel Jacobi and Hans-Peter Bretz: It might not have been the most productive idea to put us in an office- but I think it was the best. To all my friends: You are superior!

To my parents who have supported me both financially and otherwise thank you for spending over 40 000 Euros on me learning about "particle stuff"!.

My last and biggest thanks goes to Sabrina. Her endless support, optimism and motivation made this possible.

Bibliography

[1] M. S. Longair. *High energy astrophysics*, volume 1. Cambridge University Press, 2. edition, 1992. ISBN 0 521 38374 6.

[2] T. K. Gaisser, T. Stanev, and S. Tilav. Cosmic Ray Energy Spectrum from Measurements of Air Showers. *Front. Phys. China*, 8:748–758, 2013. doi: 10.1007/s11467-013-0319-7, arXiv: 1303.3565.

[3] V. Berezinsky, A. Gazizov, and S. Grigorieva. On astrophysical solution to ultrahigh energy cosmic rays. *Phys. Rev. D*, 74:043005, Aug 2006. doi: 10.1103/PhysRevD.74.043005.

[4] D. J. Bird, S. C. Corbato, H. Y. Dai, et al. The cosmic-ray energy spectrum observed by the Fly's Eye. *Astrophys. J.*, 424:491–502, March 1994. doi: 10.1086/173906.

[5] A. Calvez, A. Kusenko, and S. Nagataki. Role of galactic sources and magnetic fields in forming the observed energy-dependent composition of ultrahigh-energy cosmic rays. *Phys. Rev. Lett.*, 105:091101, Aug 2010. doi: 10.1103/PhysRevLett.105.091101.

[6] A. M. Hillas. The Origin of Ultra-High-Energy Cosmic Rays. *Ann. Rev. Astron. Astrophys.*, 22:425–444, 1984. doi: 10.1146/annurev.aa.22.090184.002233.

[7] D. F. Torres and L. A. Anchordoqui. Astrophysical origins of ultrahigh energy cosmic rays. *Rept. Prog. Phys.*, 67:1663–1730, 2004. doi: 10.1088/0034-4885/67/9/R03, arXiv: astro-ph/0402371.

[8] M. S. Longair. *High energy astrophysics*, volume 2. Cambridge University Press, 2. edition, 1992. ISBN 0 521 43439 4.

[9] O. Adriani, G. C. Barbarino, G. A. Bazilevskaya, et al. Cosmic-ray positron energy spectrum measured by pamela. *Phys. Rev. Lett.*, 111:081102, Aug 2013. doi: 10.1103/PhysRevLett.111.081102.

[10] Fermi LAT Collaboration Collaboration, M. Ackermann, M. Ajello, A. Allafort, et al. Measurement of separate cosmic-ray electron and positron spectra with the fermi large area telescope. *Phys. Rev. Lett.*, 108:011103, Jan 2012. doi: 10.1103/PhysRevLett.108.011103.

[11] (AMS Collaboration) Collaboration, M. Aguilar, D. Aisa, A. Alvino, et al. Electron and positron fluxes in primary cosmic rays measured with the alpha magnetic

spectrometer on the international space station. *Phys. Rev. Lett.*, 113:121102, Sep 2014. doi: 10.1103/PhysRevLett.113.121102.

[12] S. Della Torre, M. Gervasi, P. G. Rancoita, D. Rozza, and A. Treves. Pulsar Wind Nebulae as a source of the observed electron and positron excess at high energy: the case of Vela-X. *JHEAp*, 8:27–34, 2015. doi: 10.1016/j.jheap.2015.08.001, arXiv: 1508.01457.

[13] T. Delahaye, R. Lineros, F. Donato, N. Fornengo, and P. Salati. Positrons from dark matter annihilation in the galactic halo: Theoretical uncertainties. *Phys. Rev. D*, 77:063527, Mar 2008. doi: 10.1103/PhysRevD.77.063527.

[14] L. Feng, R.-Z. Yang, H.-N. He, et al. Ams-02 positron excess: New bounds on dark matter models and hint for primary electron spectrum hardening. *Physics Letters B*, 728:250 – 255, 2014. ISSN 0370-2693. doi: http://dx.doi.org/10.1016/j.physletb.2013.12.012.

[15] Particle Data Group Collaboration, K. Olive et al. Review of Particle Physics. *Chin. Phys.*, C38:090001, 2014. doi: 10.1088/1674-1137/38/9/090001.

[16] IceCube Collaboration, M. G. Aartsen et al. Characterization of the Atmospheric Muon Flux in IceCube. *Astropart. Phys.*, 78:1–27, 2016. doi: 10.1016/j.astropartphys.2016.01.006, arXiv: 1506.07981.

[17] R. Abbasi, Y. Abdou, T. Abu-Zayyad, et al. The energy spectrum of atmospheric neutrinos between 2 and 200 TeV with the AMANDA-II detector. *Astropart. Phys.*, 34:48–58, August 2010. doi: 10.1016/j.astropartphys.2010.05.001, arXiv: 1004.2357.

[18] IceCube Collaboration, M. G. Aartsen et al. Measurement of the Atmospheric ν_e Spectrum with IceCube. *Phys. Rev.*, D91:122004, 2015. doi: 10.1103/PhysRevD.91.122004, arXiv: 1504.03753.

[19] A. A. Kochanov, T. S. Sinegovskaya, and S. I. Sinegovsky. High-energy cosmic ray fluxes in the Earth atmosphere: calculations vs experiments. *Astropart. Phys.*, 30: 219–233, 2008. doi: 10.1016/j.astropartphys.2008.09.008, arXiv: 0803.2943.

[20] R. Enberg, M. H. Reno, and I. Sarcevic. Prompt neutrino fluxes from atmospheric charm. *Phys. Rev. D*, 78:043005, Aug 2008. doi: 10.1103/PhysRevD.78.043005.

[21] T. K. Gaisser. *Cosmic Rays and Particle Physics*. Cambridge University Press, 1990. ISBN 0 521 33931 6.

[22] S. P. Swordy. The Energy Spectra and Anisotropies of Cosmic Rays. *Space Sci. Rev.*, 99:85–94, October 2001.

[23] G. A. Medina-Tanco and A. A. Watson. On the possible galactic sources of the ultra-high energy cosmic ray anisotropy at 1EeV. In *Proc. of the International Cosmic Ray Conference*, volume 2, page 531, 2001.

[24] Pierre Auger Collaboration, P. Abreu, M. Aglietta, et al. A Search for Point Sources of EeV Neutrons. *Astrophys. J.*, 760:148, December 2012. doi: 10.1088/0004-637X/760/2/148, arXiv: 1211.4901.

[25] IceCube Collaboration, M. G. Aartsen et al. Search for High Energy Neutron Point Sources with IceTop. 2015, arXiv: 1510.05225.

[26] S. Wakely and D. Horan. TeVCat: An online catalog for Very High Energy Gamma-Ray Astronomy. In *Proc. of the International Cosmic Ray Conference*, volume 3, pages 1341–1344, 2007.

[27] N. Schmitz. *Neutrinophysik*. Teubner, 1997. ISBN 3-519-03236-8.

[28] W. B. Atwood, A. A. Abdo, M. Ackermann, et al. The Large Area Telescope on the Fermi Gamma-Ray Space Telescope Mission. *Astrophys. J.*, 697:1071–1102, June 2009. doi: 10.1088/0004-637X/697/2/1071, arXiv: 0902.1089.

[29] HESS Collaboration, F. Aharonian et al. Observations of the Crab Nebula with H.E.S.S. *Astron. Astrophys.*, 457:899–915, 2006. doi: 10.1051/0004-6361:20065351, arXiv: astro-ph/0607333.

[30] VERITAS Collaboration, J. Holder et al. The first VERITAS telescope. *Astropart. Phys.*, 25:391–401, 2006. doi: 10.1016/j.astropartphys.2006.04.002, arXiv: astro-ph/0604119.

[31] MAGIC Collaboration, J. Aleksić, E. A. Alvarez, L. A. Antonelli, et al. Performance of the MAGIC stereo system obtained with Crab Nebula data. *Astropart. Phys.*, 35:435–448, February 2012. doi: 10.1016/j.astropartphys.2011.11.007, arXiv: 1108.1477.

[32] VERITAS Collaboration, N. Galante. Status and highlights of VERITAS. In *American Institute of Physics Conference Series*, volume 1505 of *American Institute of Physics Conference Series*, pages 202–208, December 2012. doi: 10.1063/1.4772234.

[33] R. W. Atkins et al. TeV gamma-ray survey of the northern hemisphere sky using the Milagro Observatory. *Astrophys. J.*, 608:680–685, 2004. doi: 10.1086/420880.

[34] A. Abeysekara, R. Alfaro, C. Alvarez, et al. Sensitivity of the High Altitude Water Cherenkov Detector to Sources of Multi-TeV Gamma Rays. *Astropart.Phys.*, 50-52: 26–32, 2013. doi: 10.1016/j.astropartphys.2013.08.002, arXiv: 1306.5800.

[35] A. J. Smith and for the HAWC Collaboration. HAWC: Design, Operation, Reconstruction and Analysis. *ArXiv e-prints*, August 2015, arXiv: 1508.05826.

[36] E. Fermi. On the origin of the cosmic radiation. *Phys. Rev.*, 75:1169–1174, Apr 1949. doi: 10.1103/PhysRev.75.1169.

[37] A. Obermeier, P. Boyle, J. Hörandel, and D. Müller. The Boron-to-carbon Abundance Ratio and Galactic Propagation of Cosmic Radiation. *Astrophys. J.*, 752:69, June 2012. doi: 10.1088/0004-637X/752/1/69, arXiv: 1204.6188.

[38] Y. Butt. Beyond the myth of the supernova-remnant origin of cosmic rays. *Nature*, 460:701–704, 2009. ISSN 0028-0836. doi: 10.1038/nature08127, arXiv: 1009.3664.

[39] A. Meli, J. K. Becker, and J. J. Quenby. Ultra high energy cosmic rays: subluminal and superluminal shocks. In *Proc. of the International Cosmic Ray Conference*, May 2009.

[40] L. Sironi, U. Keshet, and M. Lemoine. Relativistic Shocks: Particle Acceleration and Magnetization. *Space Sci. Rev.*, 191(1-4):519–544, 2015. doi: 10.1007/s11214-015-0181-8, arXiv: 1506.02034.

[41] D. Giannios. UHECRs from magnetic reconnection in relativistic jets. *MNRAS*, 408:L46–L50, October 2010. doi: 10.1111/j.1745-3933.2010.00925.x, arXiv: 1007.1522.

[42] H.-T. Janka, K. Langanke, A. Marek, G. Martinez-Pinedo, and B. Mueller. Theory of Core-Collapse Supernovae. *Phys. Rept.*, 442:38–74, 2007. doi: 10.1016/j.physrep.2007.02.002, arXiv: astro-ph/0612072.

[43] G. Pagliaroli, F. Vissani, M. L. Costantini, and A. Ianni. Improved analysis of SN1987A antineutrino events. *Astropart. Phys.*, 31:163–176, 2009. doi: 10.1016/j.astropartphys.2008.12.010, arXiv: 0810.0466.

[44] D. Maoz, F. Mannucci, and G. Nelemans. Observational clues to the progenitors of type ia supernovae. *Annual Review of Astronomy and Astrophysics*, 52(1):107–170, 2014. doi: 10.1146/annurev-astro-082812-141031, arXiv: http://dx.doi.org/10.1146/annurev-astro-082812-141031.

[45] D. Branch and G. A. Tammann. Type ia supernovae as standard candles. *Annual Review of Astronomy and Astrophysics*, 30(1): 359–389, 1992. doi: 10.1146/annurev.aa.30.090192.002043, arXiv: http://dx.doi.org/10.1146/annurev.aa.30.090192.002043.

[46] Fermi Collaboration, M. Ackermann, M. Ajello, a. Allafort, et al. Detection of the characteristic pion-decay signature in supernova remnants. *Science (New York, N.Y.)*, 339(6121):807–11, February 2013. ISSN 1095-9203. doi: 10.1126/science.1231160.

[47] V. S. Beskin, S. V. Chernov, C. R. Gwinn, and A. A. Tchekhovskoy. Radio Pulsars. *Space Sci. Rev.*, 191:207–237, October 2015. doi: 10.1007/s11214-015-0173-8, arXiv: 1506.07881.

[48] M. Stix. *The Sun.* Springer-Verlag Berlin Heidelberg New York, 2. edition, 2002. ISBN 978-3-540-20741-2.

[49] R. Protheroe, W. Bednarek, and Q. Luo. Gamma-rays and neutrinos from very young supernova remnants. *Astropart. Phys.*, 9(1):1 – 14, 1998. ISSN 0927-6505. doi: http://dx.doi.org/10.1016/S0927-6505(98)00014-0.

[50] P. Goldreich and W. H. Julian. Pulsar Electrodynamics. *Astrophys. J.*, 157:869, August 1969. doi: 10.1086/150119.

[51] R. Bühler and R. Blandford. The surprising Crab pulsar and its nebula: A review. *Rept. Prog. Phys.*, 77:066901, 2014. doi: 10.1088/0034-4885/77/6/066901, arXiv: 1309.7046.

[52] O. Kargaltsev, B. Cerutti, Y. Lyubarsky, and E. Striani. Pulsar-Wind Nebulae: Recent Progress in Observations and Theory. *Space Sci. Rev.*, 191(1-4):391–439, 2015. doi: 10.1007/s11214-015-0171-x, arXiv: 1507.03662.

[53] A. Weinstein. Pulsar Wind Nebulae and Cosmic Rays: A Bedtime Story. *Nuclear Physics B Proceedings Supplements*, 256:136–148, November 2014. doi: 10.1016/j.nuclphysbps.2014.10.017, arXiv: 1411.2532.

[54] O. Porth, S. S. Komissarov, and R. Keppens. Three-Dimensional Magnetohydrodynamic Simulations of the Crab Nebula. *Mon. Not. Roy. Astron. Soc.*, 438(1): 278–306, 2014. doi: 10.1093/mnras/stt2176, arXiv: 1310.2531.

[55] W. Bednarek, J. Pabich, and T. Sobczak. Gamma-rays and neutrinos from dense environment of massive binary systems in open clusters. *Phys. Rev.*, D90(10):103008, 2014. doi: 10.1103/PhysRevD.90.103008, arXiv: 1410.7553.

[56] G. Dubus. Gamma-ray binaries and related systems. *Astron. Astrophys. Rev.*, 21: 64, 2013. doi: 10.1007/s00159-013-0064-5, arXiv: 1307.7083.

[57] Y. N. Istomin. On the origin of galactic cosmic rays. *New Astronomy*, 27:13–18, February 2014. doi: 10.1016/j.newast.2013.08.001, arXiv: 1110.5436.

[58] M. Su, T. R. Slatyer, and D. P. Finkbeiner. Giant Gamma-ray Bubbles from Fermi-LAT: Active Galactic Nucleus Activity or Bipolar Galactic Wind? *Astrophys. J.*, 724:1044–1082, December 2010. doi: 10.1088/0004-637X/724/2/1044, arXiv: 1005.5480.

[59] N. E. Yanasak, M. E. Wiedenbeck, R. A. Mewaldt, et al. Measurement of the secondary radionuclides 10be, 26al, 36cl, 54mn, and 14c and implications for the galactic cosmic-ray age. *Astrophys. J.*, 563(2):768, 2001. URL http://stacks.iop.org/0004-637X/563/i=2/a=768.

[60] P. Lipari. The lifetime of cosmic rays in the Milky Way. *ArXiv e-prints*, July 2014, arXiv: 1407.5223.

[61] C. M. Urry and P. Padovani. Unified schemes for radio-loud active galactic nuclei. *Publ. Astron. Soc. Pac.*, 107:803, 1995. doi: 10.1086/133630, arXiv: astro-ph/9506063.

[62] P. Kumar and B. Zhang. The physics of gamma-ray bursts & relativistic jets. *Phys. Rept.*, 561:1–109, 2014. doi: 10.1016/j.physrep.2014.09.008, arXiv: 1410.0679.

[63] E. Berger. Short-Duration Gamma-Ray Bursts. In Faber, SM and Van-Dishoeck, E, editor, *ANNUAL REVIEW OF ASTRONOMY AND ASTRO-PHYSICS, VOL 52*, volume 52 of *Annual Review of Astronomy and Astrophysics*, pages 43–105. ANNUAL REVIEWS, 4139 EL CAMINO WAY, PO BOX 10139, PALO ALTO, CA 94303-0897 USA, 2014. ISBN 978-0-8243-0952-7. doi: 10.1146/annurev-astro-081913-035926.

[64] HESS Collaboration, S. Carrigan, F. Brun, R. C. G. Chaves, et al. The H.E.S.S. Galactic Plane Survey - maps, source catalog and source population. In *Proceedings, 33rd International Cosmic Ray Conference (ICRC2013)*, 2013. URL http://inspirehep.net/record/1243126/files/arXiv:1307.4690.pdf.

[65] A. A. Abdo, B. Allen, D. Berley, et al. Tev gamma-ray sources from a survey of the galactic plane with milagro. *Astrophys. J. L.*, 664(2):L91, 2007. URL http://stacks.iop.org/1538-4357/664/i=2/a=L91.

[66] M. Ackermann, M. Ajello, W. B. Atwood, et al. Fermi-LAT Observations of the Diffuse γ-Ray Emission: Implications for Cosmic Rays and the Interstellar Medium. *Astrophysical Journal*, 750:3, May 2012. doi: 10.1088/0004-637X/750/1/3, arXiv: 1202.4039.

[67] HESS Collaboration, A. Abramowski et al. Diffuse Galactic gamma-ray emission with H.E.S.S. *Phys.Rev.*, D90(12):122007, 2014. doi: 10.1103/PhysRevD.90.122007, arXiv: 1411.7568.

[68] R. Buehler. Status of space-based gamma-ray astronomy. *PoS*, ICRC2015:017, 2015, arXiv: 1509.00012.

[69] Q. Yuan, S. Liu, and X. Bi. An Attempt at a Unified Model for the Gamma-Ray Emission of Supernova Remnants. *Astrophys. J.*, 761:133, December 2012. doi: 10.1088/0004-637X/761/2/133, arXiv: 1203.0085.

[70] A. A. Abdo, M. Ackermann, M. Ajello, et al. Fermi LAT Discovery of Extended Gamma-Ray Emission in the Direction of Supernova Remnant W51C. *Astrophys. J. L.*, 706:L1–L6, November 2009. doi: 10.1088/0004-637X/706/1/L1, arXiv: 0910.0908.

[71] T. C. Weekes, M. F. Cawley, D. J. Fegan, et al. Observation of TeV gamma rays from the Crab nebula using the atmospheric Cerenkov imaging technique. *Astrophys. J.*, 342:379–395, July 1989. doi: 10.1086/167599.

[72] MAGIC Collaboration, J. Aleksić, S. Ansoldi, L. A. Antonelli, et al. Measurement of the Crab Nebula spectrum over three decades in energy with the MAGIC telescopes. *Journal of High Energy Astrophysics*, 5:30–38, March 2015. doi: 10.1016/j.jheap.2015.01.002, arXiv: 1406.6892.

[73] D. F. Torres, J. Martin, E. d. O. Wilhelmi, and A. Cillis. The effects of magnetic field, age, and intrinsic luminosity on Crab-like pulsar wind nebulae. *Mon. Not. Roy. Astron. Soc.*, 436:3112, 2013. doi: 10.1093/mnras/stt1793, arXiv: 1309.5291.

[74] D. F. Torres, A. Cillis, J. Martín, and E. de Oña Wilhelmi. Time-dependent modeling of TeV-detected, young pulsar wind nebulae. *JHEAp*, 1-2:31–62, 2014. doi: 10.1016/j.jheap.2014.02.001, arXiv: 1402.5485.

[75] A. A. Abdo, M. Ackermann, M. Ajello, et al. Observations of the Young Supernova Remnant RX J1713.7-3946 with the Fermi Large Area Telescope. *Astrophys. J.*, 734(1):28, 2011. URL http://stacks.iop.org/0004-637X/734/i=1/a=28.

[76] D. C. Ellison, D. J. Patnaude, P. Slane, and J. Raymond. Efficient Cosmic Ray Acceleration, Hydrodynamics, and Self-Consistent Thermal X-Ray Emission Applied to Supernova Remnant RX J1713.7-3946. *Astrophys. J.*, 712:287–293, March 2010. doi: 10.1088/0004-637X/712/1/287, arXiv: 1001.1932.

[77] B. Katz and E. Waxman. In which shell-type SNRs should we look for gamma-rays and neutrinos from p-p collisions? *JCAP*, 0801:018, 2008. doi: 10.1088/1475-7516/2008/01/018, arXiv: 0706.3485.

[78] S. Federici, M. Pohl, I. Telezhinsky, A. Wilhelm, and V. V. Dwarkadas. Analysis of GeV-band γ-ray emission from supernova remnant RX J1713.7-3946. *Astron. Astrophys.*, 577:A12, 2015. doi: 10.1051/0004-6361/201424947, arXiv: 1502.06355.

[79] T. Inoue, R. Yamazaki, S. ichiro Inutsuka, and Y. Fukui. Toward understanding the cosmic-ray acceleration at young supernova remnants interacting with interstellar clouds: Possible applications to rx j1713.7-3946. *Astrophys. J.*, 744(1):71, 2012. URL http://stacks.iop.org/0004-637X/744/i=1/a=71.

[80] S. Gabici and F. A. Aharonian. Gamma-ray emission from young supernova remnants: hadronic or leptonic? *ArXiv e-prints*, February 2015, arXiv: 1502.00644.

[81] HESS Collaboration, : et al. Acceleration of petaelectronvolt protons in the Galactic Centre. *Nature*, 531:476, 2016. doi: 10.1038/nature17147, arXiv: 1603.07730.

[82] M. Boettcher, A. Reimer, K. Sweeney, and A. Prakash. Leptonic and Hadronic Modeling of Fermi-Detected Blazars. *Astrophys. J.*, 768:54, 2013. doi: 10.1088/0004-637X/768/1/54, arXiv: 1304.0605.

[83] V. S. Paliya, C. Diltz, M. Bottcher, C. S. Stalin, and D. Buckley. A hard gamma-ray flare from 3C 279 in 2013 December. 2015, arXiv: 1512.00203.

[84] T. M. Venters. Contribution to the Extragalactic Gamma-Ray Background from the Cascades of very High Energy Gamma Rays from Blazars. *Astrophys. J.*, 710:1530–1540, February 2010. doi: 10.1088/0004-637X/710/2/1530, arXiv: 1001.1363.

[85] F. W. Stecker, O. C. de Jager, and M. H. Salamon. TeV gamma rays from 3C 279 - A possible probe of origin and intergalactic infrared radiation fields. *Astrophys. J.*, 390:L49, 1992. doi: 10.1086/186369.

[86] K. Murase, D. Guetta, and M. Ahlers. Hidden Cosmic-Ray Accelerators as an Origin of TeV-PeV Cosmic Neutrinos. 2015, arXiv: 1509.00805.

[87] J. K. Becker. High-energy neutrinos in the context of multimessenger physics. *Phys. Rept.*, 458:173–246, 2008. doi: 10.1016/j.physrep.2007.10.006, arXiv: 0710.1557.

[88] S. R. Kelner, F. A. Aharonian, and V. V. Bugayov. Energy spectra of gamma-rays, electrons and neutrinos produced at proton-proton interactions in the very high energy regime. *Phys. Rev.*, D74:034018, 2006. doi: 10.1103/PhysRevD.74.034018, 10.1103/PhysRevD.79.039901, arXiv: astro-ph/0606058. [Erratum: Phys. Rev.D79,039901(2009)].

[89] IceCube Collaboration, M. Aartsen et al. Evidence for High-Energy Extraterrestrial Neutrinos at the IceCube Detector. *Science*, 342:1242856, 2013. doi: 10.1126/science.1242856, arXiv: 1311.5238.

[90] IceCube Collaboration, M. Aartsen et al. Observation of High-Energy Astrophysical Neutrinos in Three Years of IceCube Data. *Phys.Rev.Lett.*, 113:101101, 2014. doi: 10.1103/PhysRevLett.113.101101, arXiv: 1405.5303.

[91] IceCube Collaboration, M. G. Aartsen et al. Evidence for Astrophysical Muon Neutrinos from the Northern Sky with IceCube. *Phys. Rev. Lett.*, 115(8):081102, 2015. doi: 10.1103/PhysRevLett.115.081102, arXiv: 1507.04005.

[92] IceCube Collaboration, M. G. Aartsen et al. A combined maximum-likelihood analysis of the high-energy astrophysical neutrino flux measured with IceCube. *Astrophys. J.*, 809(1):98, 2015. doi: 10.1088/0004-637X/809/1/98, arXiv: 1507.03991.

[93] Q. Yuan, P.-F. Yin, and X.-J. Bi. Neutrino emission of Fermi supernova remnants. *Astropart. Phys.*, 35:33–38, August 2011. doi: 10.1016/j.astropartphys.2011.03.004, arXiv: 1010.1901.

[94] D. Fox, K. Kashiyama, and P. Mészarós. Sub-PeV Neutrinos from TeV Unidentified Sources in the Galaxy. *Astrophys.J.*, 774:74, 2013. doi: 10.1088/0004-637X/774/1/74, arXiv: 1305.6606.

[95] L. A. Anchordoqui, H. Goldberg, T. C. Paul, L. H. M. da Silva, and B. J. Vlcek. Estimating the contribution of Galactic sources to the diffuse neutrino flux. *Phys.Rev.*, D90(12):123010, 2014. doi: 10.1103/PhysRevD.90.123010, arXiv: 1410.0348.

[96] W. Bednarek. Neutrinos from the pulsar wind nebulae. *Astron.Astrophys.*, 407: 1–6, 2003. doi: 10.1051/0004-6361:20030929, arXiv: astro-ph/0305430.

[97] A. Kappes, J. Hinton, C. Stegmann, and F. A. Aharonian. Potential neutrino signals from galactic gamma-ray sources. *Astrophys. J.*, 656(2):870, 2007. URL http://stacks.iop.org/0004-637X/656/i=2/a=870.

[98] T. K. Gaisser and T. Stanev. Neutrinos and cosmic rays. *Astropart. Phys.*, 39-40:120–128, December 2012. ISSN 09276505. doi: 10.1016/j.astropartphys.2012.08.004.

[99] D. Gaggero, D. Grasso, A. Marinelli, A. Urbano, and M. Valli. The gamma-ray and neutrino sky: a consistent picture of Fermi-LAT, H.E.S.S., Milagro, and IceCube results. 2015, arXiv: 1504.00227.

[100] X.-Y. Wang, S. Razzaque, P. Mészáros, and Z.-G. Dai. High-energy cosmic rays and neutrinos from semirelativistic hypernovae. *Phys. Rev. D*, 76:083009, Oct 2007. doi: 10.1103/PhysRevD.76.083009.

[101] G. Bertone, D. Hooper, and J. Silk. Particle dark matter: Evidence, candidates and constraints. *Phys. Rept.*, 405:279–390, 2005. doi: 10.1016/j.physrep.2004.08.031, arXiv: hep-ph/0404175.

[102] R. Allahverdi, S. Campbell, and B. Dutta. Extragalactic and galactic gamma-rays and neutrinos from annihilating dark matter. *Phys.Rev.*, D85:035004, 2012. doi: 10.1103/PhysRevD.85.035004, arXiv: 1110.6660.

[103] R. Abbasi, Y. Abdou, T. Abu-Zayyad, et al. An absence of neutrinos associated with cosmic-ray acceleration in γ-ray bursts. *Nature*, 484:351–354, April 2012. doi: 10.1038/nature11068, arXiv: 1204.4219.

[104] F. W. Stecker, C. Done, M. H. Salamon, and P. Sommers. High-energy neutrinos from active galactic nuclei. *Phys. Rev. Lett.*, 66:2697–2700, May 1991. doi: 10.1103/PhysRevLett.66.2697.

[105] K. Mannheim and P. L. Biermann. Photomeson production in active galactic nuclei. *Astronomy and Astrophyisics*, 221:211–220, September 1989.

[106] K. Mannheim. High-energy neutrinos from extragalactic jets. *Astropart. Phys.*, 3(3):295 – 302, 1995. ISSN 0927-6505. doi: http://dx.doi.org/10.1016/0927-6505(94)00044-4.

[107] K. Schatto. *Stacked searches for high-energy neutrinos from blazars with Ice-Cube*. PhD thesis, Johannes Gutenberg-Universität Mainz, 2014.

[108] IceCube Collaboration, T. Glüsenkamp. Analysis of the cumulative neutrino flux from Fermi-LAT blazar populations using 3 years of IceCube data. In *5th Roma*

International Conference on Astro-Particle physics (RICAP 14) Noto, Sicily, Italy, September 30-October 3, 2014, 2015. URL `http://inspirehep.net/record/1343949/files/arXiv:1502.03104.pdf`.

[109] A. Loeb and E. Waxman. The Cumulative background of high energy neutrinos from starburst galaxies. *JCAP*, 0605:003, 2006. doi: 10.1088/1475-7516/2006/05/003, arXiv: astro-ph/0601695.

[110] K. Murase. On the origin of high-energy cosmic neutrinos. In *American Institute of Physics Conference Series*, volume 1666 of *American Institute of Physics Conference Series*, page 040006, July 2015. doi: 10.1063/1.4915555.

[111] K. Greisen. End to the Cosmic-Ray Spectrum? *Physical Review Letters*, 16:748–750, April 1966. doi: 10.1103/PhysRevLett.16.748.

[112] G. T. Zatsepin and V. A. Kuz'min. Upper Limit of the Spectrum of Cosmic Rays. *Soviet Journal of Experimental and Theoretical Physics Letters*, 4:78–+, August 1966.

[113] D. Hooper, A. Taylor, and S. Sarkar. The impact of heavy nuclei on the cosmogenic neutrino flux. *Astropart. Phys.*, 23:11–17, 2005. doi: 10.1016/j.astropartphys.2004.11.002, arXiv: astro-ph/0407618.

[114] J. A. Formaggio and G. P. Zeller. From eV to EeV: Neutrino Cross Sections Across Energy Scales. *Rev. Mod. Phys.*, 84:1307, 2012. doi: 10.1103/RevModPhys.84.1307, arXiv: 1305.7513.

[115] R. Gandhi, C. Quigg, M. H. Reno, and I. Sarcevic. Ultrahigh-energy neutrino interactions. *Astropart.Phys.*, 5:81–110, 1996. doi: 10.1016/0927-6505(96)00008-4, arXiv: hep-ph/9512364.

[116] A. Cooper-Sarkar, P. Mertsch, and S. Sarkar. Quantifying uncertainties in the high energy neutrino cross-section. In *Proceedings, 32nd International Cosmic Ray Conference (ICRC 2011)*, 2011. doi: 10.1007/s12043-012-0452-9. [Pramana79,1301(2012)].

[117] S. Pakvasa. Neutrino Flavor Detection at Neutrino Telescopes and Its Uses. In *CTP International Conference on Neutrino Physics in the LHC Era*, 2009. URL `http://inspirehep.net/record/853649/files/arXiv:1004.5413.pdf`.

[118] S. Hümmer, M. Maltoni, W. Winter, and C. Yaguna. Energy dependent neutrino flavor ratios from cosmic accelerators on the Hillas plot. *Astropart. Phys.*, 34:205–224, November 2010. doi: 10.1016/j.astropartphys.2010.07.003, arXiv: 1007.0006.

[119] P. A. Čerenkov. Visible radiation produced by electrons moving in a medium with velocities exceeding that of light. *Phys. Rev.*, 52:378–379, Aug 1937. doi: 10.1103/PhysRev.52.378.

[120] D. H. Perkins. *Introduction to High Energy Physics*. Cambridge University Press, 4. edition, 2000. ISBN 0521621968.

[121] S. W. Smith. The refractive index of liquids for x-rays. *Phys. Rev.*, 40:156–164, Apr 1932. doi: 10.1103/PhysRev.40.156.

[122] D. E. Groom, N. V. Mokhov, and S. I. Striganov. Muon stopping power and range tables 10 mev–100 tev. *Atomic Data and Nuclear Data Tables*, 78(2):183 – 356, 2001. ISSN 0092-640X. doi: http://dx.doi.org/10.1006/adnd.2001.0861.

[123] S. I. Klimushin, E. V. Bugaev, and I. A. Sokalski. Precise parametrizations of muon energy losses in water. In *27th International Cosmic Ray Conference (ICRC 2001) Hamburg, Germany, August 7-15, 2001*, page 1009, 2001. URL http://alice.cern.ch/format/showfull?sysnb=2258285. [3,1009(2001)].

[124] C. H. V. Wiebusch. *The Detection of faint light in deep underwater neutrino telescopes*. PhD thesis, DESY, Zeuthen, 1995. URL http://www-zeuthen.desy.de//amanda_users/nuastro/publications/phd/wiebusch.ps.gz.

[125] B. Voigt. *Sensitivity of the IceCube Detector for Ultra-High Energy Electron-Neutrino Events*. PhD thesis, Humboldt-Universität zu Berlin, July 2008.

[126] IceCube Collaboration, M. Aartsen et al. Energy Reconstruction Methods in the IceCube Neutrino Telescope. *JINST*, 9:P03009, 2014. doi: 10.1088/1748-0221/9/03/P03009, arXiv: 1311.4767.

[127] J. G. Learned and S. Pakvasa. Detecting tau-neutrino oscillations at PeV energies. *Astropart.Phys.*, 3:267–274, 1995. doi: 10.1016/0927-6505(94)00043-3, arXiv: hep-ph/9405296.

[128] D. Chirkin and W. Rhode. Propagating leptons through matter with Muon Monte Carlo (MMC). *ArXiv High Energy Physics - Phenomenology e-prints*, July 2004, arXiv: hep-ph/0407075.

[129] L. Rädel and C. Wiebusch. Calculation of the Cherenkov light yield from electromagnetic cascades in ice with Geant4. *Astropart. Phys.*, 44:102–113, April 2013. doi: 10.1016/j.astropartphys.2013.01.015, arXiv: 1210.5140.

[130] F. Halzen. Astropart. Phys. physics with high energy neutrinos: from amanda to icecube. *Eur.Phys.J.*, C46:669–687, 2006. doi: 10.1140/epjc/s2006-02536-4, arXiv: astro-ph/0602132.

[131] D. M. Lowder, T. Miller, P. B. Price, et al. Observation of muons using the polar ice cap as a Cherenkov detector. *Nature*, 353:331–333, 1991. doi: 10.1038/353331a0.

[132] M. Ageron, J. A. Aguilar, I. Al Samarai, et al. ANTARES: The first undersea neutrino telescope. *Nuclear Instruments and Methods in Physics Research A*, 656:11–38, November 2011. doi: 10.1016/j.nima.2011.06.103, arXiv: 1104.1607.

[133] C. Spiering. Towards high-energy neutrino astronomy. A historical review. *European Physical Journal H*, 37:515–565, August 2012. doi: 10.1140/epjh/e2012-30014-2, arXiv: 1207.4952.

[134] DUMAND Collaboration Collaboration, J. Babson et al. Cosmic-ray muons in the deep ocean. *Phys. Rev. D*, 42(11):3613–3620, Dec 1990. doi: 10.1103/PhysRevD.42.3613.

[135] G. Giacomelli. Results from the ANTARES neutrino telescope. 2011, arXiv: 1105.1245.

[136] A. Margiotta. The KM3NeT deep-sea neutrino telescope. *Nuclear Instruments and Methods in Physics Research A*, 766:83–87, December 2014. doi: 10.1016/j.nima.2014.05.090, arXiv: 1408.1392.

[137] KM3Net Collaboration, S. Adrian-Martinez et al. Letter of Intent for KM3NeT2.0. 2016, arXiv: 1601.07459.

[138] C. Spiering. Towards high-energy neutrino astronomy. A historical review. *European Physical Journal H*, 37:515–565, August 2012. doi: 10.1140/epjh/e2012-30014-2, arXiv: 1207.4952.

[139] A. D. Avrorin, A. V. Avrorin, V. M. Aynutdinov, et al. The prototyping/early construction phase of the BAIKAL-GVD project. *Nuclear Instruments and Methods in Physics Research A*, 742:82–88, April 2014. doi: 10.1016/j.nima.2013.10.064, arXiv: 1308.1833.

[140] E. Andres et al. The AMANDA neutrino telescope: Principle of operation and first results. *Astropart. Phys.*, 13:1–20, 2000. doi: 10.1016/S0927-6505(99)00092-4, arXiv: astro-ph/9906203.

[141] R. Wischnewski. The AMANDA-II neutrino telescope. *Nuclear Physics B Proceedings Supplements*, 110:510–512, July 2002. doi: 10.1016/S0920-5632(02)01550-5, arXiv: astro-ph/0204268.

[142] IceCube Collaboration, R. Abbasi, M. Ackermann, J. Adams, et al. The IceCube data acquisition system: Signal capture, digitization, and timestamping. *Nuclear Instruments and Methods in Physics Research Section A: Accelerators, Spectrometers, Detectors and Associated Equipment*, 601(3):294–316, April 2009. ISSN 01689002. doi: 10.1016/j.nima.2009.01.001.

[143] IceCube Collaboration, A. Achterberg et al. First year performance of the icecube neutrino telescope. *Astropart.Phys.*, 26(3):155 – 173, 2006. ISSN 0927-6505. doi: http://dx.doi.org/10.1016/j.astropartphys.2006.06.007.

[144] J. Yang. labeled .jpg image of icecube array with amanda, 2012. URL https://gallery.icecube.wisc.edu/internal/d/298923-2/ArrayWSeasonsLabelsAmanda.jpg.

[145] IceCube Collaboration, S. R. Klein. IceCube: A Cubic Kilometer Radiation Detector. *IEEE Transactions on Nuclear Science*, 56:1141–1147, June 2009. doi: 10.1109/TNS.2009.2015300, arXiv: 0807.0034.

[146] IceCube Collaboration, R. Abbasi, Y. Abdou, T. Abu-Zayyad, et al. Calibration and characterization of the IceCube photomultiplier tube. *Nuclear Instruments and Methods in Physics Research A*, 618:139–152, June 2010. doi: 10.1016/j.nima.2010.03.102, arXiv: 1002.2442.

[147] M. Ackermann et al. Optical properties of deep glacial ice at the South Pole. *Journal of Geophysical Research (Atmospheres)*, 111(D10):D13203, July 2006. doi: 10.1029/2005JD006687.

[148] IceCube Collaboration, M. G. Aartsen et al. Measurement of South Pole ice transparency with the IceCube LED calibration system. *Nucl. Instrum. Meth.*, A711: 73–89, 2013. doi: 10.1016/j.nima.2013.01.054, arXiv: 1301.5361.

[149] IceCube Collaboration, M. G. Aartsen et al. Searches for Extended and Point-like Neutrino Sources with Four Years of IceCube Data. *Astrophys. J.*, 796(2):109, 2014. doi: 10.1088/0004-637X/796/2/109, arXiv: 1406.6757.

[150] IceCube Collaboration, S. Tilav, P. Desiati, T. Kuwabara, et al. Atmospheric Variations as Observed by IceCube. In *Proceedings, 31st International Cosmic Ray Conference (ICRC 2009)*, 2010. URL http://inspirehep.net/record/841872/files/arXiv:1001.0776.pdf.

[151] N. Whitehorn. *A Search for High-Energy Neutrino Emission from Gamma-Ray Bursts*. PhD thesis, UNIVERSITY OF WISCONSIN–MADISON, 2012.

[152] A. Gazizov and M. Kowalski. Anis: High energy neutrino generator for neutrino telescopes. *Computer Physics Communications*, 172(3):203 – 213, 2005. ISSN 0010-4655. doi: http://dx.doi.org/10.1016/j.cpc.2005.03.113.

[153] D. Heck and T. Pierog. *Extensive Air Shower Simulation with CORSIKA: A User's Guide*. Institut für Kernphysik / Forschungszentrum Karlsruhe, corsika 6.99x edition, August 2011.

[154] J. H. Koehne, K. Frantzen, M. Schmitz, et al. PROPOSAL: A tool for propagation of charged leptons. *Computer Physics Communications*, 184(9):2070–2090, 2013. ISSN 00104655. doi: 10.1016/j.cpc.2013.04.001.

[155] IceCube Collaboration, D. Chirkin. Evidence of optical anisotropy of the South Pole ice. In *Proceedings, 33rd International Cosmic Ray Conference (ICRC2013): Rio de Janeiro, Brazil, July 2-9, 2013*, page 0580, 2013. URL http://www.cbpf.br/%7Eicrc2013/papers/icrc2013-0580.pdf.

[156] K. Copper. An OpenCL-based photon-tracking simulation using a (source-based) ray tracing algorithm modeling scattering and absorption of light in the deep glacial ice at the South Pole or Mediterranean sea water. URL `https://github.com/claudiok/clsim`. Accessed on March 22nd 2016.

[157] J. Lundberg et al. Light tracking for glaciers and oceans: Scattering and absorption in heterogeneous media with photonics. *Nucl. Instrum. Meth.*, A581:619–631, 2007. doi: 10.1016/j.nima.2007.07.143, arXiv: astro-ph/0702108.

[158] IceCube Collaboration, M. G. Aartsen et al. Search for Time-independent Neutrino Emission from Astrophysical Sources with 3 yr of IceCube Data. *Astrophys. J.*, 779:132, 2013. doi: 10.1088/0004-637X/779/2/132, arXiv: 1307.6669.

[159] ANTARES Collaboration, S. Adrian-Martinez et al. Searches for Point-like and extended neutrino sources close to the Galactic Centre using the ANTARES neutrino Telescope. *Astrophys.J.*, 786:L5, 2014. doi: 10.1088/2041-8205/786/1/L5, arXiv: 1402.6182.

[160] S. Schonert, T. K. Gaisser, E. Resconi, and O. Schulz. Vetoing atmospheric neutrinos in a high energy neutrino telescope. *Phys.Rev.*, D79:043009, 2009. doi: 10.1103/PhysRevD.79.043009, arXiv: 0812.4308.

[161] T. K. Gaisser, K. Jero, A. Karle, and J. van Santen. Generalized self-veto probability for atmospheric neutrinos. *Phys.Rev.*, D90(2):023009, 2014. doi: 10.1103/PhysRevD.90.023009, arXiv: 1405.0525.

[162] ANTARES Collaboration, S. Adrian-Martinez et al. Search for Cosmic Neutrino Point Sources with Four Year Data of the ANTARES Telescope. *Astrophys.J.*, 760: 53, 2012. doi: 10.1088/0004-637X/760/1/53, arXiv: 1207.3105.

[163] IceCube Collaboration, M. G. Aartsen et al. Search for neutrino-induced particle showers with IceCube-40. *Phys. Rev.*, D89(10):102001, 2014. doi: 10.1103/PhysRevD.89.102001, arXiv: 1312.0104.

[164] IceCube Collaboration, M. G. Aartsen et al. Determining neutrino oscillation parameters from atmospheric muon neutrino disappearance with three years of IceCube DeepCore data. *Phys. Rev.*, D91(7):072004, 2015. doi: 10.1103/PhysRevD.91.072004, arXiv: 1410.7227.

[165] J. Feintzeig. *Searches for Point-like Sources of Astrophysical Neutrinos with the IceCube Neutrino Observatory*. PhD thesis, University of Wisconsin, Madison, 2014.

[166] IceCube Collaboration, M. Aartsen et al. Low-energy (100 GeV - few TeV) neutrino point source searches in the Southern sky with IceCube . In *PoS(ICRC2015)1053*, 2015.

124

[167] R. Ström. *Exploring the Universe Using Neutrinos: A Search for Point Sources in the Southern Hemisphere Using the IceCube Neutrino Observatory.* PhD thesis, Uppsala University, 2015. URL http://urn.kb.se/resolve?urn=urn:nbn:se:uu:diva-265522.

[168] AMANDA Collaboration, J. Ahrens et al. Muon Track Reconstruction and Data Selection Techniques in AMANDA. *Nucl. Instrum. Meth.*, A524:169–194, 2004. doi: 10.1016/j.nima.2004.01.065, arXiv: astro-ph/0407044.

[169] M. G. Aartsen, R. Abbasi, Y. Abdou, et al. Improvement in fast particle track reconstruction with robust statistics. *Nuclear Instruments and Methods in Physics Research A*, 736:143–149, February 2014. doi: 10.1016/j.nima.2013.10.074, arXiv: 1308.5501.

[170] D. Pandel. Bestimmung von Wasser- und Detektorparametern und Rekonstruktion von Myonen bis 100 TeV mit dem Baikal-Neutrinoteleskop NT-72. Master's thesis, Humboldt-Universität zu Berlin, 1996.

[171] N. Whitehorn, J. van Santen, and S. Lafebre. Penalized Splines for Smooth Representation of High-dimensional Monte Carlo Datasets. *Comput.Phys.Commun.*, 184:2214–2220, 2013. doi: 10.1016/j.cpc.2013.04.008, arXiv: 1301.2184.

[172] T. Neunhöffer. Estimating the angular resolution of tracks in neutrino telescopes based on a likelihood analysis. *Astropart. Phys.*, 25(February 2008):220–225, 2006. ISSN 09276505. doi: 10.1016/j.astropartphys.2006.01.002, arXiv: 0403367.

[173] S. Odrowski. *High-Energy Neutrino Scan of the Galactic Plane.* PhD thesis, Ruperto-Carola-University of Heidelberg, 2012. URL http://www.ub.uni-heidelberg.de/archiv/13216.

[174] IceCube Collaboration, T. Glüsenkamp. Studies on the true resolution versus the estimated resolution of muon tracks. Internal report icecube/201509002, 2015. URL http://internal.icecube.wisc.edu/reports/data/icecube/2015/09/002/icecube_201509002_v1.pdf.

[175] IceCube Collaboration, M. G. Aartsen et al. Observation of the cosmic-ray shadow of the Moon with IceCube. *Phys. Rev.*, D89(10):102004, 2014. doi: 10.1103/PhysRevD.89.102004, arXiv: 1305.6811.

[176] S. Euler. *Observation of oscillations of atmospheric neutrinos with the IceCube Neutrino Observatory.* PhD thesis, RWTH Aachen, 2014.

[177] IceCube Collaboration. Very high energy electromagnetic cascades in the LPM regime with IceCube. In *Proceedings, 30th International Cosmic Ray Conference (ICRC 2007)*, 2007. URL http://inspirehep.net/record/766535/files/arXiv:0711.0353.pdf.

[178] L. D. Landau and I. Pomeranchuk. Electron cascade process at very high-energies. *Dokl. Akad. Nauk Ser. Fiz.*, 92:735–738, 1953.

[179] L. D. Landau and I. Pomeranchuk. Limits of applicability of the theory of bremsstrahlung electrons and pair production at high-energies. *Dokl. Akad. Nauk Ser. Fiz.*, 92:535–536, 1953.

[180] A. B. Migdal. Bremsstrahlung and pair production in condensed media at high-energies. *Phys. Rev.*, 103:1811–1820, 1956. doi: 10.1103/PhysRev.103.1811.

[181] D. Chirkin. Topological Splitter algorithm. URL http://code.icecube.wisc.edu/svn/projects/TopologicalSplitter. Unpublished SVN directory, accessed on March 17th 2016.

[182] IceCube Collaboration, M. G. Aartsen et al. Search for Time-independent Neutrino Emission from Astrophysical Sources with 3 yr of IceCube Data. *Astrophys. J.*, 779:132, 2013. doi: 10.1088/0004-637X/779/2/132, arXiv: 1307.6669.

[183] M. Richman. *A Search for Muon Neutrinos coincident with Northern Gamma-Ray Bursts using IceCube.* PhD thesis, Univeristy of Maryland, 2015.

[184] A. Hoecker, P. Speckmayer, J. Stelzer, et al. *TMVA - Toolkit for Multivariate Data Analysis*, March 2007.

[185] P. Flach. *Machine Learning: The Art and Science of Algorithms that Make Sense of Data.* Cambridge University Press, 2012. ISBN 9781107096394.

[186] IceCube Collaboration, M. Aartsen et al. Atmospheric and astrophysical neutrinos above 1 TeV interacting in IceCube. *Phys.Rev.*, D91(2):022001, 2015. doi: 10.1103/PhysRevD.91.022001, arXiv: 1410.1749.

[187] W. Feller. On the kolmogorov-smirnov limit theorems for empirical distributions. *Ann. Math. Statist.*, 19(2):177–189, 06 1948. doi: 10.1214/aoms/1177730243.

[188] IceCube Collaboration, M. G. Aartsen et al. The IceCube Neutrino Observatory - Contributions to ICRC 2015 Part II: Atmospheric and Astrophysical Diffuse Neutrino Searches of All Flavors. In *Proceedings, 34th International Cosmic Ray Conference (ICRC 2015)*, 2015. URL http://inspirehep.net/record/1398539/files/arXiv:1510.05223.pdf.

[189] J. Braun, J. Dumm, F. De Palma, et al. Methods for point source analysis in high energy neutrino telescopes. *Astropart.Phys.*, 29:299–305, 2008. doi: 10.1016/j.astropartphys.2008.02.007, arXiv: 0801.1604.

[190] J. Neyman. Outline of a theory of statistical estimation based on the classical theory of probability. *Philosophical Transactions of the Royal Society of London A: Mathematical, Physical and Engineering Sciences*, 236(767):333–380, 1937. ISSN 0080-4614. doi: 10.1098/rsta.1937.0005.

[191] S. S. Wilks. The large-sample distribution of the likelihood ratio for testing composite hypotheses. *Ann. Math. Statist.*, 9(1):60–62, 03 1938. doi: 10.1214/aoms/1177732360.

[192] T. Glüsenkamp. *Search for a cumulative neutrino flux from 2LAC-blazar populations using 3 years of IceCube data.* PhD thesis, Humboldt-Universität zu Berlin, 2016.

[193] M. Richman. private communication, 2015.

[194] K. M. Górski, E. Hivon, A. J. Banday, et al. HEALPix: A Framework for High-Resolution Discretization and Fast Analysis of Data Distributed on the Sphere. *Astrophys. J.*, 622:759–771, April 2005. doi: 10.1086/427976, arXiv: astro-ph/0409513.

[195] IceCube, ANTARES Collaboration, S. Adrian-Martinez et al. The First Combined Search for Neutrino Point-sources in the Southern Hemisphere With the Antares and Icecube Neutrino Telescopes. *Astrophys. J.*, 823(1):65, 2016. doi: 10.3847/0004-637X/823/1/65, arXiv: 1511.02149.

[196] G. J. Feldman and R. D. Cousins. A Unified approach to the classical statistical analysis of small signals. *Phys. Rev.*, D57:3873–3889, 1998. doi: 10.1103/PhysRevD.57.3873, arXiv: physics/9711021.

[197] R. Abbasi, Y. Abdou, T. Abu-Zayyad, et al. Time-integrated Searches for Point-like Sources of Neutrinos with the 40-string IceCube Detector. *Astrophysical Journal*, 732:18, May 2011. doi: 10.1088/0004-637X/732/1/18, arXiv: 1012.2137.

[198] J. Braun, M. Baker, J. Dumm, et al. Time-dependent point source search methods in high energy neutrino astronomy. *Astropart. Phys.*, 33:175–181, April 2010. doi: 10.1016/j.astropartphys.2010.01.005, arXiv: 0912.1572.

[199] IceCube Collaboration, M. G. Aartsen et al. Searches for Time Dependent Neutrino Sources with IceCube Data from 2008 to 2012. *Astrophys. J.*, 807(1):46, 2015. doi: 10.1088/0004-637X/807/1/46, arXiv: 1503.00598.

[200] IceCube Collaboration, M. G. Aartsen et al. The Search for Transient Astrophysical Neutrino Emission With Icecube-deepcore. *Astrophys. J.*, 816(2):75, 2016. doi: 10.3847/0004-637X/816/2/75, arXiv: 1509.05029.

[201] IceCube Collaboration, M. G. Aartsen et al. IceCube-Gen2: A Vision for the Future of Neutrino Astronomy in Antarctica. 2014, arXiv: 1412.5106.

A. Overtraining plots for IC86-I selection
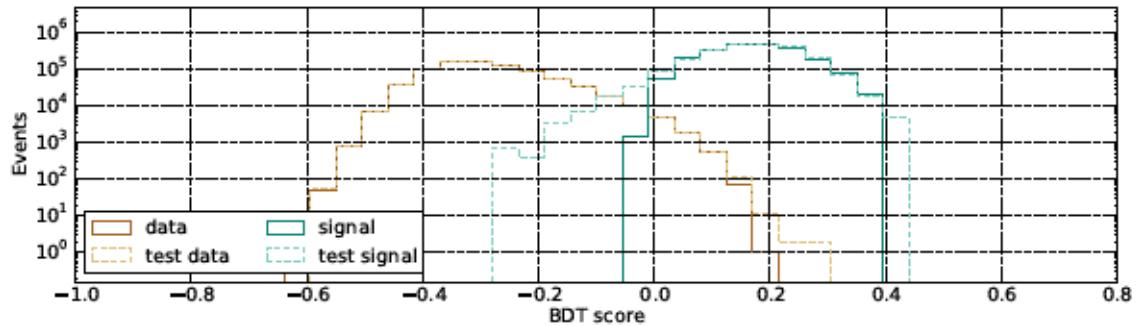
Figure A.1: Comparison between training and test sample for signal and data for IC86-I. The histograms for signal and test signal are scaled up to fit the number of events in data.
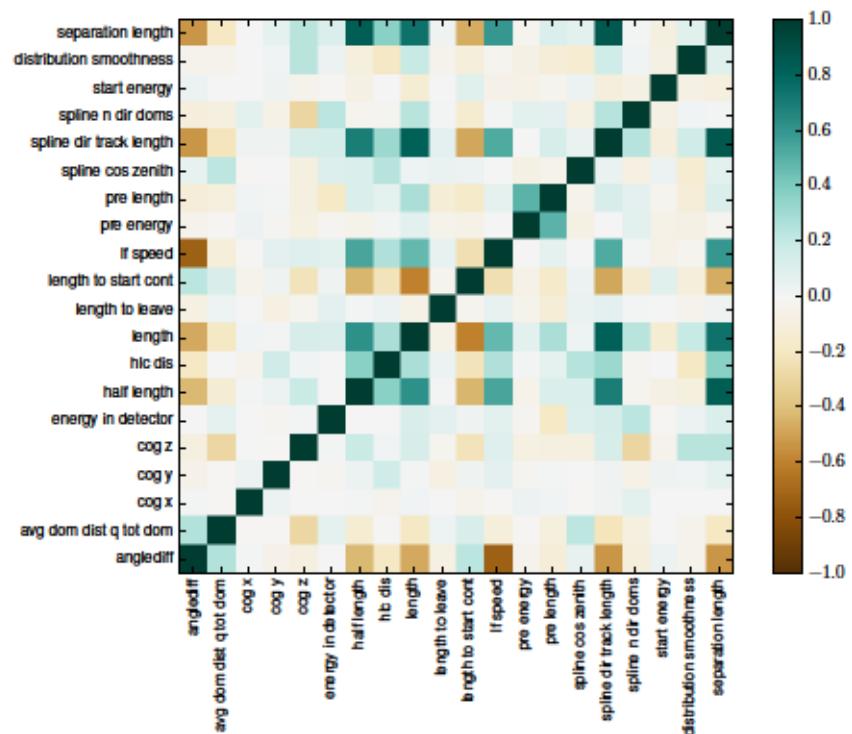
Figure A.2: BDT variables correlation Matrix (Signal) for the IC86-I selection.
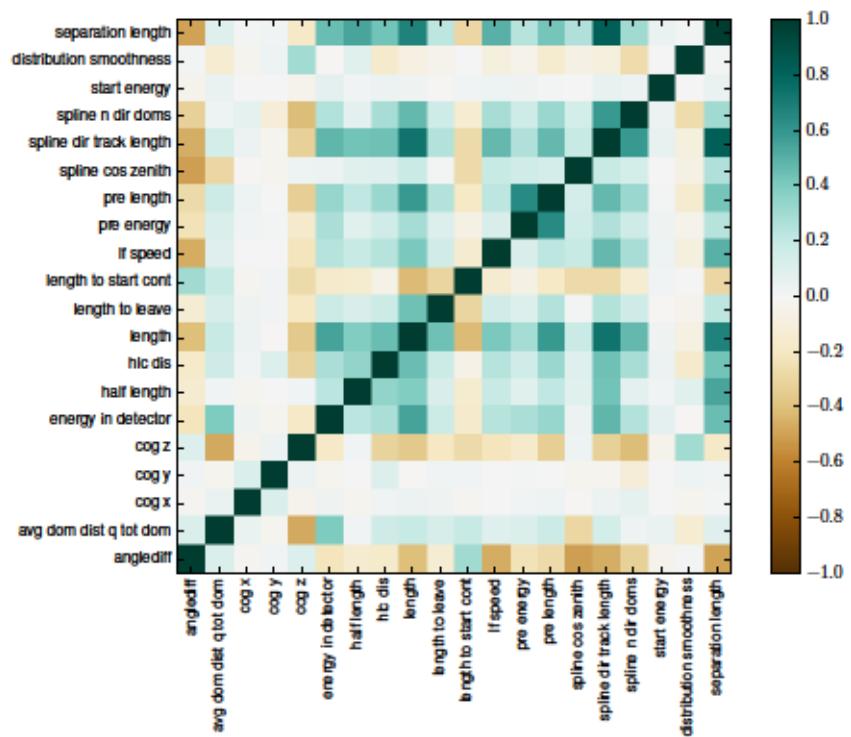
Figure A.3: BDT variables correlation Matrix (Background) for the IC86-I selection..

B. BDT variables for IC86-I selection
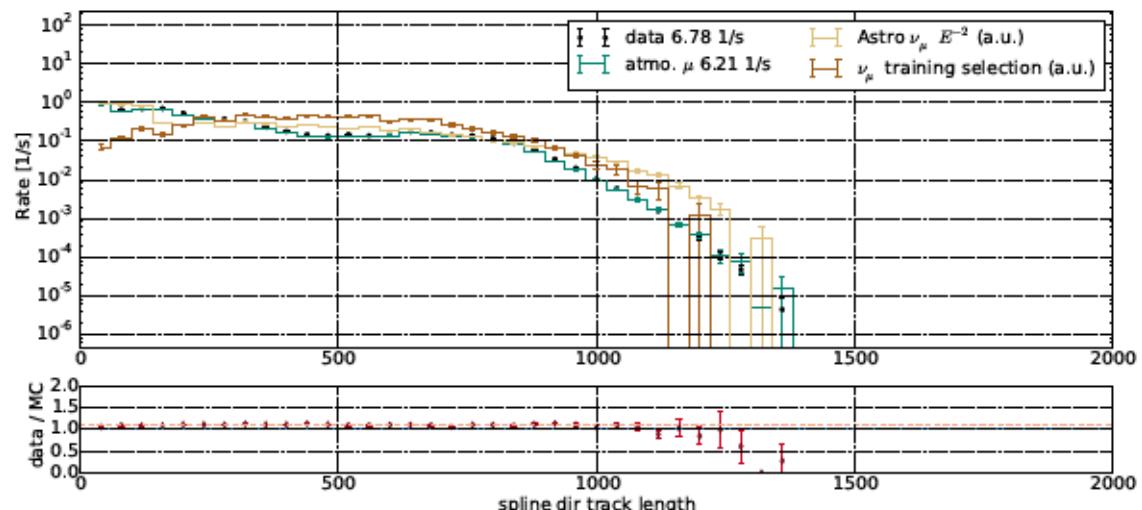
Figure B.1: spline dir track length

Figure B.2: anglediff
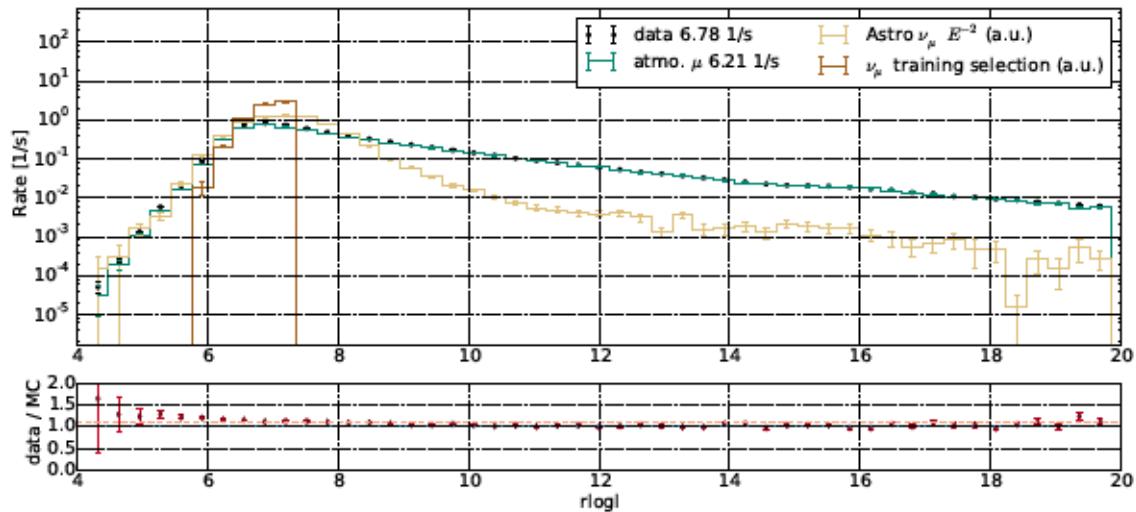
Figure B.3: rlogl
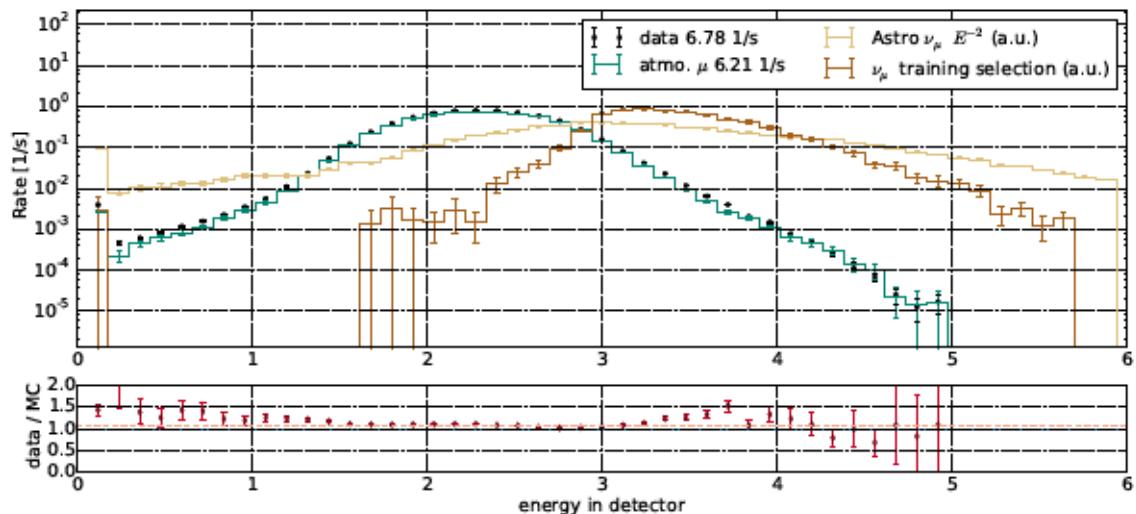
Figure B.4: energy in detector
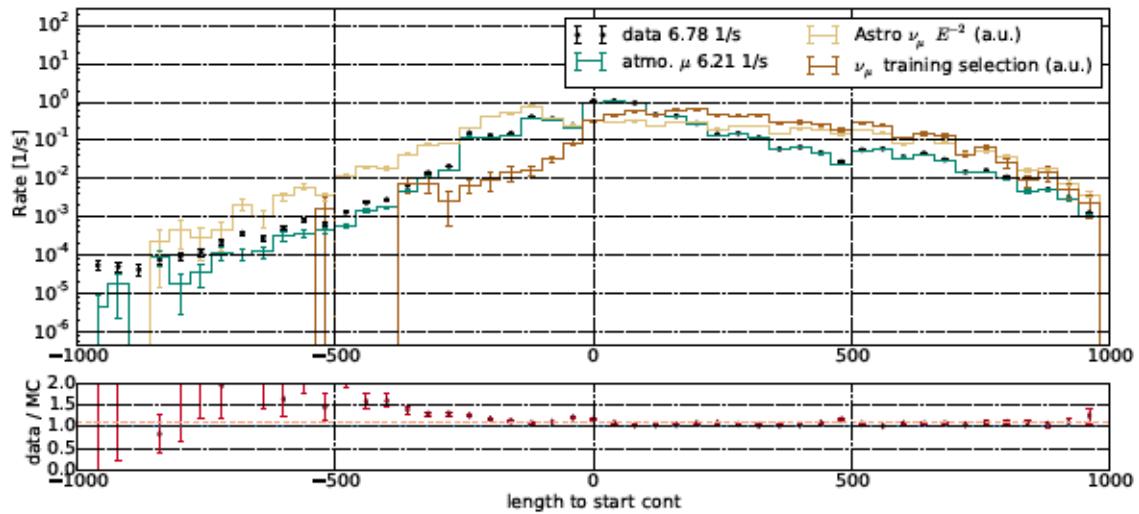
Figure B.5: length to start cont
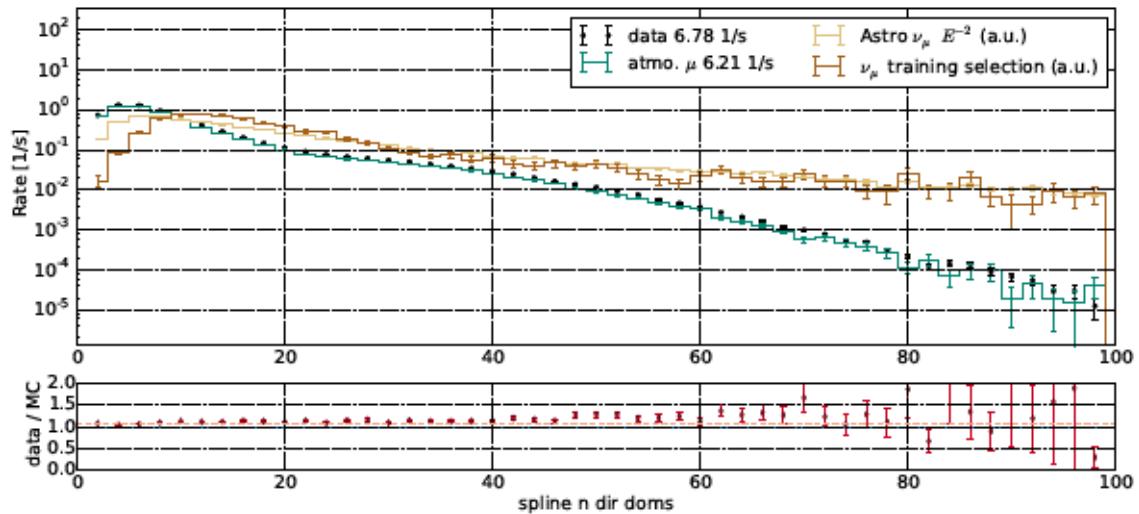
Figure B.6: spline n dir doms
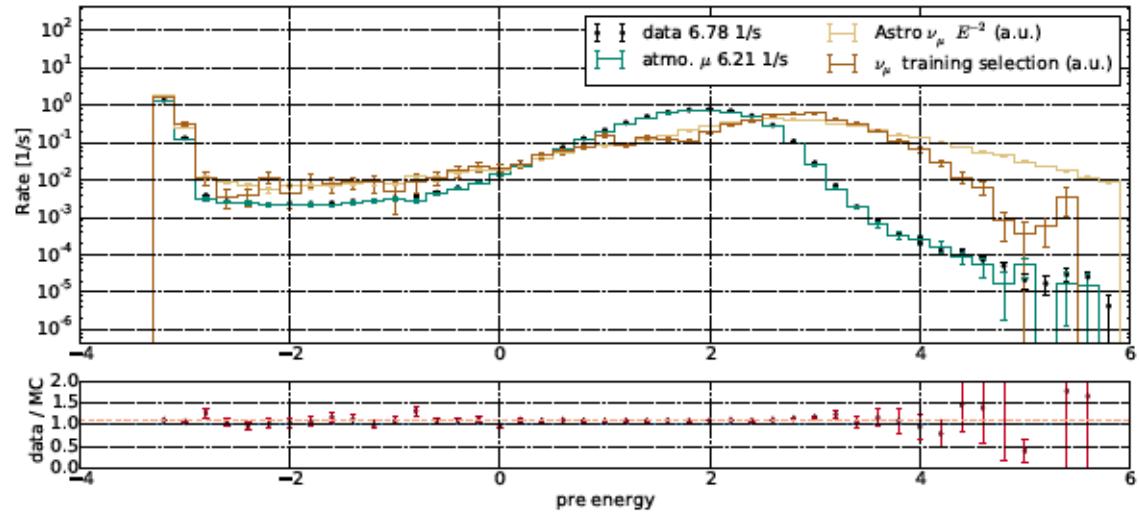
Figure B.7: pre energy
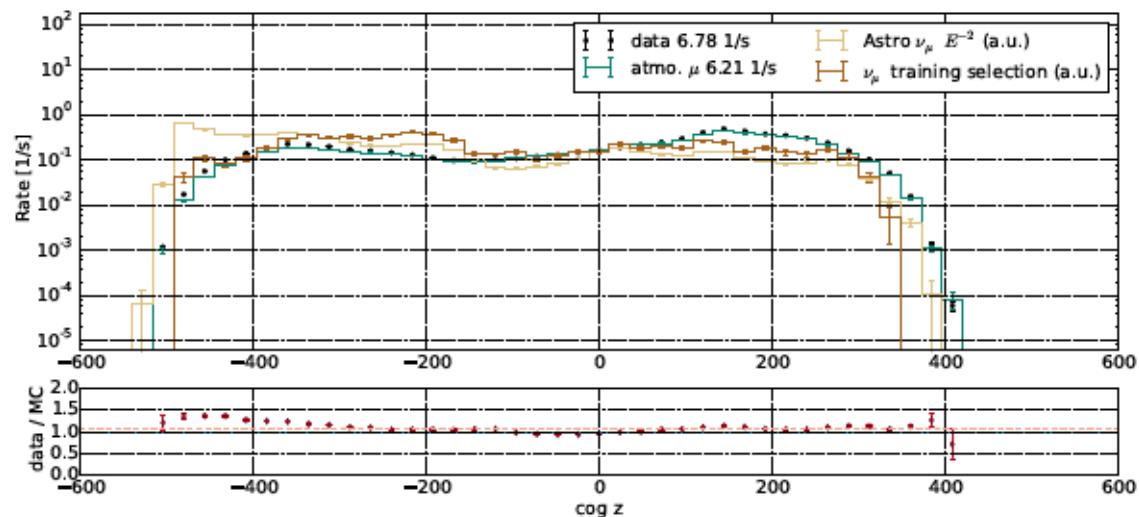
Figure B.8: cog z
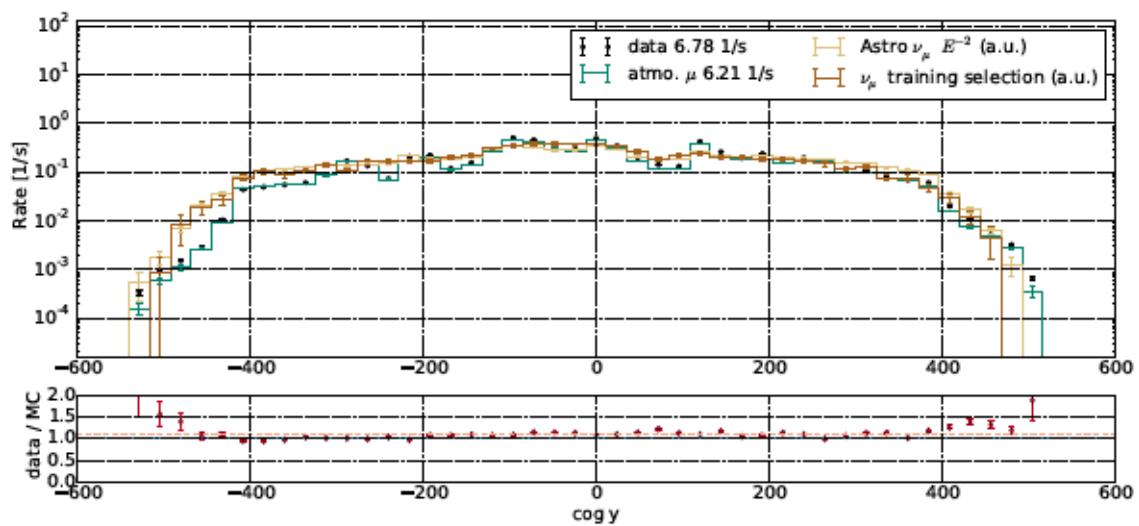
Figure B.9: cog y

Figure B.10: half length
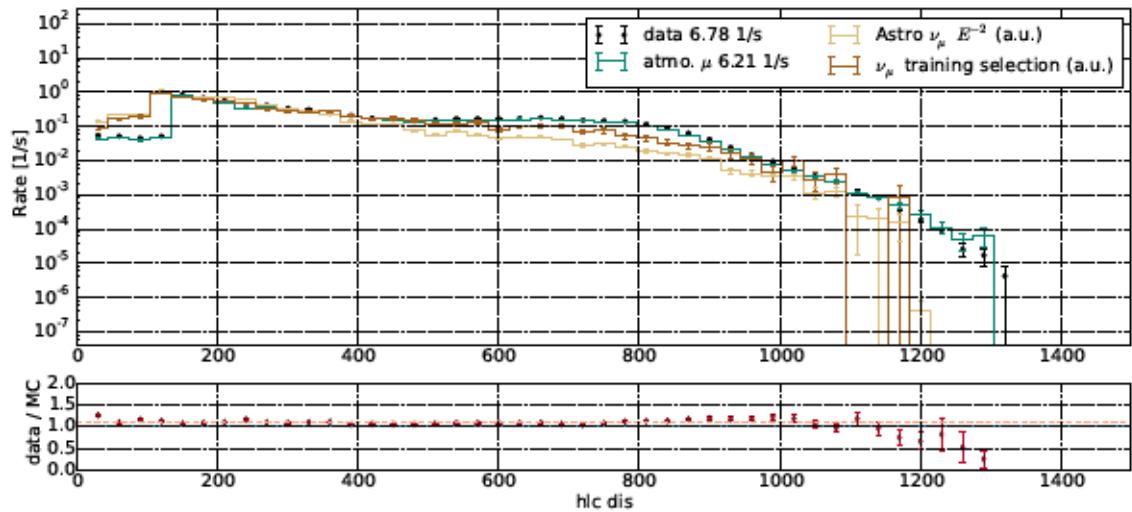
Figure B.11: hlc dis
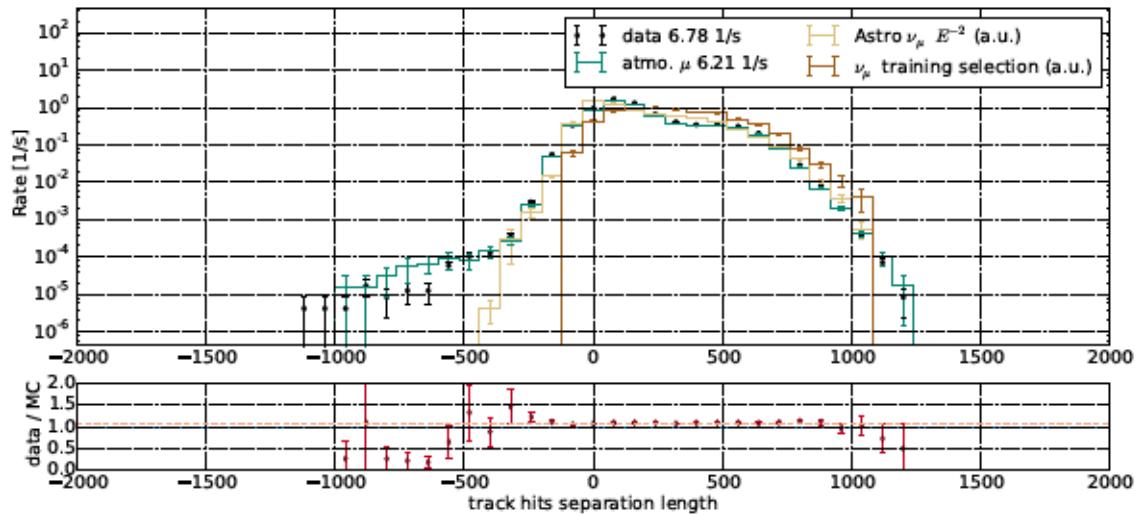

Figure B.12: track hits separation length
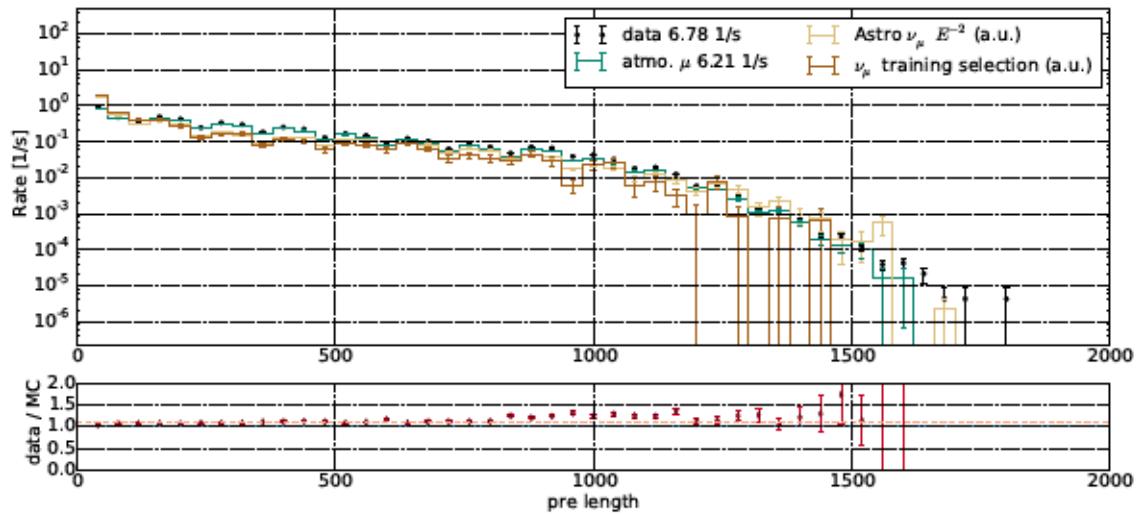
**Figure B.13:** pre length
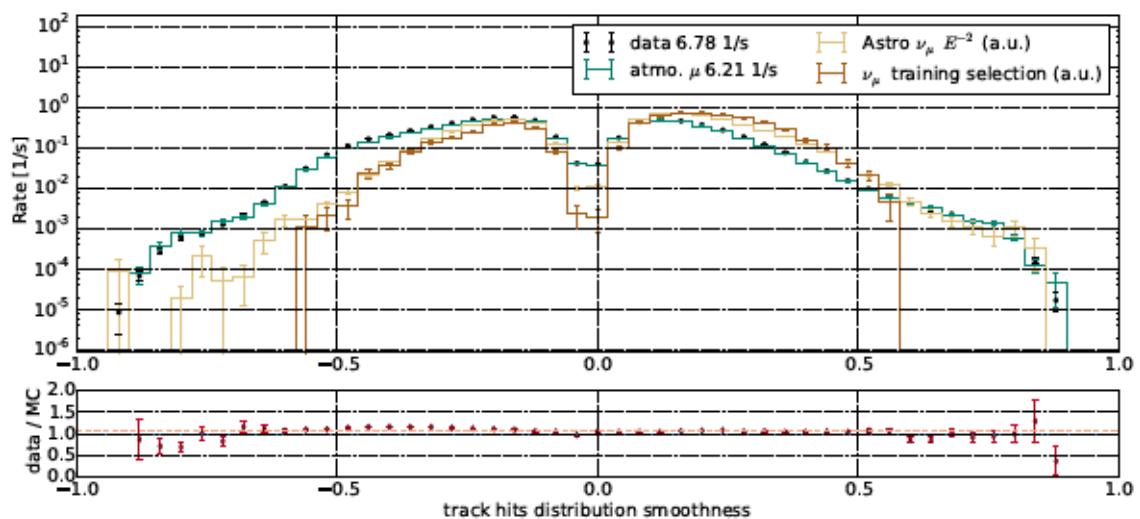
**Figure B.14:** track hits distribution smoothness
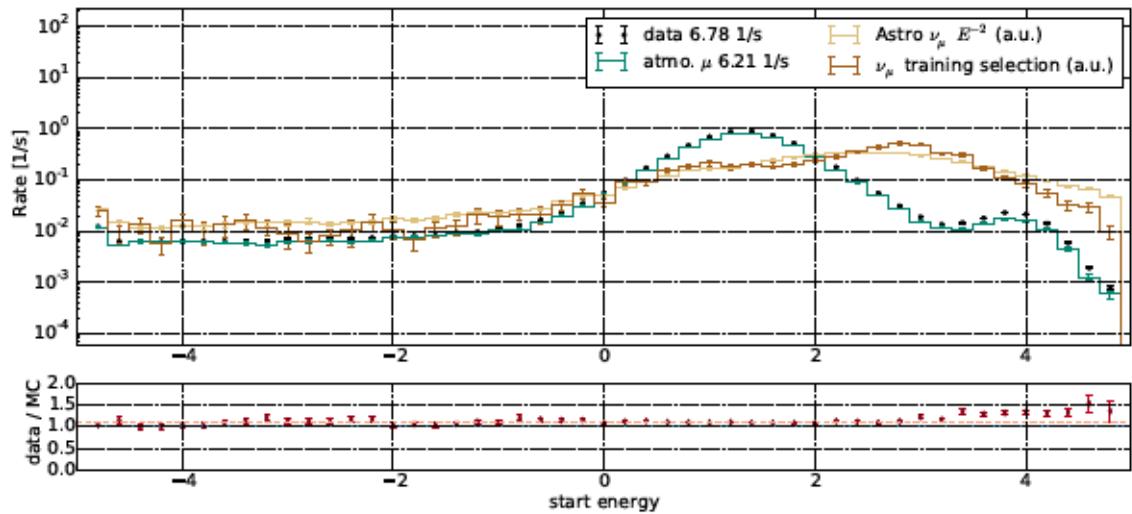
Figure B.15: start energy
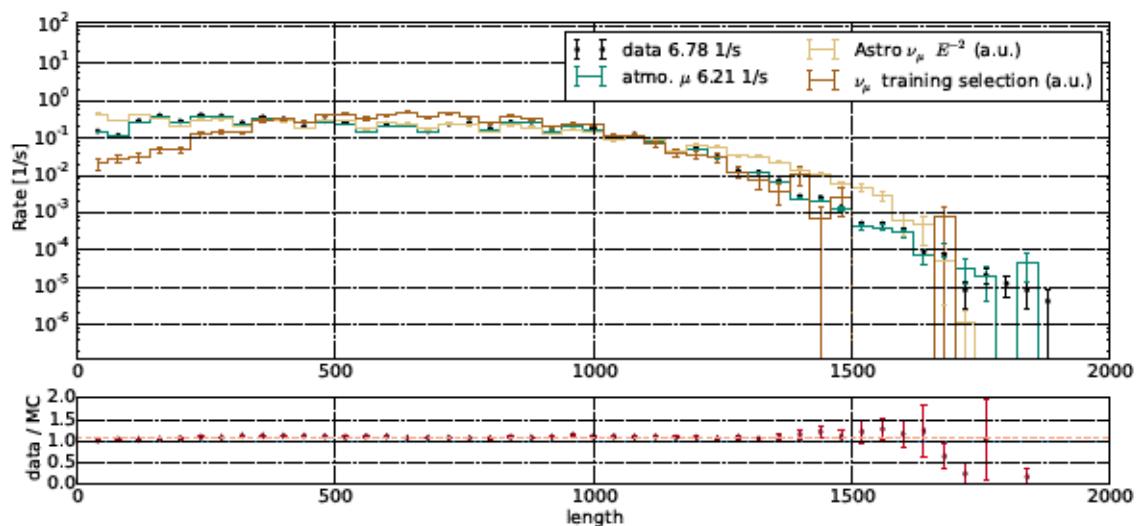
Figure B.16: length
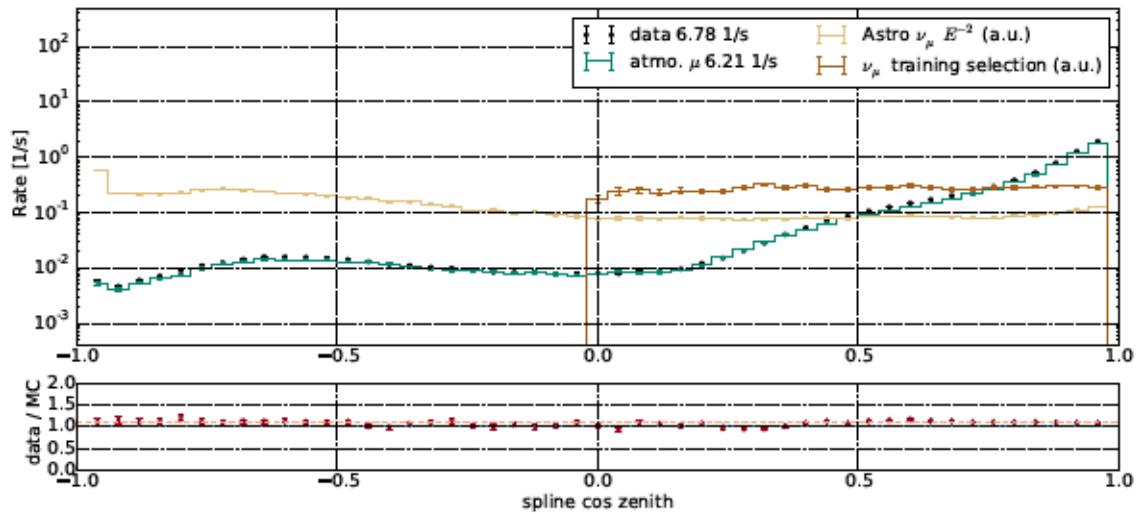
Figure B.17: spline cos zenith

Figure B.18: lf speed

Figure B.19: length to leave
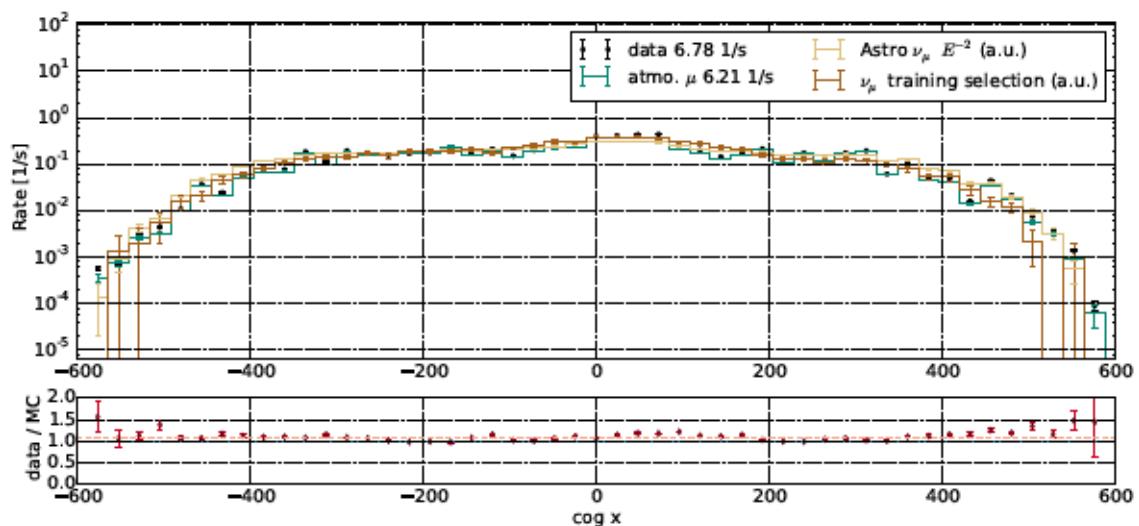
Figure B.20: cog x
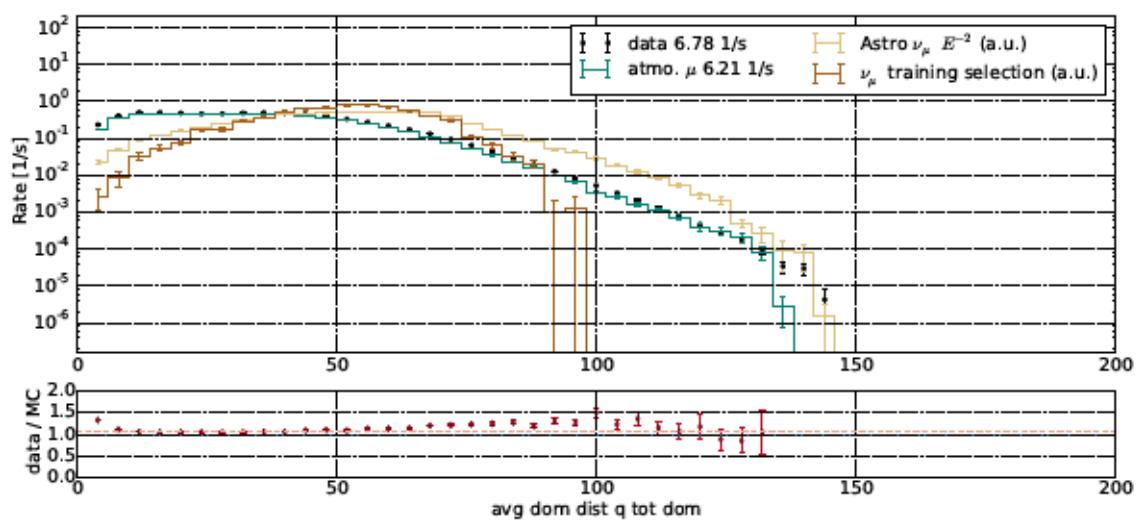
Figure B.21: avg dom dist q tot dom

C. BDT variables for IC86-II+ selection
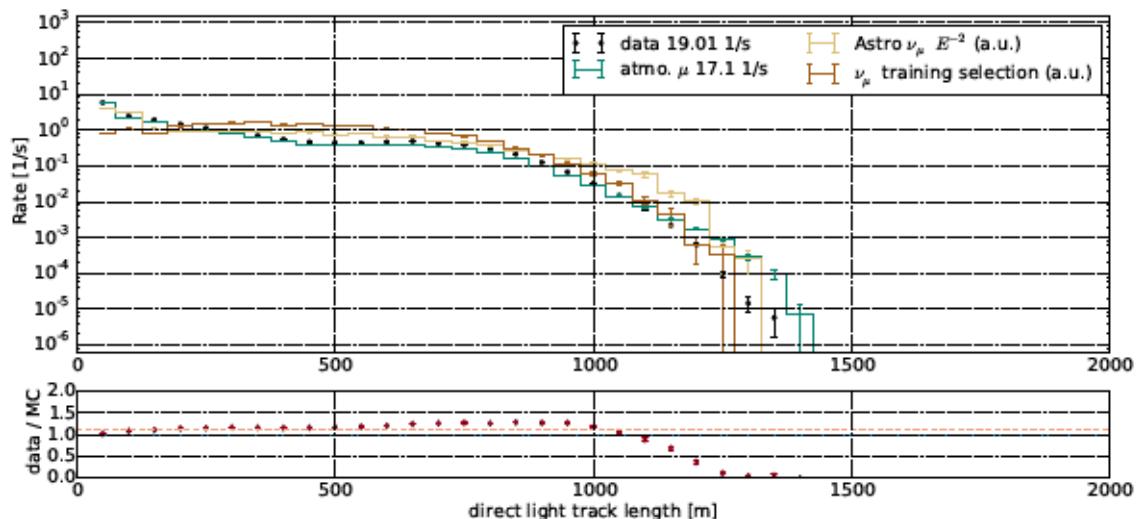
Figure C.1: spline dir track length

Figure C.2: angldiff
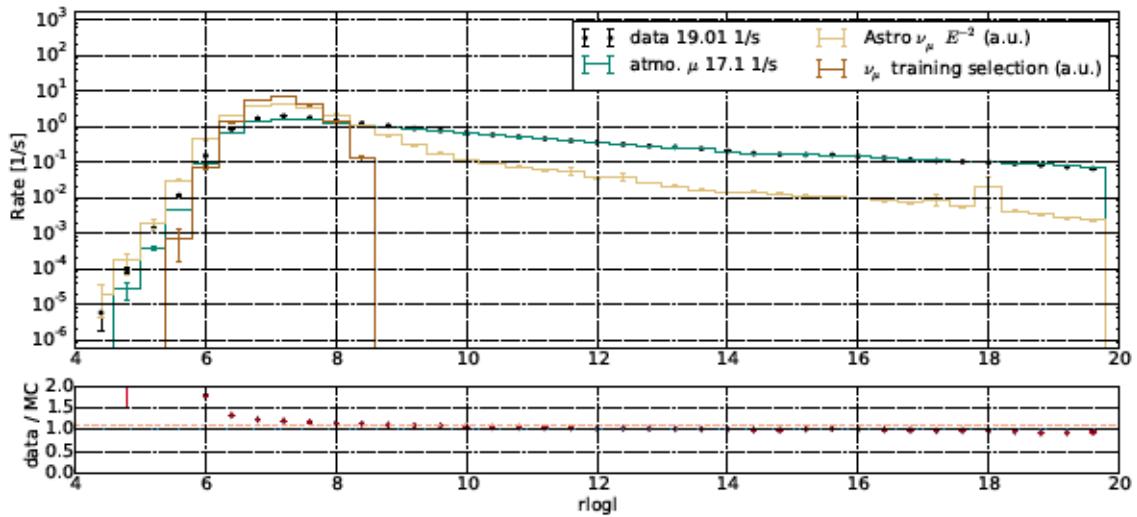
Figure C.3: rlogl
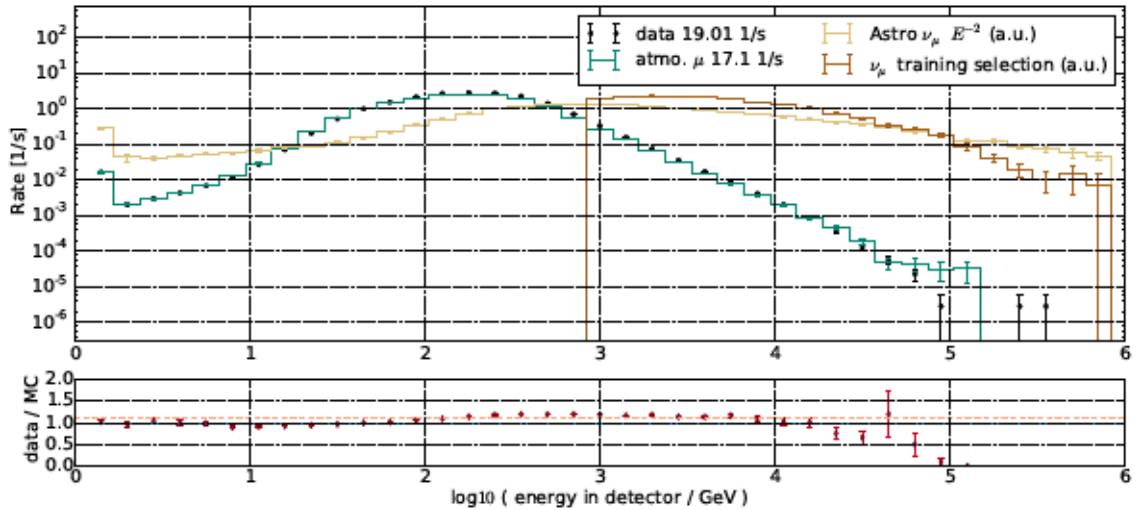
Figure C.4: energy in detector
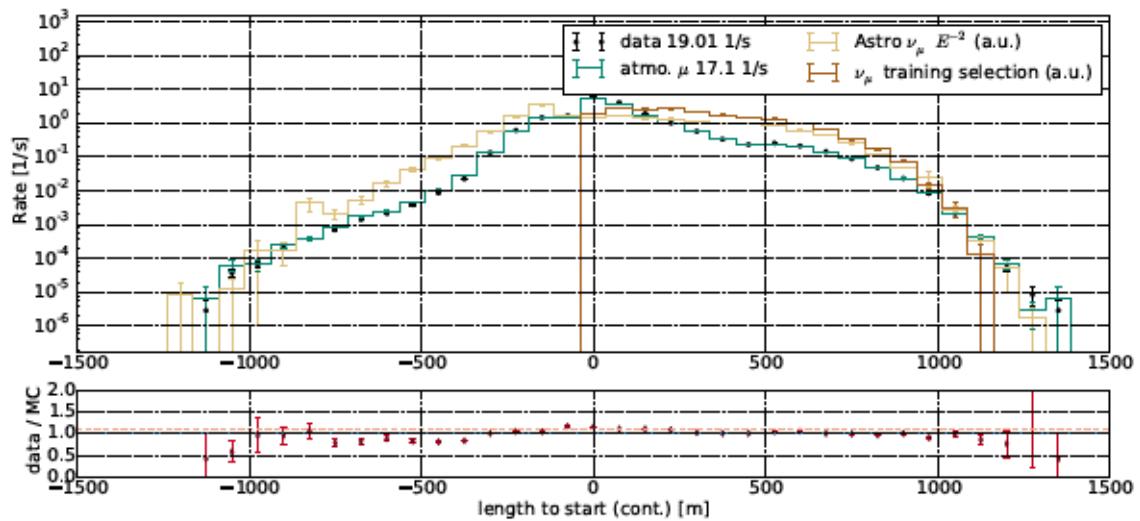
Figure C.5: length to start cont
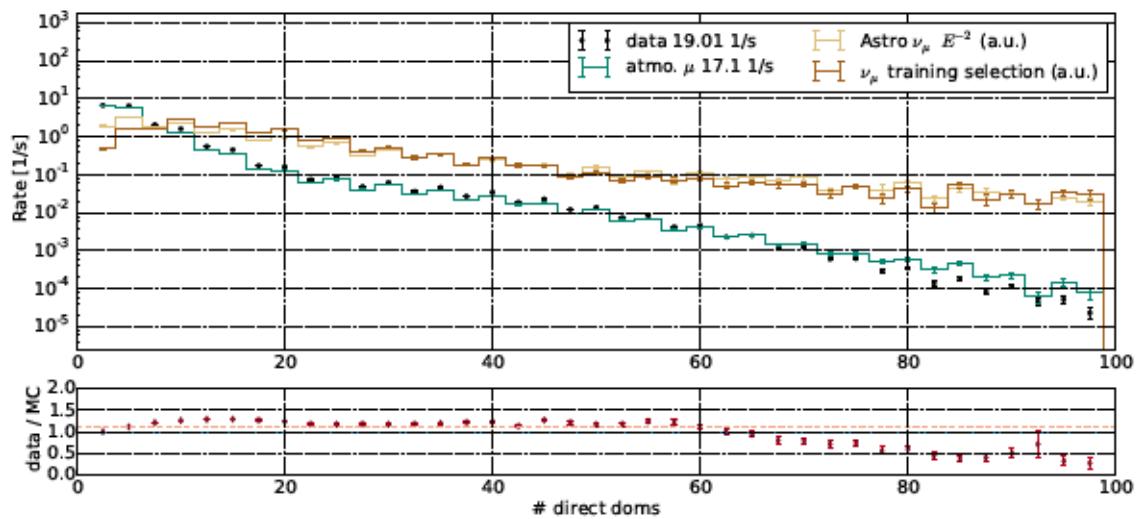
Figure C.6: spline n dir doms
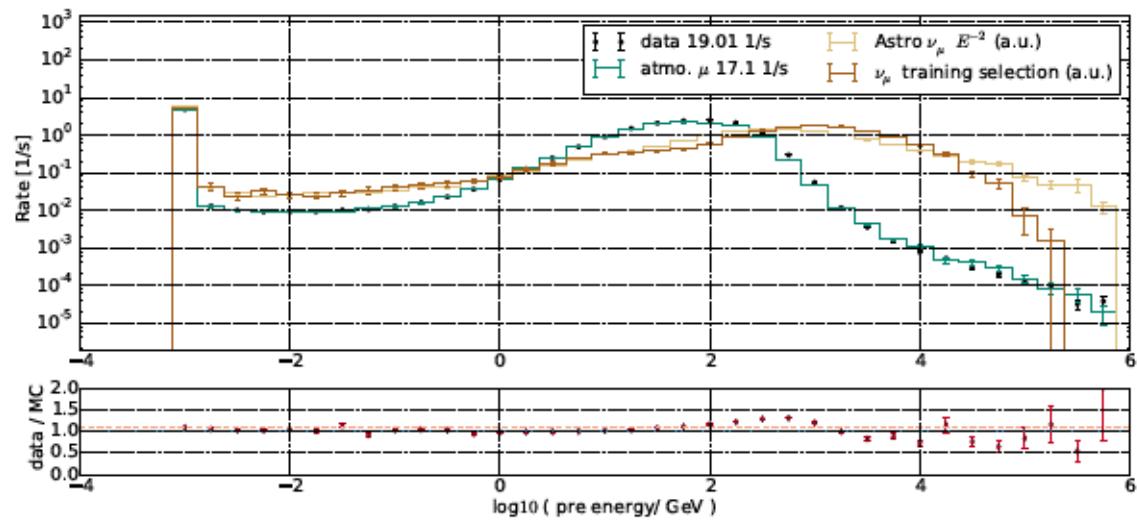
Figure C.7: pre energy

Figure C.8: cog z

Figure C.9: cog y

Figure C.10: half length
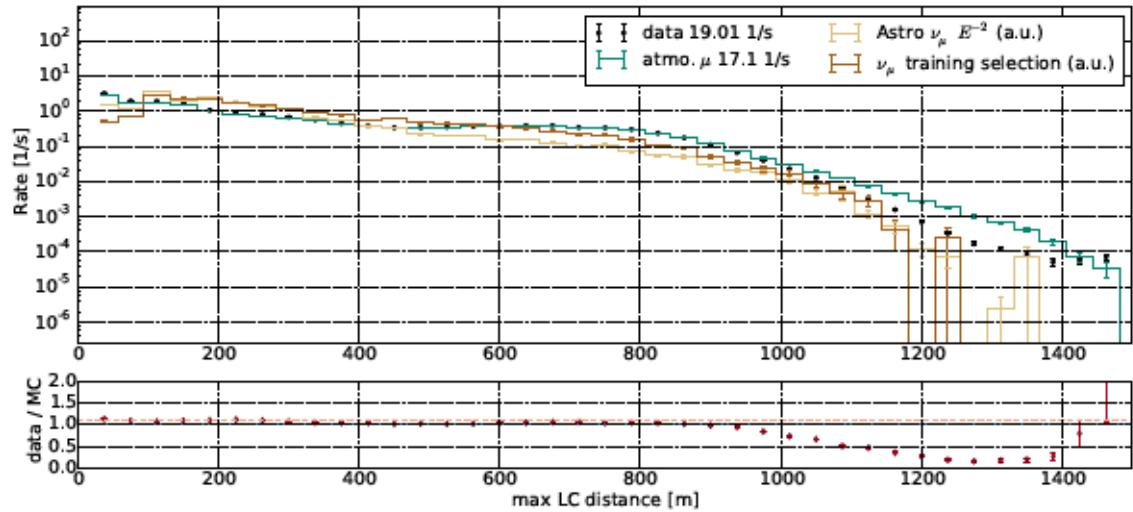
Figure C.11: hlc dis
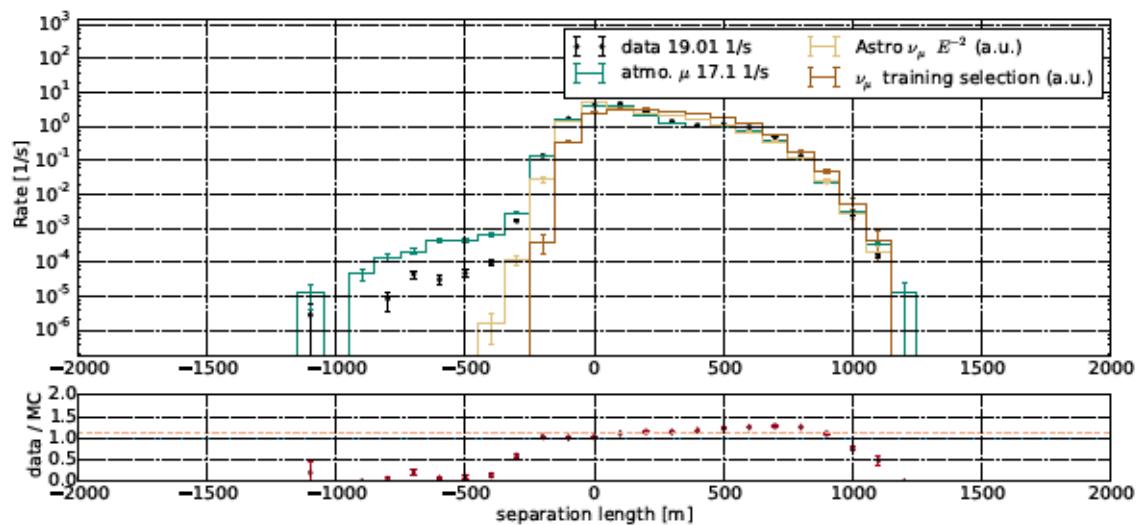
Figure C.12: track hits separation length
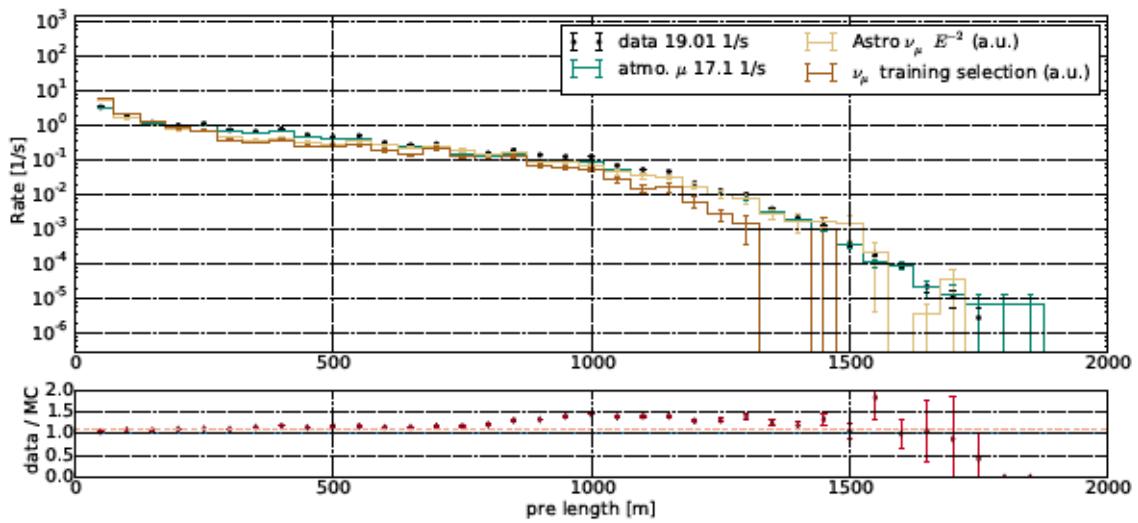
Figure C.13: pre length
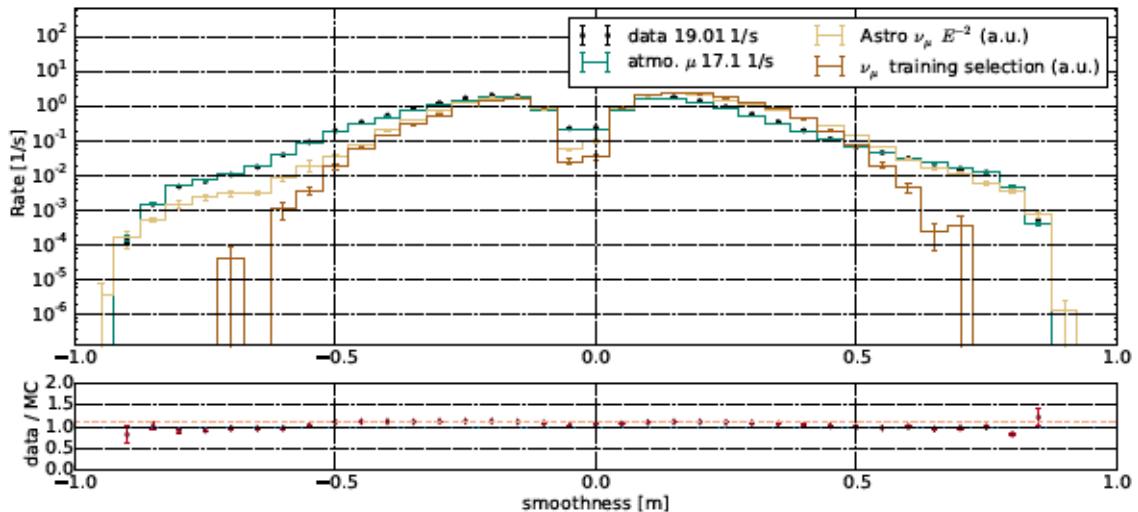
Figure C.14: track hits distribution smoothness
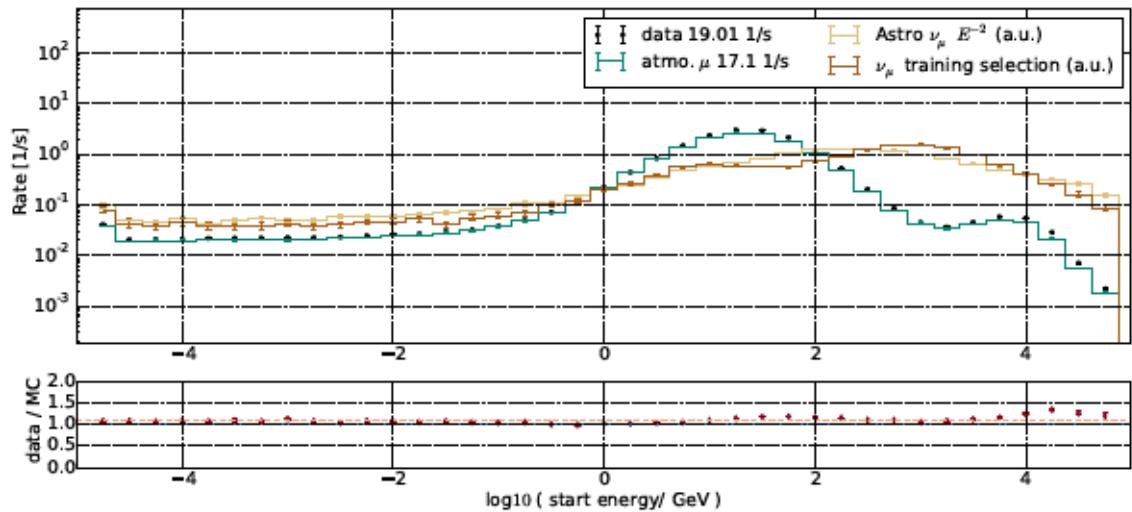
Figure C.15: start energy
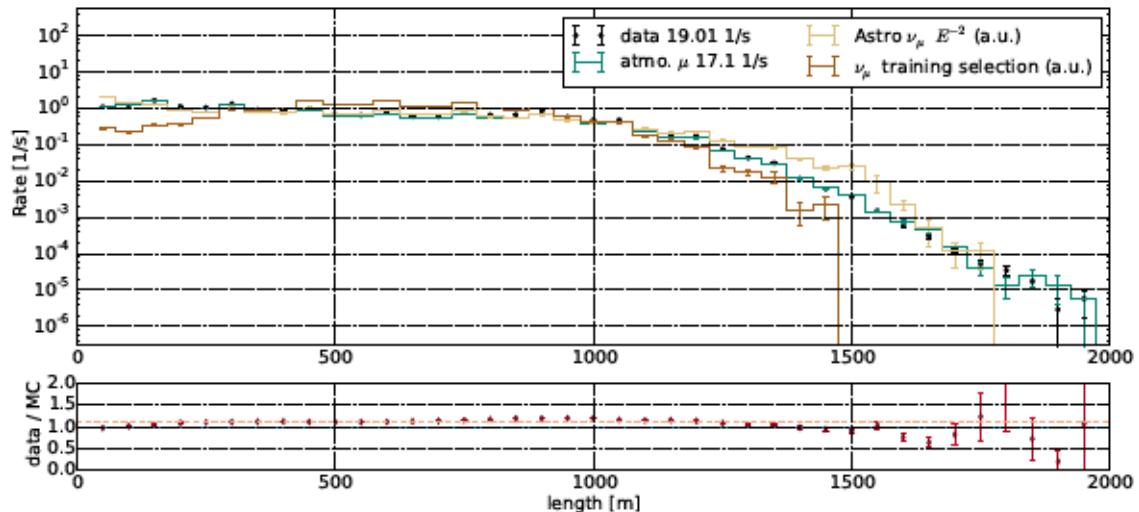
**Figure C.16:** length
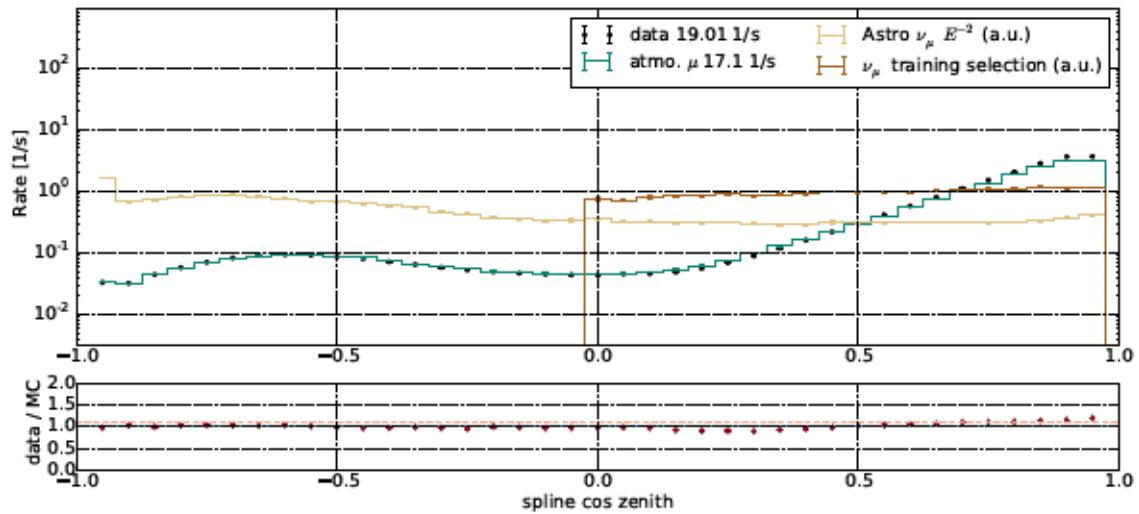
Figure C.17: spline cos zenith
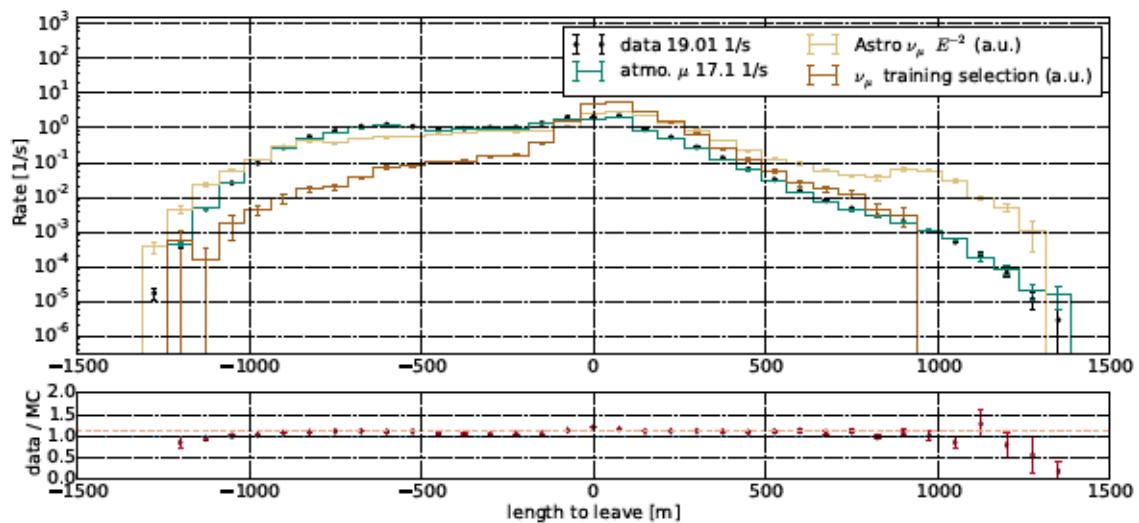
**Figure C.18:** length to leave

Figure C.19: cog x

Figure C.20: avg dom dist q tot dom

„Ich erkläre, dass ich die Dissertation selbständig und nur unter Verwendung der von mir gemäß § 7 Abs. 3 der Promotionsordnung der Mathematisch-Naturwissenschaftlichen Fakultät, veröffentlicht im Amtlichen Mitteilungsblatt der Humboldt-Universität zu Berlin Nr. 126/2014 am 18.11.2014 angegebenen Hilfsmittel angefertigt habe.“